

Summer 7-1-2022

**RELATIONSHIPS BETWEEN MONOMER CHEMICAL STRUCTURE,  
NETWORK ARCHITECTURE AND THERMAL STABILITY IN  
GLASSY POLYCYANURATES**

Rebecca Haber

Follow this and additional works at: <https://aquila.usm.edu/dissertations>

---

**Recommended Citation**

Haber, Rebecca, "RELATIONSHIPS BETWEEN MONOMER CHEMICAL STRUCTURE, NETWORK ARCHITECTURE AND THERMAL STABILITY IN GLASSY POLYCYANURATES" (2022). *Dissertations*. 2043. <https://aquila.usm.edu/dissertations/2043>

This Dissertation is brought to you for free and open access by The Aquila Digital Community. It has been accepted for inclusion in Dissertations by an authorized administrator of The Aquila Digital Community. For more information, please contact [aquilastaff@usm.edu](mailto:aquilastaff@usm.edu).

RELATIONSHIPS BETWEEN MONOMER CHEMICAL STRUCTURE, NETWORK  
ARCHITECTURE AND THERMAL STABILITY IN GLASSY POLYCYANURATES

by

Rebecca T. Haber

A Dissertation  
Submitted to the Graduate School,  
the College of Arts and Sciences  
and the School of Polymer Science and Engineering  
at The University of Southern Mississippi  
in Partial Fulfillment of the Requirements  
for the Degree of Doctor of Philosophy

Approved by:

Dr. Jeffrey S. Wiggins, Committee Chair  
Dr. Sergei Nazarenko  
Dr. Xiaodan Gu  
Dr. Yoan Simon  
Dr. Derek Patton

August 2022

COPYRIGHT BY

Rebecca T. Haber

2022

*Published by the Graduate School*



## ABSTRACT

We study monomer melt properties and polymer properties using two approaches. The first approach takes advantage of molecular dynamics to calculate monomer melt properties. The second approach involved an experimental investigation of polycyanurate networks with varying monomer functionality and rigidity.

For our computational study we applied an existing voids method by Solca et al. to calculate melting temperature for four different cyanate esters: (a) 2'-(4-cyanatophenyl) propane (BADCy), (b) 4,4'-(ethane-1,1-diyl) bis(cyanatobenzene) (LECy), (c) tris(4-cyanatophenyl) methylsilane (SiCy-3), and (d) bis(4-cyanatophenyl) dimethylsilane (SiMCy). For systems with 1 to 10% voids, the predicted melting temperature decreased due to a decrease in the free energy barrier to melting.

We synthesized cyanate ester monomers from a plant source, resveratrol, and compared the properties to cyanate esters of bisphenol A and bisphenol E. Polymer properties were characterized via DSC, DMA, and TGA. The increase in functionality and backbone rigidity of the resveratrol polycyanurates produced networks with glass transition temperatures up to 296 °C and char yields up to 70 %. Additionally, thermal, thermo-oxidative, and ablative properties were measured by TGA, TGA-MS, cone calorimetry, SEM, and EDX. Cone calorimetry data revealed that networks from cisResCy produced a *decrease* in Total Heat Release.

Monofunctional and trifunctional cyanate ester monomers, cardanol-cyanate ester (1-cyanato-3-pentadecylbenzene, CardCy) and cis-resveratrol-cyanate ester (cis-3,4',5-tricyanatostilbene, cisResCy), respectively, were synthesized from biobased cardanol and resveratrol. The cisResCy monomer was blended with varying weights of CardCy and

co-cured to produce five polycyanurate networks. The organic polymers displayed outstanding thermal stability and enhanced mechanical dampening.

## ACKNOWLEDGMENTS

There are several people I would like to thank and will do so in chronological order. My parents Robert and Suzanne, sister Hannah, grandfather Larry, and grandmother Elly are the perfect devoted family. Their never-ending love, cheer, and encouragement are the center of my world. I also look to my uncle Les and aunt Carole for their encouragement and support. In addition, I would like to thank my cousins Jared and Britainy for their support and hospitality. At the University of Southern Mississippi, I could not have found a better research advisor than Dr. Jeffrey S. Wiggins. I am one hundred percent certain my life will be more fascinating and rewarding since I have been lucky enough to be Doc's student at an "early" stage of my life. My committee Dr. Xiaodan Gu, Dr. Sergei Nazarenko, Dr. Derek Patton, and Dr. Yoan Simon will always have my sincere appreciation and utmost respect.

There are no words that can capture the appreciation and love for my fiancé Kevin. I will always be thankful that you have made my graduate experience so sweet and for your endless support. I would also like to thank the women and men in my first-year class and all of the WRG members past and present.

Contributions from several other researchers made this research achievable including Michael Blanton (SEM, EDX) and Karina Reynolds (Cone calorimetry). Finally, I would like to acknowledge Dr. Dr. Benjamin Harvey and Michael Garrison (Naval Air Warfare Center, Weapons Division) and Dr. Andrea Browning (Schrodinger) who have been ideal mentors guiding my research efforts. I deeply appreciate their involvement throughout my time in graduate school.

## DEDICATION

To my loving parents, Robert and Suzanne, and grandparents Larry and Elly who instilled in me integrity, grit, and honesty. My fiancé Kevin, whose love and companionship means so much to me. To my sister Hannah who continues to give me a lifetime of love and joy. And to my uncle Les and aunt Carole for their unending support.

## TABLE OF CONTENTS

ABSTRACT .....	ii
ACKNOWLEDGMENTS .....	iv
DEDICATION .....	iv
LIST OF TABLES .....	ix
LIST OF ILLUSTRATIONS .....	xi
CHAPTER I - INTRODUCTION .....	1
1.1 Aerospace Composites and Aircraft Fire Protection .....	1
1.2 Cyanate Ester Monomers .....	3
1.3 Monomer Melt Properties and Molecular Modelling .....	7
1.4 Polycyanurate Network Architecture.....	10
1.5 Polycyanurate Degradation and Char Formation.....	13
1.6 Sustainable Cyanate Ester Blends.....	18
1.7 Research Overview .....	20
CHAPTER II – EXPERIMENTAL .....	23
2.1 Materials .....	23
2.2 Synthesis .....	24
2.2.1 Synthesis of cisResCy Monomer .....	24
2.2.2 Synthesis of CardCy Monomer.....	26
2.3 Sample Preparation .....	27



2.4 Characterization .....	28
2.4.1 Proton <sup>1</sup> H NMR.....	28
2.4.2 Fourier Transform Infrared Spectroscopy (FTIR) .....	28
2.4.3 Dynamic Scanning Calorimetry (DSC) .....	28
2.4.4 TGA .....	30
2.4.5 TGA-MS .....	30
2.4.6 Dynamic Mechanical Analysis (DMA) .....	30
2.4.7 Rheology .....	31
2.4.8 Cone Calorimetry .....	31
2.4.9 Scanning Electron Microscopy .....	31
2.4.10 Molecular Dynamics Simulations.....	32
 CHAPTER III – MOLECULAR DYNAMICS SIMULATIONS OF CYANATE ESTER MONOMER MELT PROPERTIES .....	
3.1 Abstract.....	36
3.2 Results and Discussion .....	36
3.2.1 Melting of Monomers with 0% Voids .....	36
3.2.2 Dependence of Monomer Melting Temperature on Percentage of Voids .....	41
3.2.3 Structural Characterization .....	46
3.3 Conclusions.....	55

CHAPTER IV – EFFECT OF MONOMER STRUCTURE ON THERMAL AND THERMOMECHANICAL PROPERTIES .....	57
4.1 Abstract .....	57
4.2 Results and Discussion .....	57
4.2.1 Synthesis of cisResCy Monomer .....	58
4.2.2 DSC .....	65
4.2.3 DMA .....	76
4.2.4 TGA .....	82
4.3 Conclusions .....	83
CHAPTER V – THERMAL DEGRADATION OF POLYCYANURATES.....	85
5.1 Abstract .....	85
5.2 Results and Discussion .....	85
5.2.1 TGA .....	86
5.2.2 TGA-MS .....	89
5.2.3 Cone Calorimetry.....	92
5.2.4 Visual Inspection of Charred Specimens.....	96
5.2.5 SEM .....	97
5.2.6 EDX .....	99
5.3 Conclusions.....	100

CHAPTER VI – STRUCTURE-PROPERTY RELATIONSHIPS OF BIOBASED CYANATE ESTER BLENDS.....	101
6.1 Abstract.....	101
6.2 Results and Discussion .....	102
6.2.1 Monomer Synthesis .....	102
6.2.2 FTIR.....	104
6.2.3 DSC.....	105
6.2.4 TGA .....	112
6.2.5 DMA .....	114
6.2.6 Rheology .....	119
6.3 Conclusions.....	120
REFERENCES .....	121

## LIST OF TABLES

Table 1.1 Structures of commercial cyanate esters.....	8
Table 2.1 Composition of cyanate ester mixtures.....	27
Table 3.1 The melting points of cyanate ester monomers with 9% voids compared to previously reported literature values.....	45
Table 3.2 The orientational order parameter values for monomers: 50 K below the calculated melting temperature and 50 K above the calculated melting temperature .....	48
Table 4.1 DSC data for monomers .....	66
Table 4.2 Average complex viscosity of resins from 100 to 125 °C.....	70
Table 4.3 DSC data for monomers .....	72
Table 4.4 The extent of cure of cisResCy, BPACy, and LECy at each stage of the stepwise polymerization protocol .....	75
Table 4.5 Dynamic mechanical properties for polymers with an industrial cure .....	77
Table 4.6 Thermal degradation of industrial polycyanurates in Nitrogen and Air.....	83
Table 5.1 Thermal degradation temperatures for polycyanurates .....	88
Table 5.2 Combustion behavior of polycyanurates using from calorimetry experiments	93
Table 5.3 EDX data.....	99
Table 6.1 DSC Values for the Following Monomer Blends: (a) neat cisResCy, (b) 5 wt% CardCy/ cisResCy, (c) 10 wt% CardCy/ cisResCy, (d) 20 wt% CardCy/ cisResCy, and (e) 30 wt% CardCy/ cisResCy .....	106
Table 6.2 Average activation energy of cisResCy/cardCy blends obtained by the Kissinger and Ozawa methods utilizing the peak exotherm temperatures, ranked on kJ/mol.....	110

Table 6.3 DSC data for cyanate ester blends with calculated enthalpy of polymerization based on the linear rule of mixtures .....	112
Table 6.4 Summary of TGA experiments.....	113
Table 6.5 Dynamic mechanical analysis of polymers. ....	115

## LIST OF ILLUSTRATIONS

Figure 1.1 General chemical structure for a difunctional commercial cyanate ester of cyanic acid and bisphenols.....	4
Figure 1.2 General reaction scheme for cyanate ester monomer synthesis. ....	4
Figure 1.3 An excess of phenoxide results in the formation of an imidocarbonate.....	5
Figure 1.4 During the von Braun reaction cyanogen bromide reactions with a tertiary amine yielding an alkyl bromide and a disubstituted cyanamide. ....	6
Figure 1.5 Addition polymerization reaction forms triazine rings. ....	12
Figure 1.6 Cyanate ester groups are polymerized by phenol in the monomer. ....	13
Figure 1.7 Combustion of a glassy amorphous polymer combustion, where solid black arrows represent heat flux and broken black arrows represent gas diffusion. ....	15
Figure 1.8 Polycyanurate thermal degradation reactions.....	17
Figure 1.9 Thermo-oxidative degradation of polycyanurates.....	18
Figure 2.1 Cyanate ester monomer structures.....	23
Figure 2.2 Isomerization of trans-resveratrol to cis-resveratrol.....	25
Figure 2.3 Cyanation of cis-resveratrol to cisResCy. ....	25
Figure 2.4 Synthesis of CardCy monomer.....	27
Figure 2.5 MD workflow of melting temperature simulations. ....	34
Figure 3.1 The effect of ensemble size on the calculated melting temperature for: <b>(a)</b> BADCy (256 molecules), <b>(b)</b> BADCy (400 molecules), <b>(c)</b> LECy (256 molecules), <b>(d)</b> LECy (400 molecules), <b>(e)</b> SiCy-3 (256 molecules), <b>(f)</b> SiCy-3 (400 molecules), <b>(g)</b> SiMCy 256 molecules), and <b>(h)</b> SiMCy (400 molecules). ....	38

Figure 3.2 The effect of heating rate on the calculated melting temperature for: **(a)** BADCy (50 K/ 20 ns), **(b)** BADCy (25 K/ 20 ns), **(c)** LECy (50 K/ 20 ns), **(d)** LECy (25 K/ 20 ns), **(e)** SiCy-3 (50 K/ 20 ns), **(f)** SiCy-3 (25 K/ 20 ns), **(g)** SiMCy (50 K/ 20 ns), and **(h)** SiMCy (25 K/ 20 ns). ..... 39

Figure 3.3 The volume as a function of temperature for monomers: **(a)** BADCy, **(b)** LECy, **(c)** SiCy-3, and **(d)** SiMCy with 0% voids. The calculated melting temperature ( $T_{m,calc}$ ) is represented by the discontinuity or inflection (arrow). The results are compared to previously reported experimental melting temperatures (dotted line). ..... 41

Figure 3.4 The evolution of volume as a function of temperature starting at  $T = 150$  K for **(a)** BADCy, **(b)** LECy, **(c)** SiCy-3, and **(d)** SiMCy with 1 to 10% voids. .... 42

Figure 3.5 **(a)** The calculated melting temperature as a function of percentage voids (in % of the total monomers removed from simulation cell) and **(b)** calculated  $T_m$  at 9% voids compared to experimental  $T_m$ . ..... 43

Figure 3.6 Percent error of the calculated melting temperature, compared to the experimental values, for simulations with 0 to 10% voids (in % of the total monomers removed from simulation cell) for: **(a)** BADCy, **(b)** LECy, **(c)** SiCy-3, and **(d)** SiMCy. 44

Figure 3.7 The evolution of volume as a function of temperature for SiMCy with: **(a)** 256 and **(b)** 400 molecules. .... 46

Figure 3.8 Snapshots of the monomers at different stages of the melting process with 9% voids for the following monomers: **(a)** BADCy (300 K), **(b)** BADCy (450 K), **(c)** LECy (250 K), **(d)** LECy (400 K), **(e)** SiCy-3 (350 K), **(f)** SiCy-3 (500 K), **(g)** SiMCy (250 K), and **(h)** SiMCy (400 K). ..... 47

Figure 3.9 Snapshots of (a) BADCy and (b) LECy, highlighting the ordering of close contacts. The principal moments of inertia are displayed as a set of orthogonal tubes. ....	49
Figure 3.10 The orientational order parameter for BADCy 50 K below the calculated melting temperature (black line) and 50 K above the calculated melting temperature (blue line). Included is a snapshot of monomers in the ordered state below the calculated melting temperature and disordered state above the calculated melting temperature. ....	50
Figure 3.11 The orientational order parameter for monomers: (a) LECy, (b) SiCy-3, and (c) SiMCy 50 K below the calculated melting temperature (black line) and 50 K above the calculated melting temperature (blue line).....	51
Figure 3.12 Histogram plots to examine the distribution angle values for an individual torsion for: (a) BADCy, (b) LECy, (c) SiCy-3, and (d) SiMCy. ....	53
Figure 3.13 Display of angles for each individual torsion as a bar plot over the simulation time range with colors denoting the size of the angle for BADCy. ....	54
Figure 3.14 Display of angles for each individual torsion as a bar plot over the simulation time range with colors denoting the size of the angle for: (a) LECy, (b) SiCy-3, (c) SiMCy.....	55
Figure 4.1 (a) Isomerization of trans-resveratrol to cis-resveratrol and (b) cyanation of cis-resveratrol to cisResCy. ....	58
Figure 4.2 <sup>1</sup> H NMR of crude product from isomerization of trans-resveratrol to cis-resveratrol. ....	59
Figure 4.3 <sup>1</sup> H NMR of cis-resveratrol. ....	60
Figure 4.4 Heat flow vs. temperature for cis-resveratrol and trans-resveratrol. ....	61
Figure 4.5 Crystals of cisResCy.....	62



Figure 4.6 $^1\text{H}$ NMR of cisResCy.....	63
Figure 4.7 IR spectra of: (a) cis-resveratrol and (b) cisResCy.....	63
Figure 4.8 $^1\text{H}$ NMR of BPACy. ....	64
Figure 4.9 $^1\text{H}$ NMR of LECy. ....	65
Figure 4.10 Heat flow vs. temperature for cyanate ester monomers: (a) cisResCy, (b) BPACy, and (c) LECy. ....	67
Figure 4.11 Chemical structure of polymer network architecture from cisResCy monomer. ....	69
Figure 4.12 Heat flow vs. temperature for cyanate ester monomers with heating rates of 1, 5, and 10 °C. ....	71
Figure 4.13 (a) Kissinger plot of $\ln(\beta / T_p^2)$ vs. T and (b) Ozawa plot of $\ln(\beta)$ vs. $1/T$ for cyanate esters. ....	72
Figure 4.14 DSC plots of the residual enthalpy of polymerization for (a) cisResCy, (b) BPACy, and (c) LECy at each stage of the stepwise polymerization protocol. ....	74
Figure 4.15 Cyanate ester conversion based on DSC measurements. ....	75
Figure 4.16 $\tan \delta$ vs. temperature for polymers of (a) cisResCy, (b) BPACy, and (c) LECy.....	77
Figure 4.17 $E'$ vs. temperature for polymers of (a) cisResCy, (b) BPACy, and (c) LECy. ....	79
Figure 4.18 Difunctional polymer networks.....	81
Figure 4.19 Mass loss vs. temperature for polycyanurates.....	82

Figure 5.1 TGA plots of: (a) mass loss vs. temperature in nitrogen, (b) derivative of the mass loss vs. temperature in nitrogen, and (c) mass loss vs. temperature in air, and (d) derivative of the mass loss vs. temperature in air. ....	87
Figure 5.2 Ion current vs. temperature for (A) cisResCy, (B) BPACy, and (C) LECy in nitrogen. ....	90
Figure 5.3 Ion current vs. temperature for (A) cisResCy, (B) BPACy, and (C) LECy in air. ....	90
Figure 5.4 (a) Heat release rate vs. temperature, (b) rate of smoke production vs. temperature, and (c) mass loss vs. temperature. ....	92
Figure 5.5 The rate of mass loss vs. temperature for (a) cisResCy, (b) BPACy, and (c) LECy. ....	95
Figure 5.6 Carbonaceous char residues of polycyanurates. ....	96
Figure 5.7 SEM micrographs of (a) cisResCy, (b) cisResCy char low magnification, (c) cisResCy char high magnification, (d) BPACy, (e) BPACy char low magnification, (f) BPACy char high magnification, (g) LECy, (h) LECy char low magnification, and (i) LECy char high magnification. ....	98
Figure 6.1 <sup>1</sup> H NMR of cisResCy. ....	102
Figure 6.2 <sup>1</sup> H NMR of Cardanol. ....	103
Figure 6.3 <sup>1</sup> H NMR of CardCy. ....	103
Figure 6.4 The chemical structure of cardanol. ....	104
Figure 6.5 FTIR data for the cyanated monomers. ....	105

Figure 6.6 DSC thermograms of thermally polymerized cyanate ester monomers mixtures: **(a)** neat cisResCy, **(b)** 5 wt% CardCy/ cisResCy, **(c)** 10 wt% CardCy/ cisResCy, **(d)** 20 wt% CardCy/ cisResCy, and **(e)** 30 wt% CardCy/ cisResCy. .... 106

Figure 6.7 DSC thermograms at different heating rates for: **(A)** neat cisResCy, **(B)** 5 wt% cardCy/cisResCy, **(C)** 10 wt% cardCy/cisResCy, **(D)** 20 wt% cardCy/cisResCy, and **(E)** 30 wt% cardCy/cisResCy. .... 109

Figure 6.8 **(A)** Kissinger and **(B)** Ozawa plots for the calculation of activation energy for: (a) neat cisResCy, (b) 5 wt% cardCy/cisResCy, (c) 10 wt% cardCy/cisResCy, (d) 20 wt% cardCy/cisResCy, and (e) 30 wt% cardCy/cisResCy. .... 110

Figure 6.9 **(A)** TGA thermogram and **(B)** char yield bar graph for: (a) neat cisResCy, (b) 5 wt% CardCy/ cisResCy, (c) 10 wt% CardCy/ cisResCy, (d) 20 wt% CardCy/ cisResCy, and (e) 30 wt% CardCy/ResCy..... 112

Figure 6.10 DMA thermogram of **(A)** Tan  $\delta$  and **(B)** Storage modulus, and **(C)** bar graph of glassy and rubbery moduli for: (a) neat ResCy, (b) 5 wt% CardCy/ cisResCy cisResCy cisResCy, (c) 10 wt% CardCy/ cisResCy, (d) 20 wt% CardCy/ cisResCy, and (e) 30 wt% CardCy/ cisResCy..... 115

Figure 6.11 Mechanism of thermal polymerization of 1,4-diene groups that may occur during thermal polymerization of in the presence of small amounts of oxygen.<sup>110</sup>..... 118

Figure 6.12 Dynamic viscosity at of the cisResCy /CardCy mixtures at 100 °C: **(a)** neat cisResCy, **(b)** 5 wt% CardCy/ cisResCy, **(c)** 10 wt% CardCy/ cisResCy, **(d)** 20 wt% CardCy/ cisResCy, and **(e)** 30 wt% CardCy/ cisResCy..... 119

## CHAPTER I - INTRODUCTION

### 1.1 Aerospace Composites and Aircraft Fire Protection

Merging two dissimilar components with complementary properties dates back to biblical times, when ancient Egyptians and Hebrews reinforced clay bricks with straw to improve the composite's resistance to the elements.<sup>1</sup> Composites such as these are advantageous as they may have enhanced properties compared to other materials. In a like manner, Carbon Fiber Reinforced Polymers (CFRP's) have gained popularity in the present day as alternatives to steel and aluminum. Their wide adoption is due to several advantageous properties, compared to traditional metal components.<sup>2</sup> For example, CFRP's have been shown to have lighter weights, higher stiffness, corrosion resistance, thermal stability, high fatigue resistance and improved strength-to-weight ratios. The properties of CFRP's depend on a number of factors, including, but not limited to: fiber modulus, adhesion between the fiber and matrix, and choice of polymer matrix (thermoplastic or thermoset). Ultimately, the distinct properties of the matrix and reinforcement ultimately synergistically advance composite behavior. To this end, a wide variety of properties may be achieved considering the vast combination possibilities. Furthermore, material properties may also be varied through manufacturing method, processing conditions, and reinforcement orientations.

CFRP's that are classified as advanced composites are customarily defined by polymer matrices with exceptional thermomechanical properties and by long high performance reinforcements. Advanced composites are utilized for aerospace and defense applications including rocket motor cases and aircraft parts.<sup>2</sup> For example, fire-resistant composites have been used as replacement for aircraft metals. For fixed-wing aircraft, the

principal obstacle is vulnerability to fire, which may contribute to loss of aircraft and casualties. While methods exist to alleviate this risk, these engineering designs are limited by the weight constraints of traditional materials. Therefore, it is desirable to design light weight advanced composites with fire retardant properties. Recently, there has been an initiative in aerospace Original Equipment Manufacturers (OEM's) to maximize the weight percent of CFRP's into aircraft structures. While epoxide-amine composites have been established as the baseline polymer matrix material for aerospace composites, one drawback is that these organic polymers tend to be flammable. As a result, traditional CFRP's may degrade rapidly when exposed to fire since the continuous matrix phase is in immediate contact with the external environment. While epoxide-amines are the most widely used addition-polymerizable thermosetting polymers utilized in the aerospace industry for structural composites, the upper temperature range for structural performance  $\sim 177$  °C, which decreases to 149 °C in moist environments.<sup>3</sup> Consequently, their utility is limited for structural parts in extreme environments. To this end a plethora fire retardant additives and coatings have been created to address this drawback. On the other hand, conventional fire retardants often contain toxic halogens which have since been banned. For this reason, there is renewed interest in using high performance thermosetting matrices for aircraft composites which require skin temperatures higher than epoxide amine capacity.<sup>4</sup> Polycyanurate cyanate ester (CE) is an important class of high-performance polymers with rapid expansion in the thermoset composite matrix market. For example, the 2017 global CE market of \$195M is expected to exceed \$338M in 2022.<sup>5</sup> These thermally stable polymers have gained attention in applications requiring high glass-transition temperature ( $T_g$ ),<sup>4</sup> high strength/modulus,<sup>6</sup>

low water absorption,<sup>7</sup> no polymerization condensate,<sup>4</sup> low dielectric constant and loss,<sup>8</sup> and excellent adhesive properties.<sup>9</sup> Limitations often cited for CE adoption are cited as high brittleness<sup>10</sup> and prohibitively high cure temperatures with short processing windows.<sup>4</sup> Other concerns associated with CE and other composite matrix polymers such as benzoxazines and epoxies are associated with monomer preparations from petroleum based phenols including Bisphenol-A (BPA) associated globally with various health concerns.<sup>11,12</sup> Bio-based monomer precursors extracted from natural products are highly desirable molecular building blocks for advanced engineering polymers that offer alternative approaches to molecular design with comparable or superior properties.<sup>13</sup> CE's comprise a family of resins that have thermal properties exceeding epoxies. It has been shown that biobased cyanate ester resins may have high temperature stability and performance that may meet or exceed conventional petroleum-based resins.<sup>14</sup> Considering polymer choice is critical for composites in demanding applications such as high temperatures, biobased cyanate esters have the potential to not only decrease the weight of aerospace components, but also may configure components with decreased flammability and higher use temperature compared epoxies.

## **1.2 Cyanate Ester Monomers**

The designation CE is used to characterize monomers and oligomers with reactive (Ar-O-C≡N) functional groups.<sup>15,16,17</sup> The chemical structure of a difunctional monomer is generally described as shown in Figure 1.1, where R may be hydrogen atoms or allyl groups. Furthermore, the bridging group can be a variety of structures including, but not limited to, alkyl, cycloaliphatic, or aromatic. Cyanate ester monomers maintain an extraordinarily low toxicity with LD<sub>50</sub> value greater than 3 g/kg, which is comparable to

table salt (~4 g/kg). Monomers are neither corrosive to eyes nor skin irritants nor sensitizers.<sup>4</sup> Moreover, there is a push for high-performance matrices synthesized from sustainable and renewable sources, complementing research effort of renewable chemicals and fuels.<sup>18</sup>

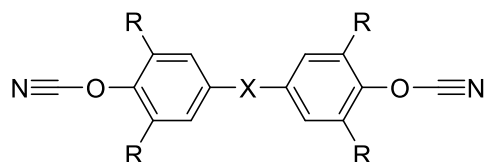


Figure 1.1 *General chemical structure for a difunctional commercial cyanate ester of cyanic acid and bisphenols.*

CE monomers with two or more functional groups will homopolymerize from catalysis or from the addition of heat to form a crosslinked polycyanurate network. This category of thermosetting polymers is often used for applications that necessitate high performance, typically within the aerospace and electronics industry. Polycyanurates have found special applications in these fields due to superior glass transition temperature ( $T_g$ ), dielectric constant and loss, radar transparency, low moisture absorption, and low outgassing.

Grigat and Putter were at Bayer AG in the 1960s when they first published the synthesis of CEs, by reacting a phenolic compound with cyanogen chloride in the presence of a base, as shown in Figure 1.2.<sup>15,16,17</sup> In this report, the authors noted a near-quantitative yield of monomers without the presence of side products.

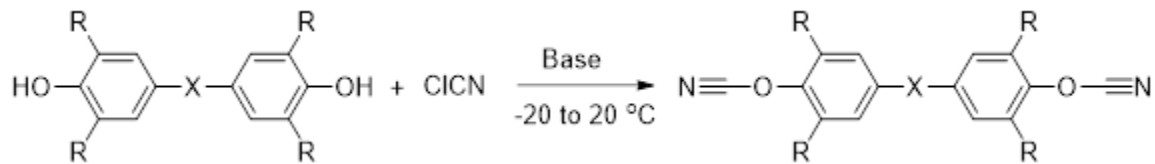


Figure 1.2 *General reaction scheme for cyanate ester monomer synthesis.*

Alternative to cyanogen chloride, cyanogen bromide may be utilized. The bromide compound takes the form of a solid and is especially useful for lab scale syntheses, considering it takes the physical form of a solid and is easier to handle than a gas. For example, it can be dissolved in solvent. It should be mentioned that there is extreme hazard of handling cyanogen halides, which may explain the small number of companies that produce CE's on an industrial scale and high cost. Conventional methods of synthesis involve the low temperature reaction of a cyanogen halide with a phenol in the presence of a base.<sup>19</sup> In most studies tertiary bases are utilized to generate a phenoxide, which subsequently reacts with the cyanogen halide. The eliminated bromide ion forms a triethylammonium hydrobromide salt, which is conveniently removed via filtration and/or a water wash.

When synthesizing CE monomers, care must be taken to avoid the formation of side products. An important consideration is that one should avoid an excess of phenoxide, which may result in formation of an undesirable imidocarbonate side product (Figure 1.3). Loss of product may be avoided via the slow addition of the base to the premixed phenol and cyanogen halide, to favor the swift reaction between the cyanogen halide and phenoxide.

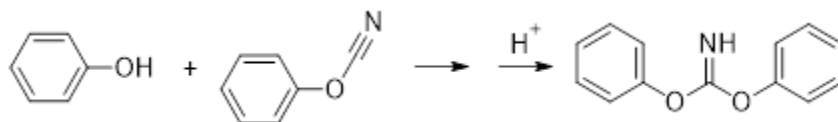


Figure 1.3 *An excess of phenoxide results in the formation of an imidocarbonate.*

Another key strategy to avoid loss of product is to maintain a low reaction temperature. The objective is to suppress the competition between the formation of cyanate groups and an undesirable von Braun reaction that produces a byproduct. More



specifically, the von Braun reaction involves the reaction of cyanogen bromide with a tertiary amine which yields an alkyl bromide and a disubstituted cyanamide. The diethylcyanamide takes the form of a volatile liquid which has been shown to cause voids and outgassing when exposed to high temperatures during cure.<sup>20</sup> To this end, vigorous mixing of the reaction during the dropwise base addition is critical to avoid localized hotspots resulting from the exothermic deprotonation of phenolic moieties.



Figure 1.4 *During the von Braun reaction cyanogen bromide reacts with a tertiary amine yielding an alkyl bromide and a disubstituted cyanamide.*

When considering the synthesis of cyanate esters, the reaction scale plays an important role on the synthetic route. As has been mentioned previously, both the chlorine and bromine cyanogen halides may be used for a cyanation reaction. For instance, cyanogen bromide is more accommodating for a laboratory scale synthesis since it is a solid, which is convenient to weigh and transfer to a reaction vessel. On the other hand, cyanogen chloride is easier to deliver to a reactor during large scale synthesis as it takes the form of a liquid or gas. While there is a chemical advantage to using each compound for varying reaction scales (convenience), both are toxic blood agents. While the cyanogen chloride is more difficult to confine, it should be recognized that it poses an apparent advantage, since it has been reported that reactions with this cyanogen halide results in a considerably lower quantity of the diethylcyanamide byproduct. More specifically, the larger amount of the byproduct during reactions with cyanogen bromide disturbs the cyanogen halide to phenol stoichiometry, and thereby results in a complicated separation to remove diethylcyanamide and unreacted phenol. The

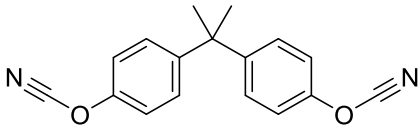
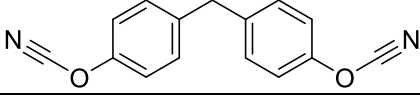
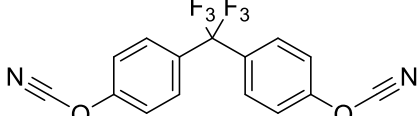
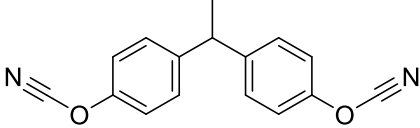
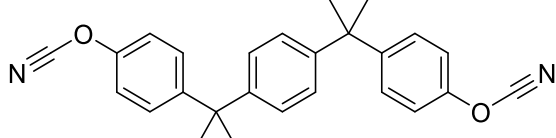
separation of unreacted phenol is critical, since it is an active hydrogen compound which is known to catalyze polymerization. While intuitively one may expect that an excess of triethylamine/cyanogen bromide will drive the desirable cyanation reaction to complete conversion, rather it has been shown that the excess reagents will instead increase the amount of diethylcyanamide to be separated.

Another important side reaction that may take place is the formation of carbamates, which occurs from the reaction of cyanate ester with water when exposed to basic conditions or heat. Not unlike phenols, carbamates are an active proton source, and can catalyze polymerization at temperatures lower than pure monomer. To avoid the formation of this impurity one should be careful to keep the cyanate ester product free from moisture and minimize exposure to heat, in particular, when the product contains water. The formation of this side product is less likely at low temperatures. Therefore, it should be emphasized that slow addition of the base is critical for temperature control to avoid hot spots which can encourage the formation of carbamates in the presence of water. Additionally, special care should be taken to dry starting materials prior to executing a cyanation reaction.

### **1.3 Monomer Melt Properties and Molecular Modelling**

Monomer chemical structure has an important implication for the physical and chemical properties of the monomer and final polymer. Table 1.1 shows the chemical structures and select key properties for CE monomers that are widely used industrially. In particular, the rigidity of the monomer generally corresponds to the melting temperature.

Table 1.1 Structures of commercial cyanate esters

Monomer	Trade Name	T <sub>m</sub> (°C)	T <sub>g</sub> (°C)
	AroCy B	79	289
	AroCy M	44	252
	AroCy F	87	270
	AroCy LA	29	258
	XU-366	68	192

One of the most critical properties of thermosetting monomers is the T<sub>m</sub> since it is crucial in choosing a matrix for a particular process or manufacturing environment. Generally, cyanate ester monomers with low T<sub>m</sub>'s have long working life such that the monomer may be easily applied to a substrate for a sufficient amount of time, and are key for techniques such as resin transfer molding and filament winding.<sup>21</sup> Additionally, another motivation for the use of cyanate esters in high-volume quantities is the demand for high performance composite fabrication technologies such as RTM and VARTM. In these cases, if cyanate esters are formulated properly, they demonstrate the lowest viscosity (and high reactivity) compared to all other high temperature thermosetting matrices, with the exception of vinyl esters or unsaturated polyesters.

Optimally, the cyanate ester exhibits a  $T_m$  slightly above room temperature (42 – 67 °C), yet is readily solidified for storage.<sup>22</sup> High  $T_m$  (above 127 °C) makes it difficult to maintain a monomer melt for adequate processing times, without advancing the polymerization. Generally, measurement of monomers by differential scanning calorimetry is a common way to quantify  $T_m$  and indicate candidates for good processability. However, the main experimental difficulty is in the prohibitively expensive and time-consuming synthesis and purification, which is not trivial and requires specialized synthetic training. Expedient computational prediction of  $T_m$  could substantially facilitate the thermosetting polymer selection process and inspire the molecular design and synthesis of new cyanate esters for CFRP applications.

Atomistic molecular dynamics (MD) simulations of polycyanurate monomer melt properties have primarily focused on wettability<sup>23</sup> and energetic rotational barriers<sup>22,24</sup> to understand structure-property relationships. Ghiassi et al. studied the energetic rotational barriers for a series of aryl cyanate esters and demonstrated control of monomer  $T_m$  through manipulation of the entropy of melting, by substituting silicon atoms for carbon atoms.<sup>22</sup> Further understanding of chemical structure effects can be gained from theoretical  $T_m$  calculations for monomers. Another recent work by Harvey et al. examined propyl-bridged di(cyanate ester) monomers, and semiempirical models indicated bulky groups ortho to the bridge connection on the phenyl rings inhibit molecular motion in the melt, thereby increases  $T_m$ .<sup>24</sup> While polymers and composites based on cyanate esters expand to a plethora of applications, little systematic work has been carried out to predict properties for these thermosetting monomers.<sup>23</sup>

$T_m$  can be readily calculated from simulations via direct<sup>25–30</sup> or thermodynamic<sup>31–34</sup> methods. Recently, Zou et al. showed for a Ni-Zr system, the calculation efficiency for a direct voids method was not only higher than thermodynamic calculations, but also ultimately predicted similar  $T_m$  values<sup>35</sup>. A simple example of a direct method is to heat a solid phase until the  $T_m$  is reached, defined by a discontinuous change in density. This temperature is always higher than experimental  $T_m$ . Compared to homogenous nucleation, the degree of superheating can be controlled through the addition of a heterogeneous interface, such as a void, which can reduce the free energy of melting.<sup>36</sup>

Currently the literature shows us several examples of studies using a direct void method. For example, Solca et al. reported studies of a direct void method where it was shown with the appropriate number of voids, the calculated  $T_m$  could be taken to be the thermodynamic  $T_m$ .<sup>37</sup> Agrawal et al. extended this work to test the influence of the size, shape, and location of voids on the  $T_m$  of argon. It was found the predicted  $T_m$  is insensitive to the shape of the void, however, is dependent on the number of voids, and best agreed with experimental values with the number of voids in the plateau region of the percentage of voids versus  $T_m$  curve.<sup>28</sup> Many of these early MD studies were directed toward atomic solids. Therefore, some modifications and innovations are needed to compute  $T_m$  of cyanate esters. These monomers are excellent prototypical compounds for testing the feasibility of predicting melt behavior of thermosetting monomers, principally since there is dependable experimental data to validate models available in the literature.

#### **1.4 Polycyanurate Network Architecture**

Subtle variations in monomer chemical structure result in dramatic changes to polymer network architecture and final properties. For thermosetting polymer matrices,

the word “architecture” construes the three-dimensional arrangement of the crosslinked matrix. Small variations in monomer chemical structure and functionality beget a rich variety of network architectures which embody diverse thermal and mechanical properties. Polycyanurate network architectures develop through a step-growth process starting with the addition of heat.

As the polymerization progresses, the system transforms from a liquid to a gelled network, and finally to a glassy solid. More specifically, liquid thermosetting monomers cure until the network molecular weight approached infinity; which is termed the gel point. The cyanate ester functional groups proceed to react until the  $T_g$  of the matrix is higher than the cure temperature, i.e. vitrification. In this respect, motions of chain segments are obstructed, such that remaining cyanate ester functional groups are unable to progress the polymerization. Accordingly, the architecture of the network is fixed in the form it took at the start of vitrification. Although some additional curing may occur after vitrification, there but a slight impact on network architecture.

The unique polymer framework is made up of cyanurates, or oxygen linked triazine rings, and connected by bisphenol ethers. More specifically, this addition polymerization proceeds from the cyclotrimerization reaction of the  $-O-C\equiv N$  functional group. Figure 1.5 shows the cyclotrimerization reaction. Oligomers and polymers exist as hard solids, semisolids, or liquids. Accordingly, during the cure the concentration of triazine rings increases, and so does the aromaticity. The high concentration of aromatic triazine rings is stabilized from the electron delocalization in the local  $\pi$ -systems.<sup>38,39</sup> The resulting aromatic backbone is highly rigid with restricted chain mobility yielding a unique high modulus polymer network with outstanding mechanical properties at extreme

elevated temperatures.<sup>40,41</sup> This cyclotrimerization is considered to rationalize the uncommon combination of low viscosity at practical processing temperatures, yet formidable  $T_g$ s of the cured matrix. This fundamental combination of physical properties is the crucial advantage of cyanate esters for high temperature composite applications compared to epoxide-amines.

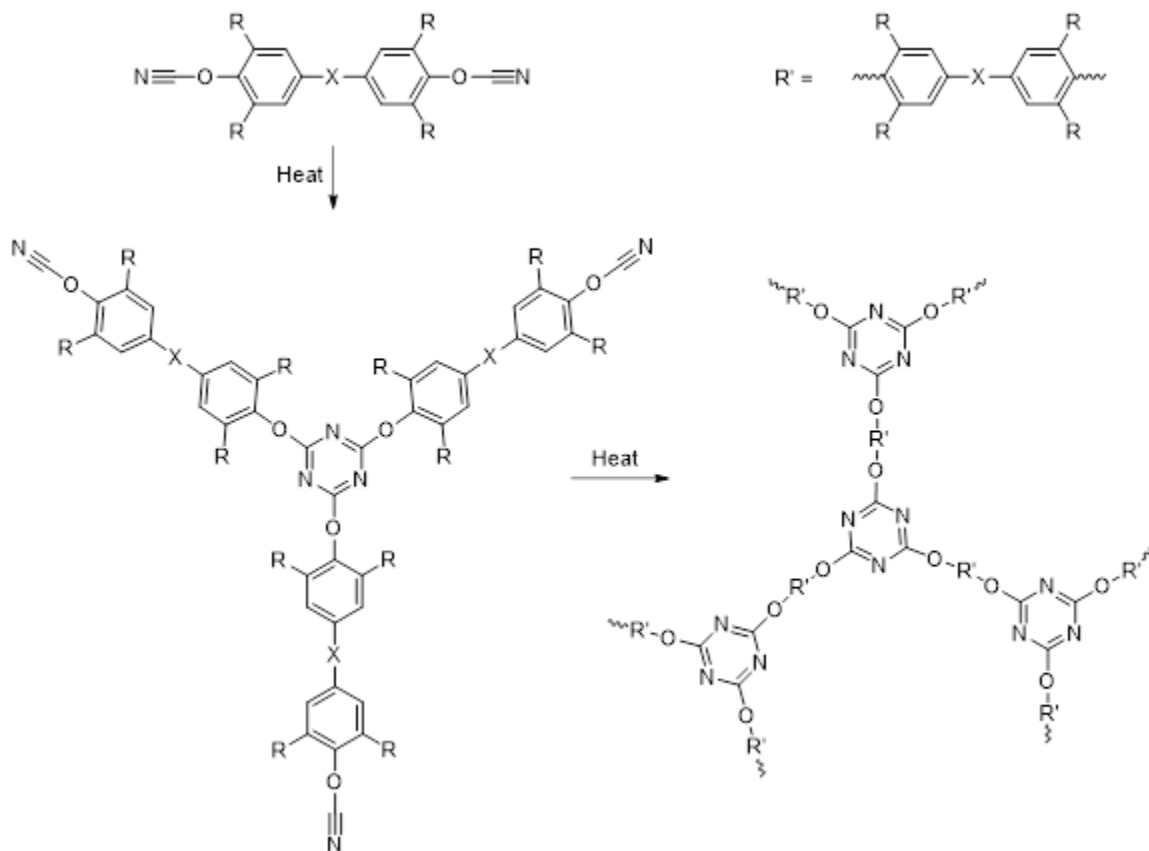


Figure 1.5 Addition polymerization reaction forms triazine rings.

In particular, the amalgamation of elements such as: 1) an increase in aromaticity with cure, 2) weak dipoles, 3) interruption of crystallinity with un-symmetric bisphenol moieties are responsible for the good processability of these high glass transition temperature matrices for applications such as resin transfer molding, vacuum assisted resin transfer molding, and filament winding. The unique aryl polycyanurate system and -

OCN chemistry created after polymerization create unique properties which can be augmented through variation of the polyphenol backbone chemical structures.<sup>8</sup>

The kinetics of cyanate ester polymerization was studied by Bauer et al. and it was reported that phenolic impurities in cyanate esters initiated polymerization in an autocatalytic process.<sup>42</sup> This multistep process is initiated by the ArOH impurities, which can catalyze the cyclotrimerization to triazine rings. Following this, the ArOCN will react with the ArOH group catalyzed by the formed triazine ring, which forms the carbonic ester imide (Figure 1.6). Finally, this carbonic ester reacts with another two OCN groups, resulting in a triazine ring and an ArOH.<sup>19</sup> As mentioned previously, in the second step the ArOCN reacts with a ArOH, which propagates the polymerization reaction up until the ArOCN are all reacted.

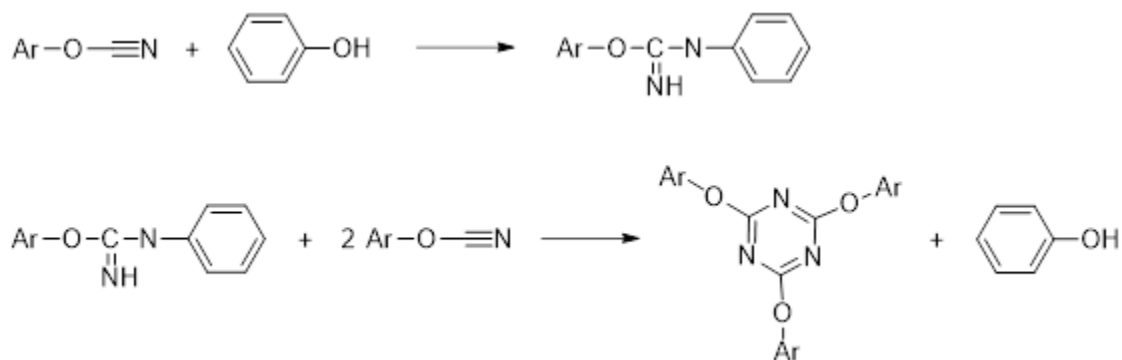


Figure 1.6 Cyanate ester groups are polymerized by phenol in the monomer.

### 1.5 Polycyanurate Degradation and Char Formation

The glassy polymer network architecture of thermosets is inherently related to advanced composite performance (and flame retardance), since the continuous matrix phase is in immediate contact with the external environment. When composites are exposed to extreme temperatures, the exposed polymer matrix absorbs and dissipates heat through endothermic bond breaking processes, which can be detrimental to key



mechanical properties of the matrix. While flame retardant additives have been developed, the limitations for wider adoption of halogenated molecules include bio-accumulation which threaten the environment and human health.<sup>43</sup> These limitations must be overcome with the development of novel polymers with inherent non-flammable properties. Key to the advancement of these polymers is a fundamental understanding of the mechanisms of polymer degradation.

Frequently, organic polymers are flammable and combustion takes place in a sequence of events. This process begins as the polymer is exposed to high temperatures such that it begins to degrade and subsequently release combustible gasses. If the network is exposed to severe heating, pyrolysis occurs, which is a form of thermal degradation. At these high temperatures the kinetic energy of the molecules is high enough to traverse the energy barrier for bond dissociation and vaporization of high and low molecular weight gaseous fragments such as ammonia, carbon monoxide, methane, hydrogen, acetylene, hydrogen cyanide, carbon dioxide, water, nitrogen, and various free radicals. Upon ignition of the flammable gasses, the temperature continues to increase until enough combustible gasses are released to self-sustain, with sufficient oxygen to maintain the fire. In some instances, the combustible gasses for a polymer type have a high concentration of monomeric species on account of depolymerization of polymer chains. Furthermore, monomers may decompose to lower molecular weight combustible products. In instances where depolymerization does not occur, the generation of combustible gasses may be generated from surface oxidation. A representation of polymer burning is shown in Figure 1.7, which shows the diffusing gasses being combusted which causes heat radiation that sustains pyrolysis.

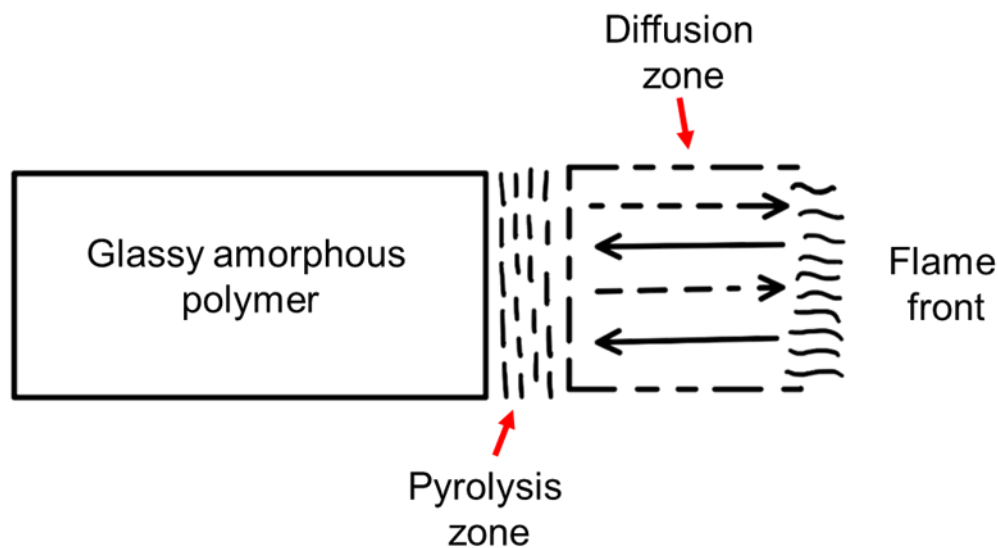


Figure 1.7 *Combustion of a glassy amorphous polymer combustion, where solid black arrows represent heat flux and broken black arrows represent gas diffusion.*

While polyethylene is a polymer that is readily combusted, polymers that possess aromatic structures provide an example of degradation where complete combustion may be prevented. Polymers containing aromatic backbones may be converted into a carbonaceous char when they are burnt, which forms a protective barrier during burning that improves fire resistance.<sup>44,45</sup> In this respect, with continued high thermal exposure, the outer polymer surface densifies to form a thick solid residue. Through this process, thermal protection can be achieved with the formation of a char surface with superior thermal stability which serves as an insulate layer.<sup>46</sup> Provided that the char remains intact, a network's resistance to thermal and chemical ablation will govern lifetime and performance. Chemical structure and network architecture is known as a primary determinant of thermal stability and degradation properties in polymers. For example, for networks with  $sp^3$  hybridized hydrocarbons, the bond dissociation energy is low compared to the other unsaturated networks, which affects thermal stability.<sup>47</sup> A

comprehensive knowledge of the effect of monomer chemical structure and network architecture on polymer degradation and flammability is critical. Only with insight into the degradation processes can we then rationally design polymers with improved thermal properties.

Chemical structure and network architecture is known as a primary determinant of thermal stability and degradation properties in polymers. As such, chemical approaches to degradation and fire behavior, including analyses of degradation processes have proven useful to elucidate trends regarding network architecture and thermal/thermooxidative stability. Early work to study the degradation of polycyanurates at elevated temperatures in air and inert atmosphere utilized the following representative compounds: diphenyl cyanurate, triphenyl isocyanurate, cyanuric acid, and triphenyl-*s*-triazine. From the chromatography and mass-spectroscopy experiments it was concluded that the main degradation products were carbon dioxide, carbon monoxide, phenol and cyanuric acid.<sup>39</sup> This study, among others, resulted in a degradation mechanism that commences with the cleavage of ester linkage followed by the decomposition of the triazine ring through both homo- and heterolytic reactions. Interestingly, it was also found that the incorporation of large side groups on the polycyanurate backbone somewhat represses hydrolysis of the ester linkages early in the decomposition reaction.

Further research has established the degradation of polycyanurates as follows: 1) indiscriminate chain scission, along with crosslinking of the polymer backbone from 400 to 450 °C without a substantial loss of mass, 2) decyclization of the cyanurate ring and the release of small organic molecules from 450 to 500 °C (primary solid residue formed), and 3) degradation of this primary residue and the evolution of hydrogen and

alkenes, leaving behind a carbonaceous char with unconsumed oxygen and nitrogen (Figure 1.8). On the other hand, thermogravimetric experiments in air (in the presence of water) have shown that degradation begins sooner, at 350 to 420 °C with the hydrolysis of the oxygen bond attached to the triazine ring.<sup>48</sup> Furthermore, it has been shown that the char yield is roughly proportional to the  $T_g$  along with the degree of unsaturation of the thermosetting monomer.<sup>49</sup> Not unrelated, the char produced (30 to 60%) is roughly proportional to the concentration of aromatic groups in the polymer backbone. This carbonaceous char is made of carbon, hydrogen, nitrogen, and oxygen in relative abundance of C/H/O/N = 15/4/2/1. Since the combustion temperature and thermal stability of this class of polymers are approximately independent of backbone architecture, the combustibility is contingent on char yield and char formation.<sup>48,50</sup>

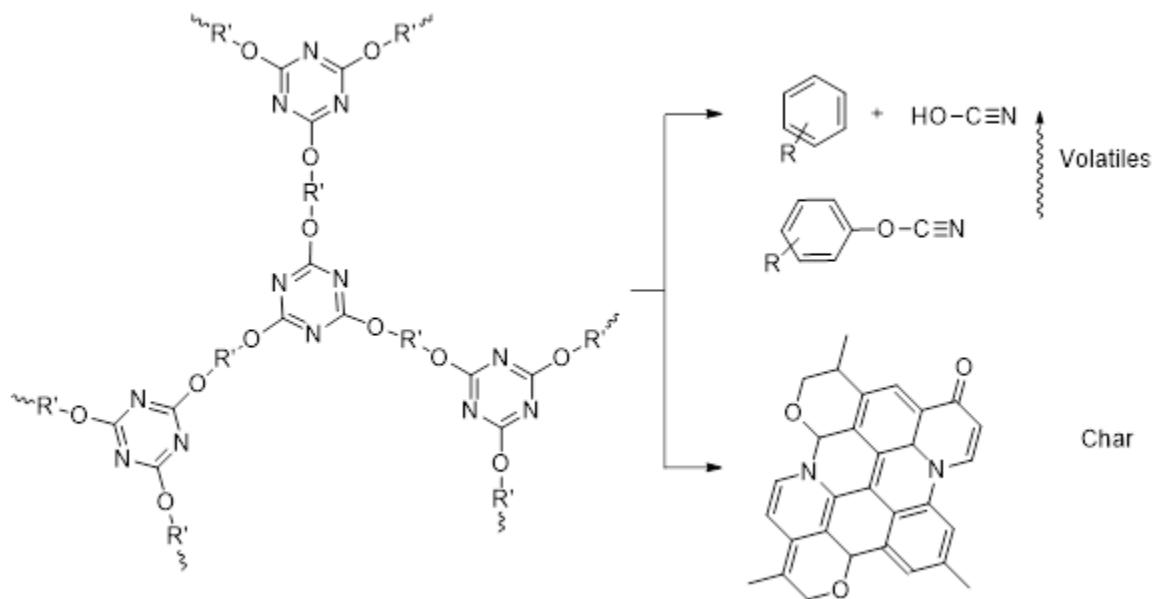


Figure 1.8 Polycyanurate thermal degradation reactions.

With respect to long-term high temperature air exposure, polycyanurates may exhibit swelling and blistering. This degradation and swelling is believed to be due to

carbon dioxide, which was formed when unreacted cyanate ester functional groups react with water to form carbamates, which subsequently undergo decarboxylation yielding carbon dioxide (Figure 1.9).<sup>4</sup> Therefore, other than chemical structure, the degree of polymerization also governs thermal stability.

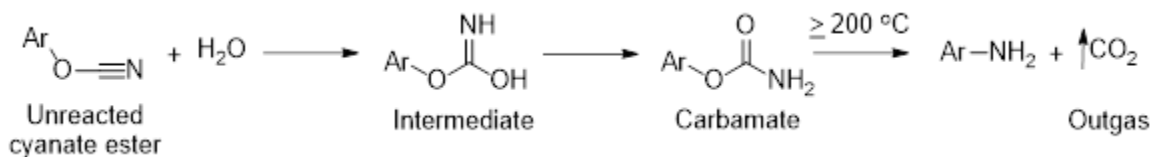


Figure 1.9 *Thermo-oxidative degradation of polycyanurates.*

## 1.6 Sustainable Cyanate Ester Blends

A comprehensive understanding of chemical structure and network architecture of biobased cyanate esters blends is critical to predict processability and thermomechanical properties. While polycyanurates are an important class of high-performance polymers, limitations include unsustainable starting materials, high brittleness<sup>10</sup> and prohibitively high cure temperatures with short processing windows.<sup>4</sup> For example, tricyanate esters (Primaset PT-306) offer excellent thermomechanical properties, but are difficult to process due to high  $T_m$ . Conversely, 1,1-bis(4-cyanatophenyl) ethane (LECy) is a low viscosity liquid at room temperature, which is favorable for composite fabrication, but the thermomechanical properties are inferior to tricyanate esters. It is well known monomers with higher functionality ( $f \geq 3$ ) tris-phenol based CE monomers, form polycyanurates with enhanced thermal stability,<sup>51,52,53</sup> however, they may be difficult to process. While several new cyanate ester monomers with a variety of functionalities (and bulk properties) have been developed, it is important to realize is that co-cured networks may also bring about advantageous properties. In this respect, in addition to great

homogeneity of cyanate ester blends, synergistic interactions (difference in properties from linear rule of mixing) may advance properties relative to the homopolymer networks.

More contemporary concerns/drawbacks associated with CE and other composite matrix polymers such as benzoxazines and epoxies are associated with monomer preparations from petroleum based phenols including Bisphenol-A (BPA) associated globally with health concerns.<sup>11,12</sup> Bio-based monomer precursors extracted from natural products are highly desirable molecular building blocks for advanced engineering polymers that offer alternative approaches to molecular design with comparable or superior properties.<sup>13</sup> For example resveratrol, cited for potential BPA replacement in network polymers, is a trifunctional polyphenol extracted from wine, legumes, and Japanese Knotweed (*Polygonum cuspidatum*)<sup>54</sup> and is known to protect against diseases such as Alzheimer's,<sup>55</sup> diabetes,<sup>56</sup> and cancer in mammals.<sup>57</sup> In 2013 a high performance trifunctional cyanate ester monomer from a sustainable phenol, *trans*-resveratrol was reported, with a high  $T_g$  ( $>350$  °C) and excellent char yield in air (71% at 600 °C).<sup>58</sup> On the other hand, the high melting temperature (165 °C) precluded this system from use in processing techniques such as filament winding and RTM. It was later found in 2017 that the more thermodynamically stable *trans*-resveratrol undergoes an isomerization reaction to *cis*-resveratrol when irradiated with UV light. Furthermore, tricyanate monomer cisResCy, maintained the excellent thermomechanical properties, but the melting temperature was nearly 100 °C lower than the *trans* isomer.<sup>14</sup> It should also be mentioned that the resveratrol-based polcyanurates demonstrated an ~50% increase in char yield measured under nitrogen at 600 °C, compared to BPA-based commercial CE polymer

standards.<sup>59,60</sup> In this example, the observed highly desirable increase in char yield for certain applications was attributed to the higher crosslink density and stilbene structure, highlighting how bio-based precursors provide new opportunities for improved polymer molecular design.

Reactive diluents and blends of multiple bio-based monomers with varying functionality can be investigated to alter monomer melting temperature ( $T_m$ ), polymerization onset temperature ( $T_o$ ), polymerization peak exotherm temperature ( $T_p$ ), and polymerization enthalpy ( $\Delta H$ ) in an effort to enhance processing and process control of thermoset polymers. Cardanol is a 15-carbon unsaturated alkyl-chain substituted liquid phenol readily extracted from cashew nut oil (*Anacardium occidentale L*).<sup>61</sup> Due to the availability and low cost, this molecule is an attractive candidate to insert sustainable natural mono-phenol precursors for equivalent or improved performance. The phenolic moiety of cardanol is an outstanding biobased reactive modifier that can undergo cyanation and subsequently react with other CE groups via a cyclotrimerization polymerization to form a crosslinked network. Since cardanol is an oily liquid at room temperature, it potentially serves as a reactive diluent when blended with highly crystalline solid resveratrol-CE monomers to modify  $T_m$  and other critical polymerization temperatures for further enhanced processability and process control.

## 1.7 Research Overview

The objective of the following dissertation is to study the essential structure-property-performance associations between monomer structure, glassy matrix architecture, and the thermal stability in high performance polycyanurates. It should be mentioned a primary research thrust is to compare BPA-based polycyanurates to our

novel formulations from sustainable feedstocks. This work builds on previous research by evaluating thermomechanical properties in complex polycyanurate thermosetting matrices and by the flourishing interest in matrices based on sustainable and renewable plant sources. These environmentally friendly high-temperature polymer matrices have the capacity to not only improve the performance of aerospace polycyanurate materials, but also of dramatically lowering the energy footprint for the fabrication of high performance composite materials. Contemporary polycyanurate systems are reliant on unsustainable starting material, and moderate char yield. Their net carbon emissions and thermal stability could be improved if the alliance between monomer chemical structure, network architecture, thermal stability, and flame-retardant properties were better understood.

This dissertation studies structure-property-performance relationships in sustainable polycyanurate systems relevant to high-temperature materials. In chapter III the relationship between monomer chemical structure and melting temperature are evaluated by molecular dynamics simulations. In Chapter IV, the neat monomer properties and cure kinetics are evaluated to demonstrate the connection between cure kinetics, network formation, and thermomechanical properties. Furthermore, in chapter IV, combustion properties and char residues are characterized for difunctional and multifunctional polycyanurates. These properties are interpreted in light of molecular architecture and degree of unsaturation of polycyanurates. In Chapter V cyanate esters based on cardanol and resveratrol are formulated and to study blend behavior for processability and thermomechanical cured network properties. The effects of varying monofunctional content of the CardCy CE blended within ResCy was studied to quantify



polymerization behaviors including thermomechanical and thermal degradation analyses to demonstrate sustainable polycyanurates with tunable polymerization behaviors, thermal, and mechanical properties for high performance applications. In summary, this work presents continuation in effort towards sustainable cyanate ester polycyanurates with high-performance thermomechanical properties for integration as matrix polymer networks into advanced aerospace composites.

## CHAPTER II – EXPERIMENTAL

### 2.1 Materials

The following materials were used as received: Biosynthetic *trans*-resveratrol (>98%) was provided by Evolva and used as received. Cashew seed oil was obtained from Cardolite. Diethyl ether, methanol (MeOH), tetrahydrofuran (anhydrous), hexanes, ammonium hydroxide, hydrochloric acid (HCl), and activated charcoal were obtained from Fisher Scientific and used as received. Triethylamine (TEA) was obtained from Millipore Sigma and used as received. Cyanogen bromide (BrCN) was obtained from ACROS Organics and used as received. All NMR specimens were dissolved in CDCl<sub>3</sub> with the  $\delta$  7.27 solvent reference. Caution, reactions involving BrCN are hazardous as the reagent is extremely toxic by ingestion or skin absorption. Due to the high vapor pressure at room temperature, inhalation is a major toxic route, so this reagent must be handled inside a well-ventilated fume hood.<sup>62</sup>

The cyanate ester monomers 2'-(4-cyanatophenyl)propane (BADCy) and 4,4'-(ethane-1,1-diyl)bis(cyanatobenzene) (LECy) were supplied by Toray and used as received. Their structures are shown in Figure 2.1.

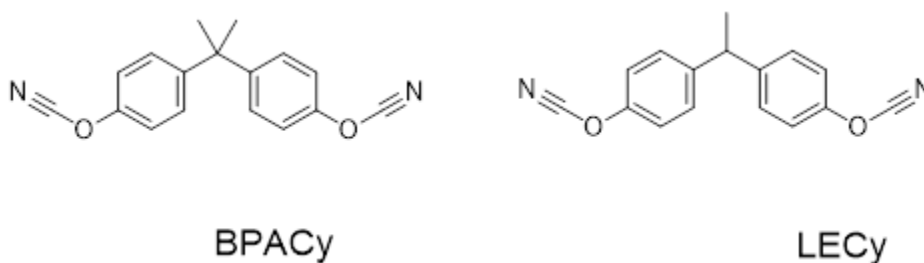


Figure 2.1 *Cyanate ester monomer structures.*

## 2.2 Synthesis

In 2013 a trifunctional CE resin synthesized from biosynthetic *trans*-resveratrol was reported to polymerize to a network with high  $T_g$  ( $>350$  °C) and char yield in air (71% at 600 °C).<sup>58</sup> It was later discovered in 2017 the *cis*-resveratrol derived cyanate ester resin yielded networks with comparable thermomechanical properties, yet, exhibited a melting temperature nearly 100 °C lower than the *trans* analogue, greatly improving processability.<sup>14</sup> Our syntheses of *cis*-resveratrol (Figure 2.2) and cisResCy (Figure 2.3) followed cyanation reaction preparations described in 2017 by Cambrea et al.<sup>14</sup> Despite this innovation, it was of interest to further investigate synergistic structure property relationships by formulating 100% biobased resins with tunable material properties.

### 2.2.1 Synthesis of cisResCy Monomer

A borosilicate flask (1 L) equipped with magnetic stirring bar, reflux condenser, and N<sub>2</sub> bubbler was charged with *trans*-resveratrol (10.44 g, 45.8 mmol) and MeOH (660 mL). The reaction setup was mounted in a Rayonet<sup>TM</sup> photochemical reactor with long wavelength bulbs (k5350 nm) for 24 h. The products were protected from light by covering with aluminum foil during the workup steps. The highlighter yellow solution was cooled to ambient temperature and the solvent was removed with rotary evaporation. The yellow solid was dissolved in diethylether and filtered through a glass fritted filter, to yield a *cis*-resveratrol filtrate. The solvent was removed with rotary evaporation, yielding *cis*-resveratrol as a pale yellow powder. Yield: 8.4 g (81%).  $T_m$ : 174 C. <sup>1</sup>H NMR (600 MHz, CDCl<sub>3</sub>-d<sub>6</sub>  $\delta$ , ppm): <sup>1</sup>H NMR (600 MHz, DMSO-d<sub>6</sub>,  $\delta$ , ppm): 9.6 (OH), 9.24 (2x OH), 7.06 (d, 2H), 6.62 (d, 2H), 6.37 (d, 1H), 6.29 (d, 1H), 6.11 (d, 2H), 6.06 (t, 1H).

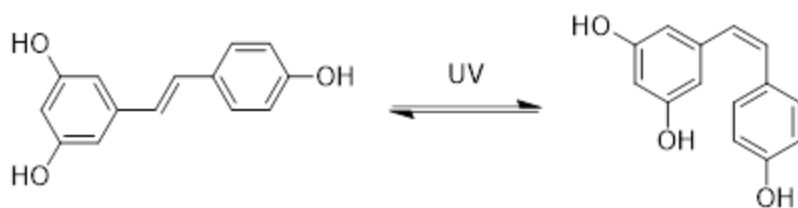


Figure 2.2 Isomerization of *trans-resveratrol* to *cis-resveratrol*.

A 3 L reaction vessel equipped with an overhead mixer was charged with cyanogen bromide (70.5 g, 0.67 mol, 3.8 eq) and anhydrous THF (160 mL). The mixture was cooled in an acetone/ dry ice bath under a slow stream of nitrogen, and *cis-resveratrol* (40 g, 0.18 mol, 1 eq) with anhydrous THF (390 mL) was added to the reaction flask. Triethylamine (78.2 mL, 0.56 mol, 3.2 eq) dissolved in anhydrous THF (78.2 mL) was added dropwise resulting in a cloudy beige mixture. The reaction was stirred for 3 h and then allowed to warm to 0 °C. A large amount of white precipitate (triethylammonium hydrobromide) was subsequently removed via filtration. The organic product was washed with water, dried (MgSO<sub>4</sub>), and the solvent was removed under reduced pressure to give ResCy. The product was further purified by recrystallization from THF and hexanes to yield white needle crystals. Yield: 36 g (68 %). T<sub>m</sub>: 84 °C. <sup>1</sup>H NMR (600 MHz, CDCl<sub>3</sub>-d<sub>6</sub> δ, ppm): 7.51 (s, 1H), 7.41 (s, 4H), 7.27 (s, 2H), 6.94 (d, 1H), 6.82 (d, 1H).

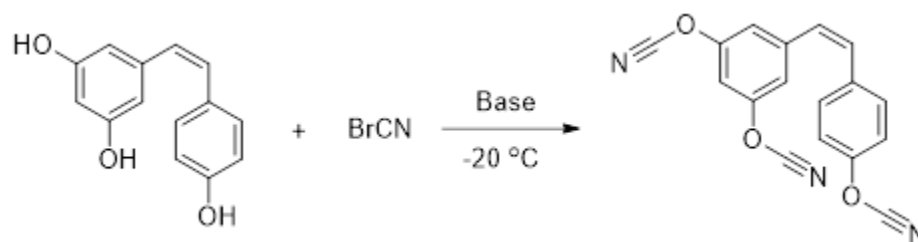


Figure 2.3 Cyanation of *cis-resveratrol* to *cisResCy*.

### 2.2.2 Synthesis of CardCy Monomer

Crude cardanol (100 g) was diluted in methanol (350 mL) and ammonium hydroxide (190 mL, 25%). The mixture was vigorously stirred for 15 mins, after which the intermediate was extracted with hexanes (4x). The organic extract was washed with HCl (100 mL, 5%) and water (100 mL). The organic layer was then stirred with activated charcoal (10 g) and then filtered. The filtrate was dried, and the solvent was removed under reduced pressure to yield the product as an oily red liquid. Yield: 37.4 g (93.5%).  $^1\text{H}$  NMR (400 MHz,  $\text{CDCl}_3-d_6$ ,  $\delta$ , ppm): 7.74 (t, 1H), 7.37 (t, 1H), 7.26 (t, 2H), 6.42 (m, 1H), 5.95 (m, 4H), 5.68 (m, 2H), 2.62 (t, 2H), 2.19 (s, 2H), 1.98 (s, 16H), 1.53 (t, 3H).

Purified cardanol (10 g, 33.05 mmol, 1.0 eq) and CNBr (5.25g, 49.58, 1.5 eq) was dissolved in 135 mL of anhydrous diethyl ether (135 mL) and cooled to  $-20\text{ }^\circ\text{C}$ , and TEA (4.83 mL, 34.7 mmol, 1.05 eq) dissolved in anhydrous diethyl ether (5 mL) was added dropwise to the reaction. The reaction was stirred vigorously for 3 h while warming up to  $0\text{ }^\circ\text{C}$ , resulting in a cloudy beige mixture. The salt (triethylammonium hydrobromide) was filtered off, and the product was washed with water, dried ( $\text{MgSO}_4$ ), and the solvent was removed under reduced pressure. The product was dissolved in hexanes and passed through a short silica plug, after which the solvent was removed under reduced pressure (Figure 2.4). Yield: 7.7 g (71.92%).  $^1\text{H}$  NMR (600 MHz,  $\text{CDCl}_3-d_6$ ,  $\delta$ , ppm): 7.37 (1, 1H), 7.14 (t, 3H), 5.85 (m, 1H), 5.38 (m, 4H), 5.06 (m, 1H), 2.82 (m, 2H), 2.67 (t, 2H), 2.07 (m, 2H), 1.65 (t, 2H), 1.35 (m, 15H).

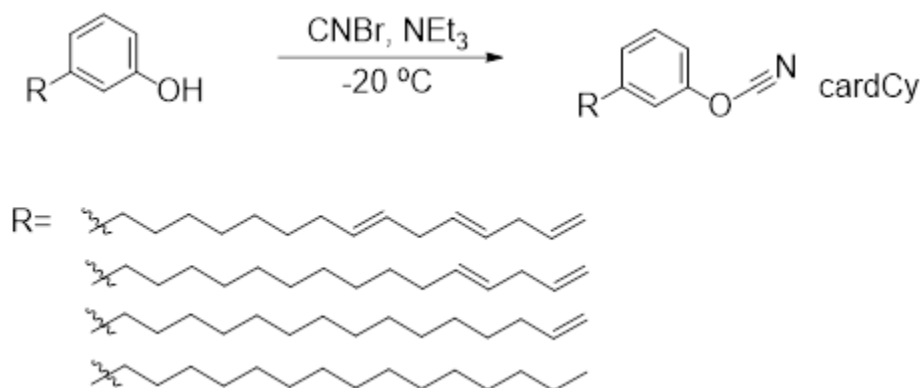


Figure 2.4 *Synthesis of CardCy monomer.*

### 2.3 Sample Preparation

To prepare cisResCy/CardCy formation, CardCy was measured into a round-bottomed flask with a magnetic stir bar and degassed under vacuum using a heating mantle set to 40 °C. Upon sufficient degassing for approximately 20 minutes, cisResCy ( $T_m = 84\text{ }^\circ\text{C}$ ) was added to the liquid CardCy resin. Complete dissolution of cisResCy within CardCy required stirring at 110 °C for approximately 1 h, for optical clarity. When mixing was complete and there was no evidence of bubbles, the heat was removed to allow the resin to cool to room temperature, and then stored in the freezer with a nitrogen headspace for subsequent experiments.

Table 2.1 *Composition of cyanate ester mixtures*

<b>Network</b>	<b>a</b>	<b>b</b>	<b>c</b>	<b>d</b>	<b>e</b>
cisResCy (wt %)	1	0.95	0.90	0.80	0.70
CardCy (wt %)	0	0.05	0.10	0.20	0.30

## **2.4 Characterization**

### **2.4.1 Proton $^1\text{H}$ NMR**

The  $^1\text{H}$ -NMR spectrum was measured on a Bruker 600 Mhz spectrometer with  $\text{CDCl}_3-d_6$  as the solvent.

### **2.4.2 Fourier Transform Infrared Spectroscopy (FTIR)**

Mid- Infrared Spectroscopy (IR) in attenuated reflectance (ATR) mode were recorded using a Thermo Scientific Nicolet 6700 FTIR spectrometer for the frequency range from 4000 to 600  $\text{cm}^{-1}$ . Spectra were measured with a 4  $\text{cm}^{-1}$  resolution. Liquid and solid monomer samples were directly loaded onto the Internal Reflection Element (IRE) crystal.

### **2.4.3 Dynamic Scanning Calorimetry (DSC)**

DSC samples were prepared for polymerizations in aluminum weigh dishes, and DMA samples were cast and polymerized in silicone molds. In the archetypal network preparation the monomer blends were removed from the freezer, heated and degassed in a vacuum oven set to 110  $^\circ\text{C}$  for approximately 20 mins. When clarified, the molten mixture was poured into the appropriate dishes or molds. The samples were polymerized in an inert atmosphere with the following protocol: 160  $^\circ\text{C}$  2h, 180  $^\circ\text{C}$  2h, 200  $^\circ\text{C}$  2h, 220  $^\circ\text{C}$  2h.

Cured and uncured CE samples were analyzed using a TA Instruments Q200 Differential Scanning Calorimeter (DSC). Samples were prepared by sealing (3 – 5 mg) of material in a hermetically-sealed aluminum pan. DSC testing of uncured CE material was conducted using a nonisothermal protocol. The temperature was ramped from 40 to 325  $^\circ\text{C}$  at rates of 5, 10, 15, and 20  $^\circ\text{C}/\text{min}$ . The total heat of the cure reaction ( $\Delta\text{H}$ ) was

calculated from the area under the exotherm curve in the DSC thermogram. Analysis using the Kissinger<sup>63</sup> and Ozawa<sup>64</sup> methods were applied to the DSC data to determine the activation energy of polymerization. Based on the Kissinger method, the activation energy can be obtained from the resulting relation:

$$\ln\left(\frac{\beta}{T_{max}^2}\right) = \ln\left(\frac{AR}{E_a}\right) - \frac{E_a}{RT_{max}^2} \quad (1)$$

Where  $\beta$  = heating rate,  $T_{max}$  = temperature of DSC peak maximum,  $E_a$  = activation energy,  $A$  = pre-exponential factor, and  $R$  = gas constant. By plotting  $\ln(\beta/T_p^2)$  versus  $1000/T_p$ , the activation energy can be calculated from the slope. In addition, the Flynn-Wall-Ozawa method can be represented by the following equation:

$$E_a = \frac{-R}{1.052} \frac{\Delta \ln(\varphi)}{\Delta(1/T_p)} \quad (2)$$

where  $\varphi$  is the heating rate,  $T_p$  is the peak exotherm temperature, and  $R$  is the universal gas constant (8.314 J/mol·K). A plot of  $\Delta \ln \beta$  against  $\Delta(1/T_p)$  yields a slope of  $\Delta \ln \beta / \Delta(1/T_p)$ , which can be used to calculate activation energy. All DSC experiments were run in a  $N_2$  environment with a flow rate of 25 mL/min. The calorimeter was calibrated with an indium standard.

DSC testing of cured CE material was conducted using a nonisothermal protocol. The temperature was ramped from 40 to 325 °C with a heating rate of 10 °C/min. Samples were removed from the oven and quenched in liquid nitrogen after each polymerization stage to prevent advancement of crosslinking reactions. For example, the first sample was removed after 2h at 160 °C. The Degree of Cure ( $\alpha$ ) was calculated from the residual heat of the polymerization reaction using the following equation:

$$\alpha = \frac{(\Delta H_0 - \Delta H)}{\Delta H_0} \quad (3)$$



where  $\Delta H_0$  is the enthalpy of polymerization of the uncured CE monomer and  $\Delta H$  is the residual enthalpy of cure for the material cure at each subsequent stage.<sup>65</sup>

#### 2.4.4 TGA

Thermogravimetric analysis (TGA) was performed on cured polycyanurate material using a TA Instruments Q5000 TGA. Samples weighing 8 to 10 mg. The temperature was ramped from 40 to 600 °C at a heating rate of 10 °C/min under a nitrogen environment. The  $T_{5\%}$  (decomposition temperature) and  $T_{10\%}$  were reported as temperatures at which 5% and 10% weight loss was observed, respectively.

#### 2.4.5 TGA-MS

A TGA-MS TA Instruments Discovery series was utilized for quantification of weight loss and identification of degradation products in both a nitrogen and air environment. The experiments were performed with a 1.1 to 1.9 mg sample size and a 10 °C/min heating ramp rate from room temperature to 900 °C.

#### 2.4.6 Dynamic Mechanical Analysis (DMA)

Dynamic mechanical analysis (DMA), including storage modulus ( $E'$ ) and thermomechanical glass transition temperature ( $T_g$ ) were measured with a TA Instruments Q800 DMA. Experiments were run in tensile mode with a temperature ramp rate of 5 °C/min from 50 to 400 °C, strain of 0.05%, and frequency of 1 Hz. The  $T_g$  was calculated as the peak of the  $\tan \delta$ . The crosslink density ( $\nu_e$ ) of the cured CE's were calculated using the following equation based on the theory of rubbery elasticity:

$$\nu_e = \frac{E_r}{3RT} \quad (4)$$

where E is the tensile storage modulus obtained in the rubbery plateau ( $T_g + 30$  °C), T is temperature in °K of the corresponding storage modulus value, and R is the gas constant.<sup>66</sup>

#### **2.4.7 Rheology**

The complex viscosities of the samples were measured using a TA Ares G2 rheometer with a frequency of 1 Hz and 10% strain. The gap was set to 0.5 mm. Aluminum disposable parallel plates with a 25 mm diameter were utilized for the temperature ramp test with a temperature range from 85 - 150 °C, and ramp rate of 1 °C/min.

#### **2.4.8 Cone Calorimetry**

Samples for cone calorimetry were made by measuring out 80 g of monomer, degassing at 100 °C for 20 mins, and pouring into a silicone mold (10 cm X 10 cm X 2 mm) for subsequent polymerization. Samples were polymerized in a nitrogen atmosphere with the following cure protocol: 160 °C 2h, 180 °C 2h, 200 °C 2h, 220 °C 2h, and 300 °C 30 min. Once fully cured, the samples were somewhat transparent and light amber in color. During the experiment, the exposed material was subject to 50 kWm<sup>-2</sup> of radiant heat flux.

#### **2.4.9 Scanning Electron Microscopy**

Samples were analyzed via SEM using a JOEL JSM 7800f at 5.0 kV. Samples were cut to size with a razor blade to approximately 2 x 2 mm and then mounted onto a post.

#### 2.4.10 Molecular Dynamics Simulations

MD simulations were performed to simulate the solid-to-liquid phase transition of cyanate ester monomers, calculate  $T_m$ , and thereby appraise the quality of the molecular model relative to available experimental values (Figure 2.5).<sup>28</sup> The Schrödinger Materials Science Suite<sup>67</sup> and Desmond<sup>68</sup> were used to for model construction, analysis, and simulation. Simulations were performed in the canonical ensemble with a constant number of atoms, pressure, and temperature (NPT) with a Nosé-Hoover thermostat<sup>69,70</sup> and the Martyna–Tobias–Klein barostat<sup>71</sup> unless otherwise noted. The OPLS3e forcefield was used for all molecules.<sup>72, 73, 74</sup>

We examined four different cyanate ester monomers, with previously reported experimental melting temperatures: 1) 2'-(4-cyanatophenyl)propane (BADCy,  $T_m$ = 355.15 K),<sup>75</sup> 2) 4,4'-(ethane-1,1-diy)bis(cyanatobenzene) (LECy,  $T_m$ = 302.15 K),<sup>51</sup> 3) tris(4-cyanatophenyl)methylsilane (SiCy-3,  $T_m$ = 390.62 K),<sup>22</sup> and 4) bis(4-cyanatophenyl)dimethylsilane, (SiMCy,  $T_m$ = 333.05 K ).<sup>76</sup> The crystal structures of BADCy,<sup>77</sup> LECy,<sup>51</sup> SiCy-3,<sup>22</sup> and SiMCy<sup>22</sup> have also been previously published. The structures for BADCy (Refcode: TACHAG), SiCy-3 (Refcode: WAGWEJ), and SiMCy (Refcode: YERHAF) are available from the Cambridge Structural Database as .cif files.<sup>78</sup> For LECy the crystallographic data was only available as unit cell vectors, so the .cif for BADCy was modified, due to structural similarities. In this instance, a methyl group was deleted from each BADCy molecule in the unit cell and subsequently a simulation cell was constructed from the edited structure. Supercells with specified number of molecules were created by replicating supplied unit cell in all three directions to roughly cubic cell. Simulation cells with 256 molecules (0% voids) and 400 molecules (0% voids) were

constructed. For 256 molecule ensembles (0% voids) LECy had the lowest number of atoms (8192), whereas SiCy-3 had the largest number of atoms (11,264). For larger systems with 400 molecules (0% voids) the number of atoms ranged from 12800 to 17600.

The procedure to simulate the solid-liquid phase transition imitates the process of heating a crystalline solid from low temperature while tracking the change in volume of the system in tandem. To calculate  $T_m$  from MD simulations, researchers have typically used the volume (or density) as a function of temperature.<sup>29, 30, 79, 80, 81, 82, 83</sup> Within this thermodynamic theory of melting, at the melting temperature (constant temperature and pressure), the solid-liquid equilibrium is defined as:

$$\frac{\partial G_s}{\partial P T_m} = V_s \neq V_l = \frac{\partial G_l}{\partial P T_m} \quad (5)$$

where s represents solid properties and l indicates liquid properties. For example, upon the first order melting phase transition there is a discontinuous increase in volume.

We used a void method, put forward by Solca et al.,<sup>37</sup> whereby voids are “added” into the system by deleting a certain percentage of monomers from the source structure. Molecules were selected at random and deleted to prepare supercells with defect concentration ranges from 1% to 10% to allow us to assess the effect of voids on the quality of  $T_m$  calculations with regard to experimental values. The 10% voids upper limit was selected to prevent mechanical destabilization and collapse of simulation cells,<sup>28, 79, 80</sup> which has been previously attributed to excessive number of defects, shear instability, or excessive vibrational motion.<sup>84</sup> An energy minimization step was used to generate optimized geometrical configurations and to provide molecule systems with realistic densities. MD simulations were run stepwise from 150 K specified increments until 600

K was reached. The simulation cells were subjected to an equilibration period of 20 ns at each temperature step, during which properties were elicited.<sup>85</sup>

It should be mentioned that the heating rate influences thermodynamic outcomes,<sup>86</sup> therefore initially two different heating rates (25 K/ 20 ns and 50 K/ 20 ns) were tested to observe the reproducibility of calculated  $T_m$ .

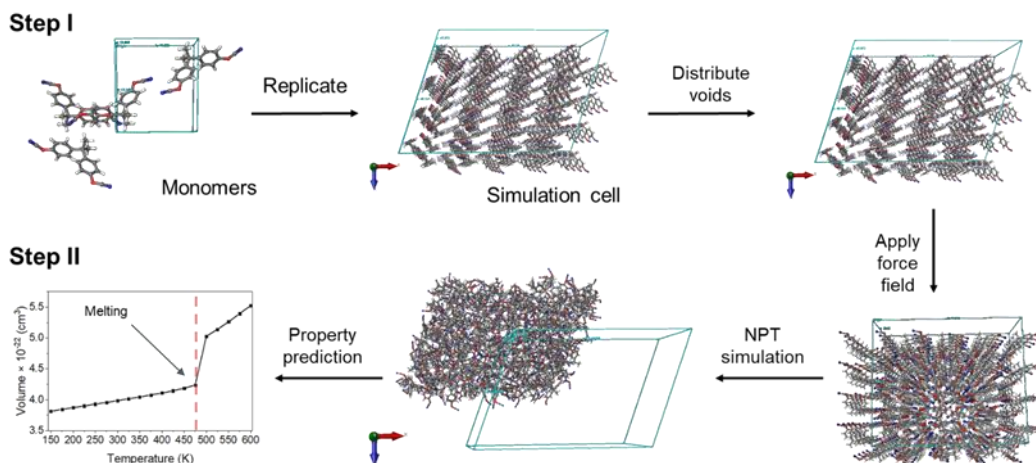


Figure 2.5 MD workflow of melting temperature simulations.

Structural characterization, including the *Orientational Order Parameter* was utilized to describe the solid-to-liquid phase transition. For a given configuration this parameter is defined by:

$$OP = \left(\frac{1}{N}\right)\sum_{i=1,N}P_2(\cos\theta_i) \quad (6)$$

where  $\cos\theta_i$  is derived from the scalar product of a vector for the descriptor (principal moment of inertia) and the vector for the director, and  $P_2(\cos\theta_i)$  is the second order Legendre polynomial,  $(3\cos^2\theta_i - 1)/2$ . The sum is calculated from all descriptor vectors defined for all molecules, and the order parameter is taken as the average value of the Legendre polynomial over all descriptors.  $P_2$  is used so that the order parameter does not distinguish between descriptor vectors in opposite directions.<sup>67</sup> The order parameter

equals 1 when molecules have perfect alignment along the director, which signifies a crystalline lattice in the solid state. This value decreases as the system becomes disordered, and approaches 0 when molecules have isotropic orientations with respect to the director, which indicates liquid-like behavior.<sup>82, 87</sup> The procedure of the calculation consisted of running an annealing simulation below the  $T_m$  ( $T_m - 50K$ ) and above the  $T_m$  ( $T_m + 50K$ ). The simulation cells were subjected to a NVT Brownian dynamics stage for 1200 ps, a NVT MD stage for 1.2 ns at 10 K, and an NPT MD stage for 1.2 ns at the desired temperature to reach an equilibrium value using the MD Multistage Workflow module.<sup>88</sup>

Structural characterization, including the torsion angle describing the orientation of the aromatic rings, relative to the bridging methyl group were calculated using the *Torsion Profile Analysis* module. Trajectories were obtained in an analogous manner to the Order Parameter calculations. For all monomers, trajectory files for systems below and above the  $T_m$  ( $T_m - 50 K$  or  $T_m + 50 K$ ) were used as input for analysis over the simulation time. The SMARTS<sup>89</sup> pattern for the dihedral angle between the methyl carbon on bridging groups and aromatic carbons on the benzene ring was used to define the torsional angle.

## CHAPTER III – MOLECULAR DYNAMICS SIMULATIONS OF CYANATE ESTER MONOMER MELT PROPERTIES

### **3.1 Abstract**

The objective of this work is to computationally predict the melting temperature and melt properties of thermosetting monomers used in aerospace applications. In this study, we apply an existing voids method by Solca et al. to examine four cyanate ester monomers, with a wide range of melting temperatures. Voids are introduced into some simulations by removal of molecules from lattice positions to lower the free energy barrier to melting to directly simulate the solid to liquid phase transition. We validate model predictions by comparing calculated melting temperature against previously reported literature values. Additionally, the torsion and orientational order parameter were used to examine the monomers' freedom of motion to investigate structure-property relationships. Ultimately the voids method provided reasonable estimates of melting temperature while the torsion and order parameter analysis provided insight into source of the differing melt properties between the thermosetting monomers. As a whole, the results shed light on how freedom of molecular motions in the monomer melt state may affect melting temperature, and can be utilized to inspire the development of thermosetting monomers with optimal monomer melt properties for demanding applications.

### **3.2 Results and Discussion**

#### **3.2.1 Melting of Monomers with 0% Voids**

The calculation of monomer melt properties relies on simulations that represent the existing physical systems, and that are supported by empirical data. It is fundamental

to our approach that simulating the systems should take less time compared to synthesizing and measuring properties experimentally. In an effort to reach a good compromise between simulation time and accuracy, we decided to apply a well-known void method<sup>37</sup> to our thermosetting monomer systems: (a) 2'-(4-cyanatophenyl)propane (BADCy), (b) 4,4'-(ethane-1,1-diy) bis(cyanatobenzene) (LECy), (c) tris(4-cyantophenyl) methylsilane (SiCy-3), and (d) bis(4-cyanatophenyl) dimethylsilane (SiMCy).

Three parameters that may affect the calculated  $T_m$  of simulated cyanate ester monomers were tested: system size, heating rate, and percentage voids. Simulations were performed as described in the experimental section. The phase transition temperature of simulated system was estimated by observing a discontinuity, to represent melting, or inflection, to represent a glass transition, from the temperature-volume curve. This is analogous to a  $T_m$  calculation performed on a differential scanning calorimeter performed on themosetting monomers.

The effect of system size on the calculated  $T_m$  was examined (Figure 3.1). We observed that increasing the number of molecules did not cause a significant change in the calculated  $T_m$ , consistent with previous findings.<sup>37</sup> Based on this result, subsequent simulations were conducted with 256 molecules for efficiency. In addition, the optimal heating rate was tested on the 256 monomer systems. Simulations were run with stepwise temperature ramps of 25 K/20 ns and 50 K/20 ns (Figure 3.2). It was determined that there was no significant difference in the phase transition temperature, so the 50 K/20 ns (and 256 mol systems) was a good compromise between the simulation size and heating rate.



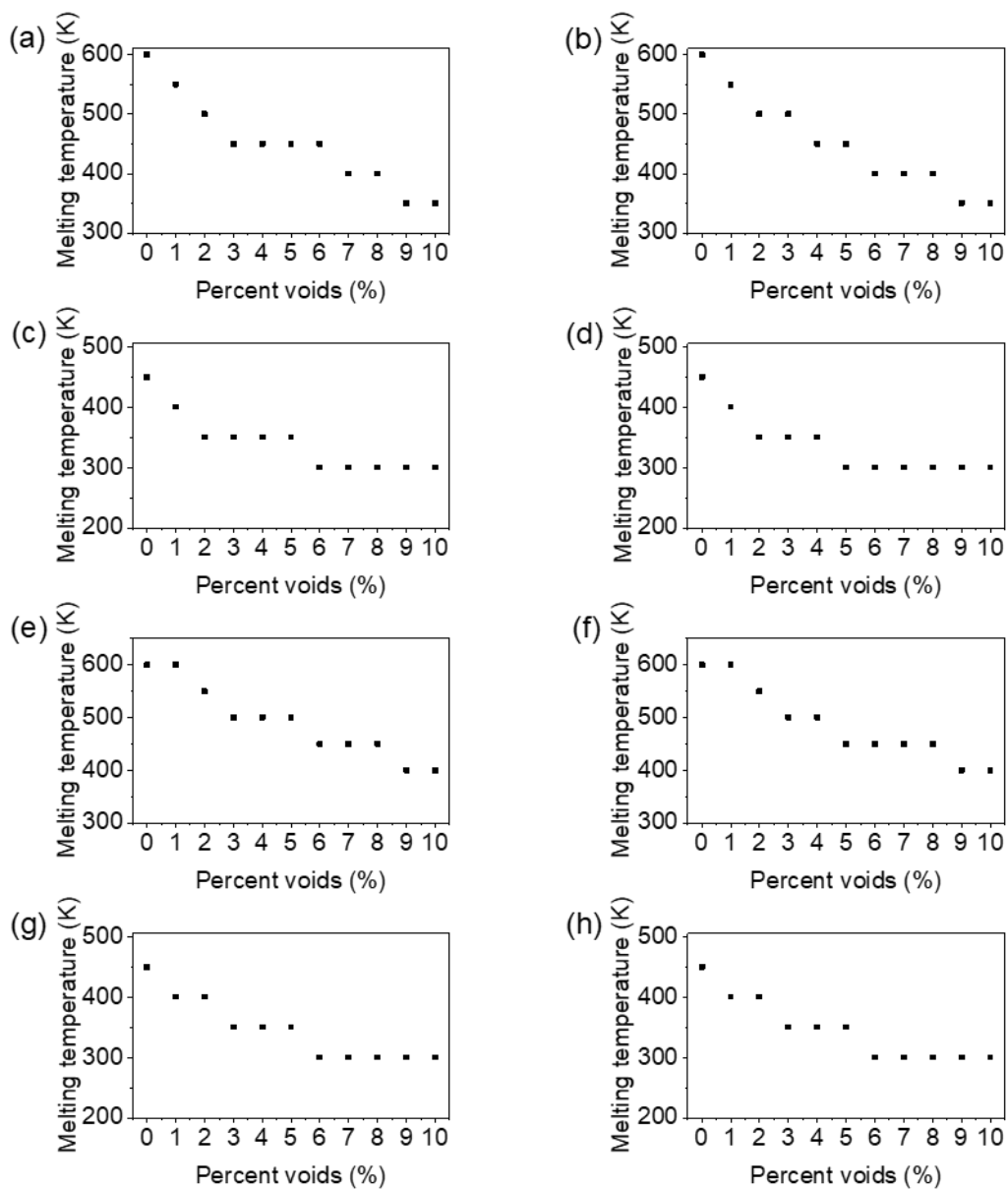


Figure 3.1 The effect of ensemble size on the calculated melting temperature for: (a) BADCy (256 molecules), (b) BADCy (400 molecules), (c) LECy (256 molecules), (d) LECy (400 molecules), (e) SiCy-3 (256 molecules), (f) SiCy-3 (400 molecules), (g) SiMCy (256 molecules), and (h) SiMCy (400 molecules).

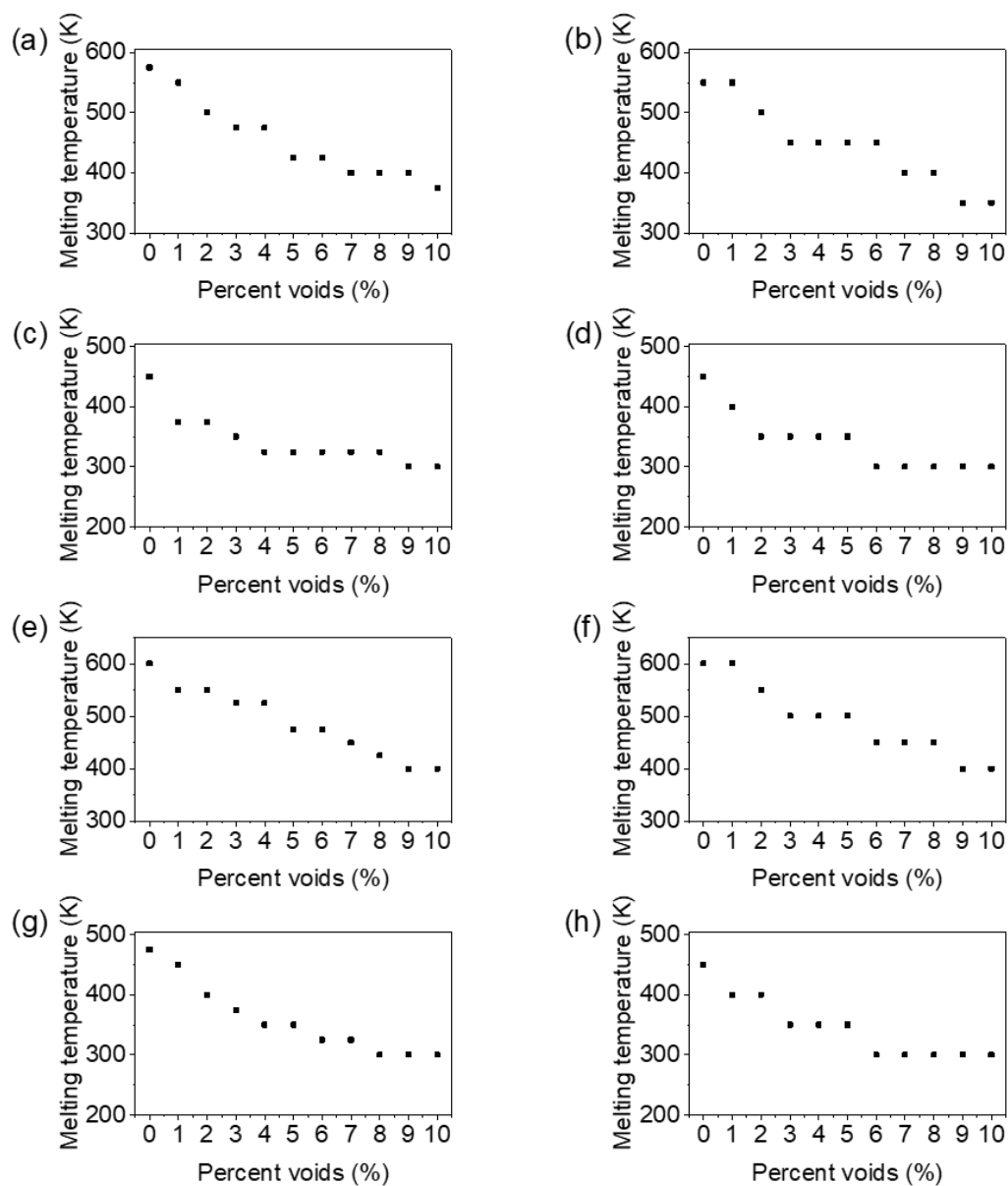


Figure 3.2 The effect of heating rate on the calculated melting temperature for: (a) BADCy (50 K/20 ns), (b) BADCy (25 K/20 ns), (c) LECy (50 K/20 ns), (d) LECy (25 K/20 ns), (e) SiCy-3 (50 K/20 ns), (f) SiCy-3 (25 K/20 ns), (g) SiMCy (50 K/20 ns), and (h) SiMCy (25 K/20 ns).

Figure 3.3 shows the evolution of volume temperature curves (50 K/20 ns, 256 mol) for systems without voids. Due to the nature of the temperature increments, the  $T_m$  was expected to be resolved within a 50 K temperature range, rather than a true

discontinuity typical for a first order phase transition. The intent was not to get an exact number, but rather a range sufficient to resolve a  $T_m$  by 50 K useful for the purpose of ranking. Figure 3.4 shows the volume-temperature curve for LECy. The volume increases linearly up to 450 K, after which an abrupt increase in volume is observed from 450 to 500 K. The  $T_m$  is assigned to the onset of this discontinuity, which is evidence of the melting of a crystalline solid.<sup>80</sup> The volume-temperature graphs for BADCy and SiCy-3 do not exhibit a discontinuous  $T_m$ . The discontinuous  $T_m$  is likely not captured in our temperature range, so 600 K is taken as the calculated  $T_m$ . For all systems with 0% voids, the predicted phase  $T_m$ 's are significantly greater than the experimental values. This finding is in good agreement with earlier observations of superheating for perfect crystalline lattices.<sup>30,90,91</sup>

The overestimation in calculated  $T_m$  for simulations without voids is largely on account that homogenous nucleation is the sole mechanism to initiate melting, which is determined by the probability of spontaneously forming liquid-like droplets in the solid phase.<sup>30</sup> Another important consideration is that melting is a fundamentally a kinetic phenomenon and varying the heating rate is known to affect the observed  $T_m$ .<sup>92</sup> Heating rates achieved in MD simulations are intrinsically much faster than heating rates accessible for experimental systems. In this context, significant superheating may occur since molecular motions are hindered below the  $T_m$  at short timescales accessible in MD simulations.

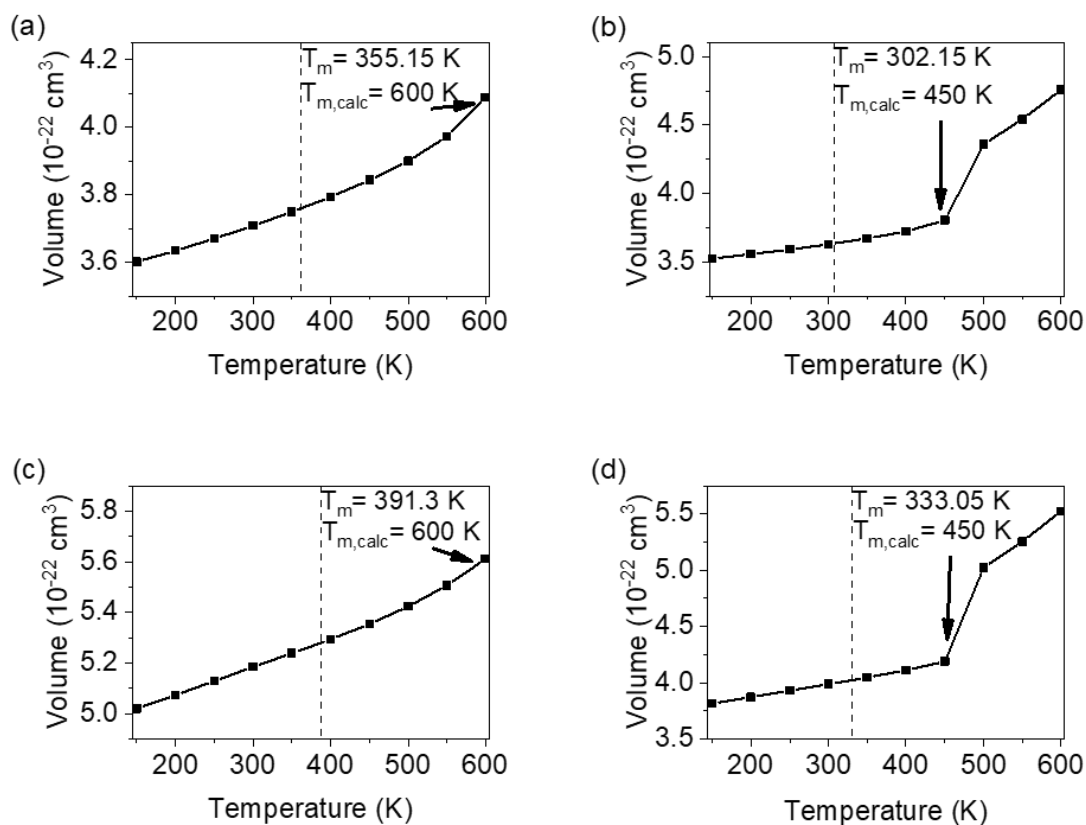


Figure 3.3 The volume as a function of temperature for monomers: (a) BADCy, (b) LECy, (c) SiCy-3, and (d) SiMCy with 0% voids. The calculated melting temperature ( $T_{m,calc}$ ) is represented by the discontinuity or inflection (arrow). The results are compared to previously reported experimental melting temperatures (dotted line).

### 3.2.2 Dependence of Monomer Melting Temperature on Percentage of Voids

The following part of this study involved removal of 1 to 10% of molecules from simulation cells. This was to assess the effect of void percent on the quality of the  $T_m$  calculation with regard to experimental values, and to observe the monomer melt behavior on an atomistic scale. The evolution of volume as a function of stepwise heating for monomers is shown in Figure 3.4. The variation of the calculated  $T_m$  as a function of percentage of total number of molecules removed from simulation cells is shown in Figure 3.5. The most striking and immediate observation for the plots is the decrease in

the predicted  $T_m$  with an increase in percent voids, complementing previous studies.<sup>28,37</sup>

The lower  $T_m$  reflects the decrease in the free energy barrier to the formation of a solid-liquid interface to nucleate melting. In general, monomers LECy and SiMCy have the lowest  $T_m$ 's, BADCy an intermediate value, whereas SiCy-3 has the highest  $T_m$ .

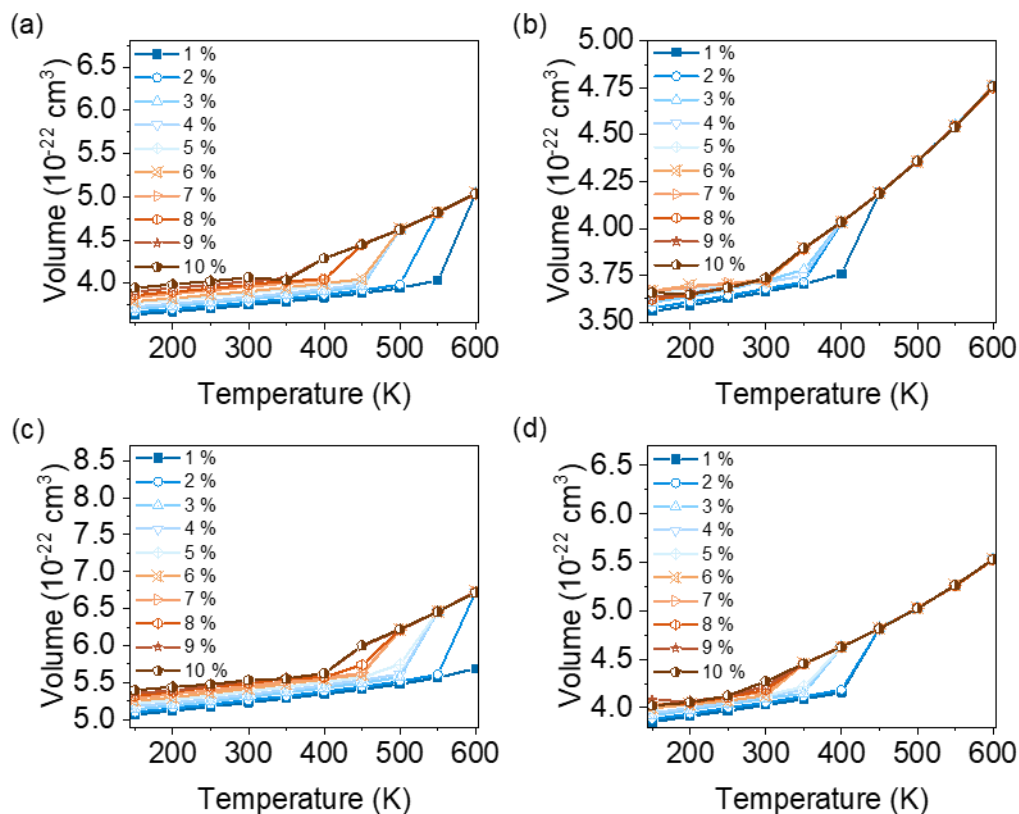


Figure 3.4 The evolution of volume as a function of temperature starting at  $T = 150 \text{ K}$  for (a) BADCy, (b) LECy, (c) SiCy-3, and (d) SiMCy with 1 to 10% voids.

While the voids were confirmed to be necessary to nucleate melting of the simulated thermosetting monomers, there were some issues with the application of the void method to these polyatomic monomers. In the traditional void method the estimated  $T_m$  has been shown to reach a constant value that is independent of the percent voids. This was not observed in all thermosetting monomers simulated, therefore an important consideration is the discrepancy from the traditional voids method, with regard to the

absence of a flat region. It is evident that LECy and SiMCy are in best agreement with the conventional void method as they reach an appreciable plateau from 6 to 10% voids. In the case of BPACy and SiCy-3, the systems do reach a narrow plateau where  $T_m$  is independent of percent voids, however it spans from 9 to 10% and is more narrow than expected. It is worth noting that the plateau value for Alvares et al., who used the voids method to study CaO, was inferred from void percentages between 9 and 27%.<sup>93</sup> For Alavi et al. the plateau spanned from 5 to 10% voids, despite the similar approach.<sup>36</sup> These findings emphasize the difficulty in predicting, *a priori*, (and calculating computationally) the  $T_m$  of monomers. A challenge that becomes formidable when targeting additional constraints on reactivity and performance to satisfy composite applications.

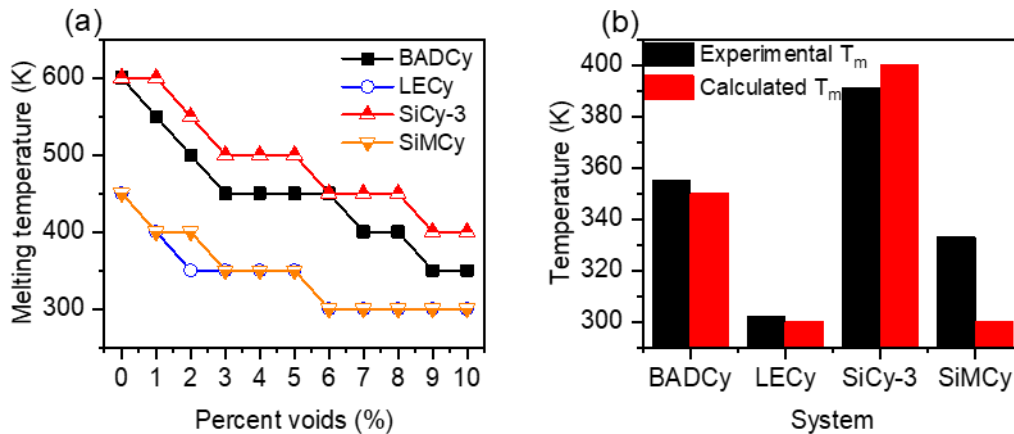


Figure 3.5 (a) The calculated melting temperature as a function of percentage voids (in % of the total monomers removed from simulation cell) and (b) calculated  $T_m$  at 9% voids compared to experimental  $T_m$ .

Figure 3.6 compared the accuracy of calculated  $T_m$ 's against the experimental values, as a function of the percentage of voids. Most of the calculated values are well above the experimental  $T_m$  partly due to the lack of heterogeneous nucleation and also

due to the measurement technique (heating rate). Of note is the good agreement of calculated  $T_m$ 's with experimental values from 9 to 10% voids for most monomer systems. Since our simulations were run in 50 K steps, we expected the technique would be capable to rank modelled systems, rather than precise numeric agreement.

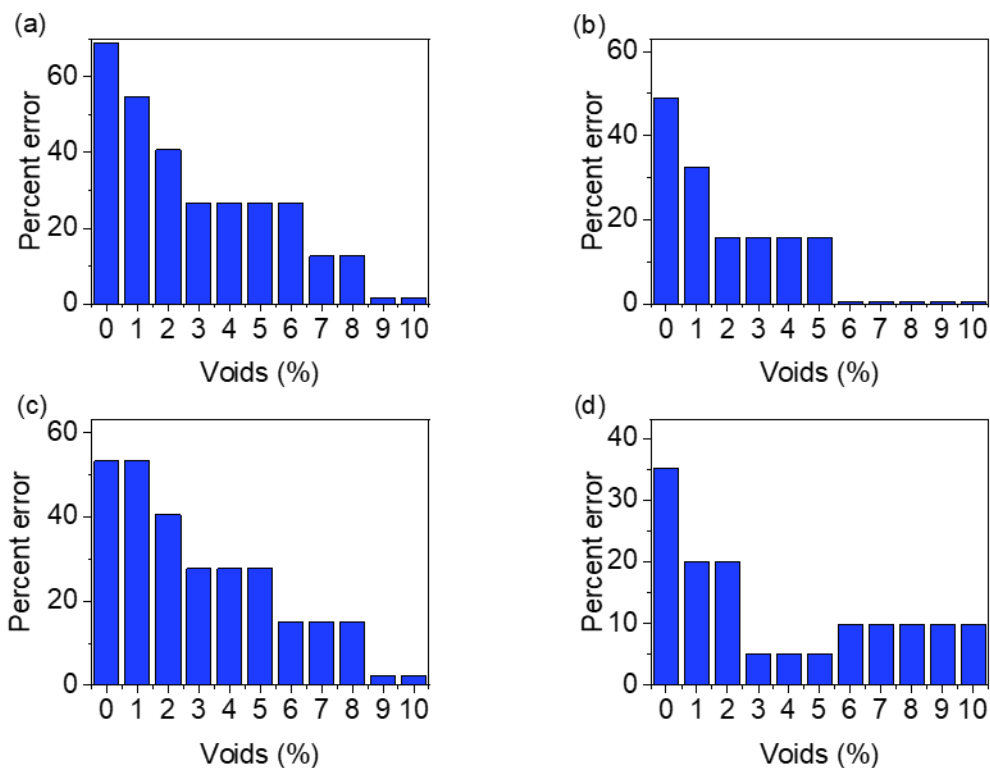


Figure 3.6 *Percent error of the calculated melting temperature, compared to the experimental values, for simulations with 0 to 10% voids (in % of the total monomers removed from simulation cell) for: (a) BADCy, (b) LECy, (c) SiCy-3, and (d) SiMCy.*

With this consideration, the 9% void systems were established for the comparison analysis between simulated monomer systems, and summarized in Table 3.1, and Figure 3.5. A point to note from this figure is that the  $T_m$  of SiMCy was most similar to the experimental value from 3 to 5% voids but the accuracy diminishes further with increasing percentage of voids. This behavior has been observed elsewhere, and related to

the mechanical instability and collapse of the simulated crystalline solid into an amorphous solid.<sup>37</sup> While this was unexpected when considering results from other monomers, when the volume versus temperature curves for SiMCy are plotted (Figure 3.7), important differences between simulated behavior became evident. It can be seen that simulations of SiMCy with 9% and 10% voids exhibited an inflection, which suggests a glass transition to a rubbery regime. The appearance of the  $T_g$  suggests the incorporation of high void percentages may cause the collapse of the solid lattice into an amorphous solid at the start of the MD simulation because the system was unable to maintain solid configuration.<sup>94</sup> It should be mentioned for the simulated systems with 256 molecules, the voids are located relatively close to each other. In the instance of high percent voids, these interfaces may overlap, transforming the solid-liquid phase into supercooling amorphous liquid. Considering the effect of size, it can be seen for the system with 400 molecules, all the simulations exhibited a discontinuous solid to liquid melting phase transition (Figure 3.7). Comparing across the four monomers at 9% void, it can be seen that the correct rank ordering is retained.

Table 3.1 *The melting points of cyanate ester monomers with 9% voids compared to previously reported literature values*

<b>Monomer</b>	<b>Calculated <math>T_m</math> (K)</b>	<b>Experimental <math>T_m</math> (K)</b>	<b>Reference</b>	<b>Percent error (%)</b>
BADCy	350	355.15	<sup>75</sup>	2
LECy	300	302.15	<sup>51</sup>	1
SiCy-3	400	391.3	<sup>22</sup>	3
SiMCy	300	333.05	<sup>76</sup>	10



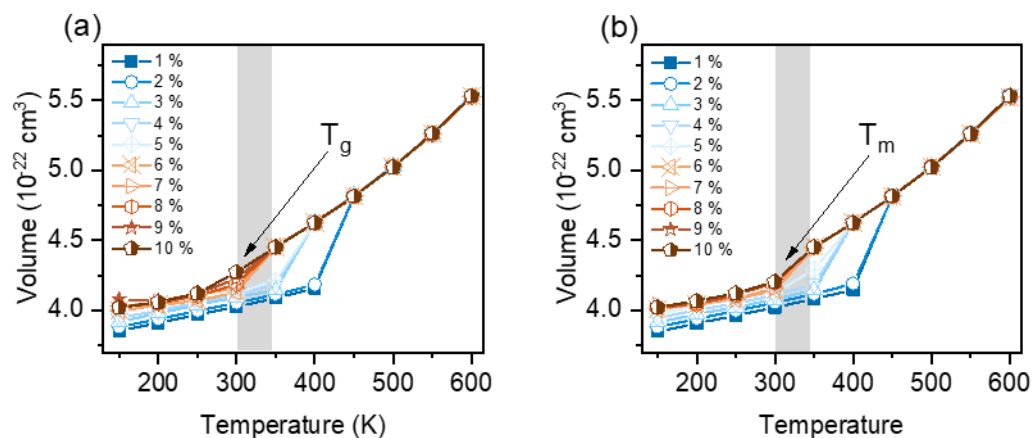


Figure 3.7 The evolution of volume as a function of temperature for SiMCy with: (a) 256 and (b) 400 molecules.

### 3.2.3 Structural Characterization

Following the examination and validation of system construction with  $T_m$  calculations, the structural parameters were also explored. Order parameter studies were performed to determine the possible correlation of local short-ranged ordering to  $T_m$  and observe monomer melt behavior on the molecular level. The Order Parameter in MS suite was utilized and applied to monomer systems with 9% voids. The calculations involved the use of simulation cells slightly below ( $T_m - 50 \text{ K}$ ) and above ( $T_m + 50 \text{ K}$ ) the  $T_m$ . The low and high temperature order parameters for each class of monomer is summarized in Table 3.2, and snapshots of this order to disorder transition is shown in Figure 3.8. The simulated values were expected to be maximum for monomers with high  $T_m$ 's, and minimum for monomers with comparatively lower  $T_m$ 's.

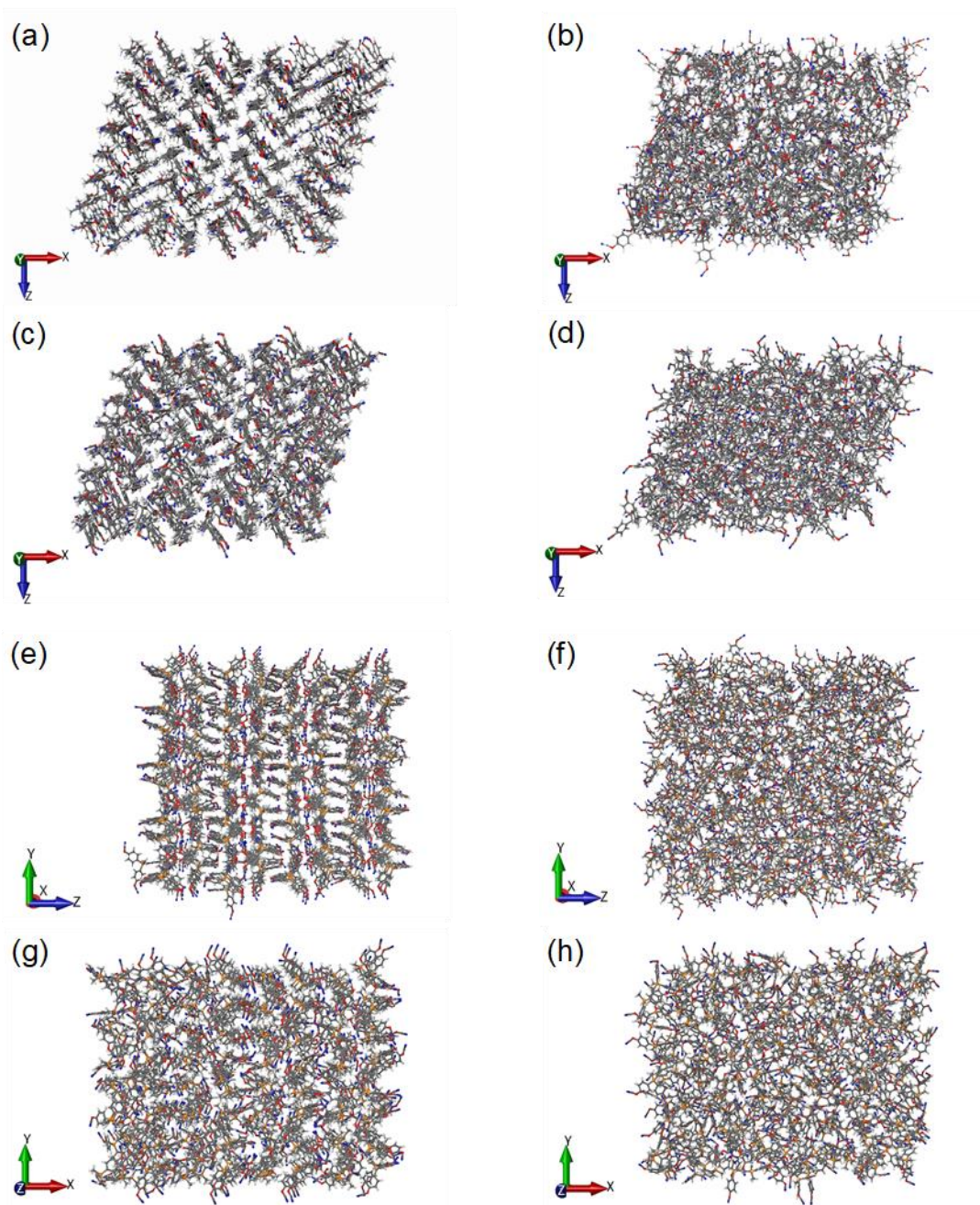


Figure 3.8 Snapshots of the monomers at different stages of the melting process with 9% voids for the following monomers: (a) BADCy (300 K), (b) BADCy (450 K), (c) LECy (250 K), (d) LECy (400 K), (e) SiCy-3 (350 K), (f) SiCy-3 (500 K), (g) SiMCy (250 K), and (h) SiMCy (400 K).

Table 3.2 *The orientational order parameter values for monomers: 50 K below the calculated melting temperature and 50 K above the calculated melting temperature*

<b>Monomer</b>	<b>Order parameter below <math>T_m</math></b>	<b>Order parameter above <math>T_m</math></b>
BADCy	0.515 (300 K)	0.09 (450 K)
LECy	0.41 (250 K)	0.06 (400 K)
SiCy-3	0.61 (350 K)	0.06 (500 K)
SiMCy	0.24 (300 K)	0.03 (450 K)

The orientational order parameters for the monomers below the  $T_m$  vary from ~0.6 to ~0.3, and are ranked from highest to lowest in the following order: SiCy-3 > BADCy > LECy > SiMCy. SiCy-3 has the highest order parameter and the highest experimental  $T_m$  of the monomers characterized in this study. Analysis shows a comparable ordering between BADCy and LECy systems, with BADCy being slightly higher. It is well known that the BPA-derived cyanate ester monomer with 2 methyl groups on the bridgehead tend to have increased rigidity. Compared to BADCy, LECy has one less methyl group on the bridgehead group, resulting in an increase in flexibility, and decrease in close contact ordering (Figure 3.9). The correlation between order parameter and  $T_m$  seen here lends support to the hypothesis that increase ordering between close contacts is the driving factor to the melting temperatures.

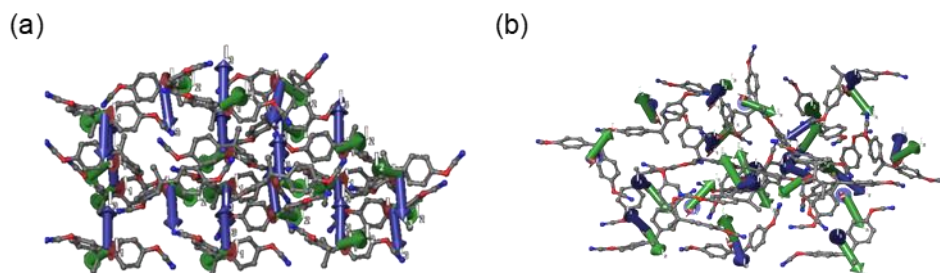


Figure 3.9 Snapshots of (a) BADCy and (b) LECy, highlighting the ordering of close contacts. The principal moments of inertia are displayed as a set of orthogonal tubes.

However, it was surprising the same trend does not hold with SiMCy, as it has the lowest order parameter, yet the second lowest  $T_m$ . This result may be rationalized by the monomer chemical structure, that the increased flexibility from the silicon substituted bridgehead increases isotropy in the ordering, resulting in the lowest order parameter value. Work by Guenther et al. has shown that the rotational barriers experienced by the silicon containing monomer is low compared to BADCy (quaternary carbon) due to “extra” conformational freedom of SiMCy, due to the quaternary silicon group.<sup>22</sup> For SiMCy, the two phenyl rings are not “locked in” and can occupy a variety of twist angles, which may rationalize the low order parameter. It should also be mentioned that the low order parameter value signifies the presence of amorphous domains in SiMCy simulation cell, which is in agreement with observation of a  $T_g$  for SiMCy systems with 9 to 10% voids. When considering the previous section where the calculated  $T_m$  value (9% voids) was compared to the experimental  $T_m$  value, the presence of amorphous domains, rather than the crystal structure, may cause result in lack of congruous trends formerly observed with molecular simulations using voids method (underpredicted  $T_m$ ).

For simulations run above  $T_m$  all monomers exhibited observable drops in order parameter that approached zero over time, which was expected. As seen in Figure 3.10, BADCy was observed to reach an equilibrium value of 0.09, indicating the crystalline lattice structure completely dematerializes.<sup>95</sup> Similar trends were observed for the other monomers. These observations indicate an order-to-disorder transition as a result of the melting process, specifically an increase in mobility and decrease in associations.<sup>96,97</sup>

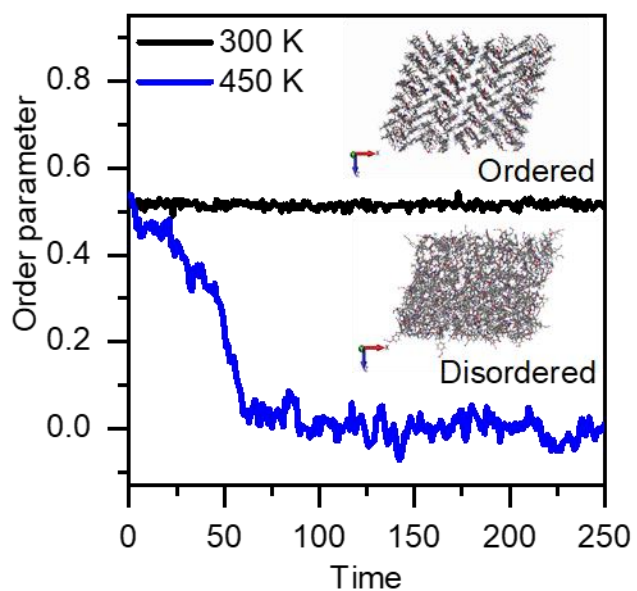


Figure 3.10 *The orientational order parameter for BADCy 50 K below the calculated melting temperature (black line) and 50 K above the calculated melting temperature (blue line). Included is a snapshot of monomers in the ordered state below the calculated melting temperature and disordered state above the calculated melting temperature.*

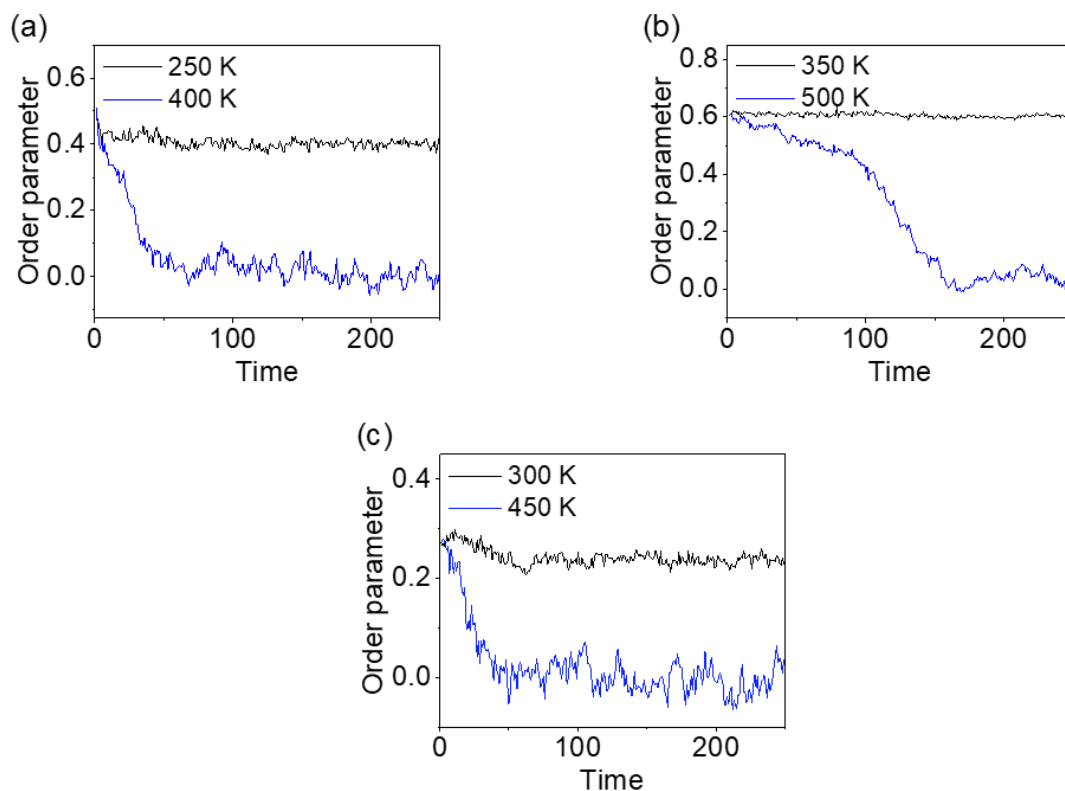


Figure 3.11 *The orientational order parameter for monomers: (a) LECy, (b) SiCy-3, and (c) SiMCy 50 K below the calculated melting temperature (black line) and 50 K above the calculated melting temperature (blue line).*

To further investigate structure-property relationships and examine possible correlations between chemical structure (freedom of motion) and monomer  $T_m$ , Torsion Profile Analysis was performed on monomer systems. The module allows for the investigation of a property that is not readily accessible experimentally: phenyl ring torsion of monomer melts. It was hypothesized that the difference in  $T_m$  between monomers was influenced by the chemical structure and assumed flexibility of the bridgehead group.<sup>22</sup> Furthermore, phenylene flips would indicate the solid to liquid phase transition, with high melting monomers having a narrow distribution of dihedral angles, indicating high rigidity. Conversely, it was expected that low melting monomers would have broader distributions of dihedral angles, indicating increased monomer flexibility.

In order to examine this, equilibrated systems slightly below ( $T_m - 50$  K) and above ( $T_m + 50$  K) the  $T_m$  were examined. For most systems 9% voids was used. For SiMCy 7% voids was used, since the system maintained crystalline structure prior to melting, as evidenced by a first order solid to liquid phase transition. Figure 3.12 shows examples of changes in the dihedral distribution (phenyl group orientation compared to methyl bridging group) upon the solid-liquid phase transitions. In the case of BADCy, below the  $T_m$  the mean values fluctuate around  $-174$  to  $-154^\circ$ ,  $-124^\circ$ ,  $-94$  to  $-84^\circ$ ,  $-54^\circ$ ,  $-30$  to  $25^\circ$ ,  $55^\circ$ ,  $85$  to  $95^\circ$ ,  $125^\circ$ , and  $155$  to  $175^\circ$ . The peak positions of the BADCy dihedral angle shift as the temperature is increased from 300 to 450 K. The pronounced peaks in the distributions merge and range from  $-175$  to  $-125^\circ$ ,  $-95$  to  $55^\circ$ , and  $95$  to  $175^\circ$ . Not only do the peak widths in the distribution increase, but the peak heights also decrease upon melting, signifying a decrease in barrier to motion as the relative populations of conformers broadened.<sup>98</sup> The torsion of phenyl rings with respect to the two methyl groups at the bridge are able to assume a broad range of conformations, and ring acquires more freedom to rotate. A similar trend is seen with LECy. Below the  $T_m$ , the torsion has maxima at  $-153$  to  $-143^\circ$ ,  $-113$  to  $-64^\circ$ ,  $-34$  to  $-24^\circ$ ,  $15$  to  $35^\circ$ ,  $65$  to  $75^\circ$ ,  $94^\circ$ ,  $114^\circ$ , and  $144$  to  $154^\circ$ . Above the  $T_m$  the probability has greatly changed, and the maxima occur from  $142$  to  $-123^\circ$ ,  $-63$  to  $-24^\circ$ ,  $26$  to  $56^\circ$ , and  $105$  to  $145^\circ$ . Compared to BADCy, it can be seen that LECy has more broad peaks below the  $T_m$ . This broadening indicates a lower barrier to motion for LECy, compared to BADCy, which would be expected on the basis of the decrease in rotational steric hinderance upon replacing one methyl bridging group with a Hydrogen atom. Ultimately, the lower barrier to motion results in concomitant decrease in  $T_m$ , and the expectedly lower order parameter seen for LECy in the previous

section. However, when considering the distribution of dihedral angles for all of the monomers in the data set, important differences between monomer freedom of motion become apparent. Figure 3.12 shows the broadest peaks in the melt (above the  $T_m$ ) are in the order of: BADCy > SiMCy > SiCy-3 > LECy. However, the  $T_m$  values occurs in the following order: SiCy-3 > BADCy > SiMCy > LECy. While the computed results appear contradictory to previously reported experimental value, this suggests that the barrier to motion (internal entropy) is not the sole contributor to the  $T_m$ , and other factors should be considered, such as interactions with neighboring molecules (intermolecular interactions). These results align with those of Ghiassi et al. who used X-ray crystallography, thermal, and computational simulations to study the structure-property relationships that determine the melting characteristics for a series of cyanate ester monomers. The authors similarly concluded the expected correlation between restricted motion and entropy of melting (melting characteristics) was not observed for the examined monomers.<sup>24</sup>

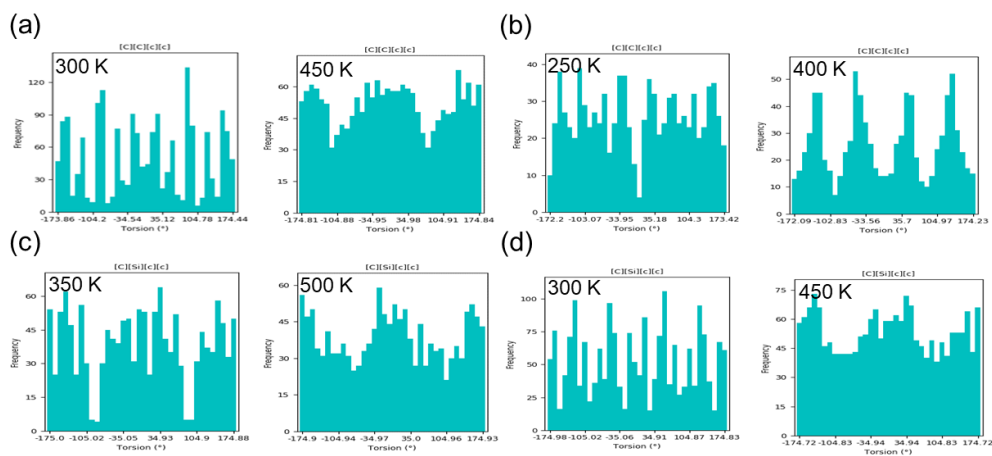


Figure 3.12 Histogram plots to examine the distribution angle values for an individual torsion for: (a) BADCy, (b) LECy, (c) SiCy-3, and (d) SiMCy.



The dihedrals between aromatic rings and a bridging methyl group are of particular interest because they define the phenyl ring positions in the molecule. In order to explore this further, dihedral angle is plotted as a function of time during equilibration, for BADCy (Figure 3.13).

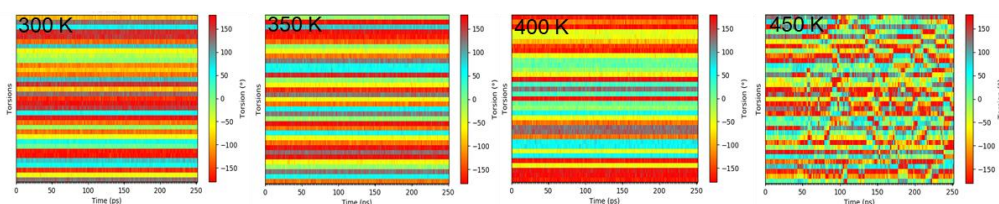


Figure 3.13 *Display of angles for each individual torsion as a bar plot over the simulation time range with colors denoting the size of the angle for BADCy.*

The sequence of images shows the time-dependent distributions of dihedral angles that demonstrate the phase transition of BADCy monomers upon heating above the  $T_m$ . In the crystal state the torsion angles were relatively stagnant and distributed without deviation along a gradient, as expected. At 450 K a fluctuation in dihedral angle of phenyl group orientation compared to methyl bridging group suggests ring flips occur, likely due to the increase in thermal energy when the melting temperature is approached. The same trend can be seen for all systems (Figure 3.14), which show fluctuating dihedral angles upon melting, in accordance with the increase in thermal energy and freedom of motion.

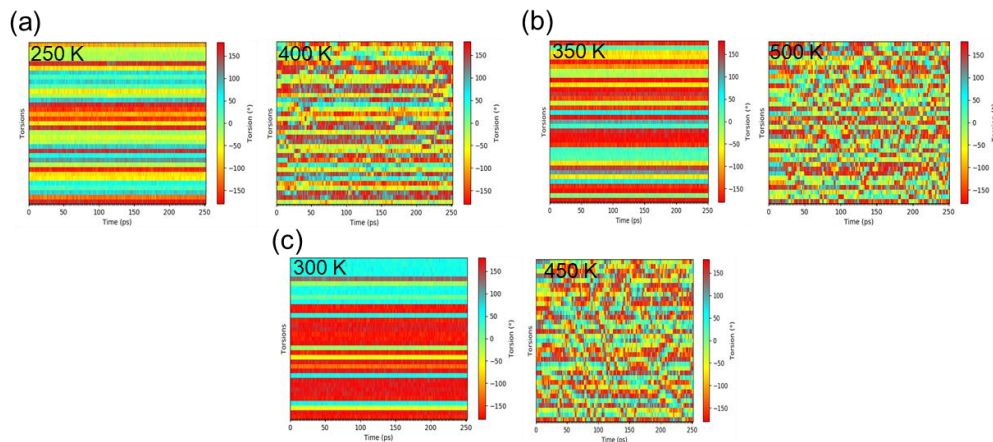


Figure 3.14 *Display of angles for each individual torsion as a bar plot over the simulation time range with colors denoting the size of the angle for: (a) LECy, (b) SiCy-3, (c) SiMCy.*

### 3.3 Conclusions

This research was aimed at studying the effect of chemical structure on the melting behavior of cyanate ester thermosetting monomers and investigating the performance of the voids method introduced by Solca et al. in capturing the melting temperature.<sup>37</sup> MD simulations were carried out on the crystalline monomers with void percentages up to 10%. A computational framework and a compared analysis of simulated  $T_m$  is presented and validated through comparison to previously reported empirical data. Additionally, the torsion and orientational order parameter were used to examine the monomers' freedom of motion in order to determine structure-property relationships. It was found that systems with 9% voids provided the best estimate of  $T_m$  for most systems. The orientational order parameter and torsion simulations gave insight on the local short-ranged ordering of monomers and monomer flexibility. The monomers with lower melting temperatures tended to have lower orientational order parameters than monomers with higher values as expected,<sup>99</sup> based on molecular symmetry and packing.

Furthermore, these results in tandem with torsion simulations indicated that the internal barrier to motion is not the sole contributor to  $T_m$ , and intermolecular interactions must also be considered. As a whole the results shed light on how chemical structure of cyanate ester monomers may affect  $T_m$  both computationally and experimentally determined, and can be utilized to inspire the development of thermosetting monomers with optimal monomer melt properties for demanding applications.

## CHAPTER IV – EFFECT OF MONOMER STRUCTURE ON THERMAL AND THERMOMECHANICAL PROPERTIES

### 4.1 Abstract

The aim of this chapter is to investigate the feasibility of synthesizing cyanate esters (CE's) from renewable plant sources and investigate the complex network architecture that are established within glassy crosslinked polycyanurate matrices. Plant-based polyphenolic scaffolds were readily converted to CE monomers, and compared to CE's of bisphenol A and bisphenol E. The polymer properties were characterized via DSC, DMA, and TGA. Profound changes in network architecture of the trifunctional bio-based CE, compared to difunctional networks, were apparent from DMA and TGA analysis. The increase in functionality and backbone rigidity produced a network with dramatically improved high temperature modulus and thermal stability. More specifically, glass transition temperatures up to 296 °C and char yields up to 70 % were observed for the polymers of cisResCy. From the appraisal of the thermomechanical properties, such  $T_g$  and decomposition temperature, it is shown that highly crosslinked bio-based polycyanurates offer advantages of superior high temperature performance and reliability, affiliated with “next generation” matrix chemistries.

### 4.2 Results and Discussion

The trifunctional bio-based cyanate ester, cisResCy, was synthesized from resveratrol. The polymerization reaction and thermal stability of the sustainable cyanate ester, along with industrial benchmarks was characterized via nonisothermal Differential Scanning Calorimetry (DSC) and Thermogravimetric Analysis (TGA). These are analytical techniques commonly employed by polymer chemists. The first technique

measured the extent of reaction as a function of cure time. The cure profile that was used is as follows: 160 °C (2h), 180 °C (2h), 200 °C (2h), 220 °C (2h). Thermal stability data was obtained with TGA to investigate the effect of functionality and molecular structure on thermal stability.

#### 4.2.1 Synthesis of *cisResCy* Monomer

The synthetic route to convert *trans*-resveratrol to the *cis*-resveratrol isomer, and the subsequent conversion to a cyanate ester is shown in Figure 4.1.

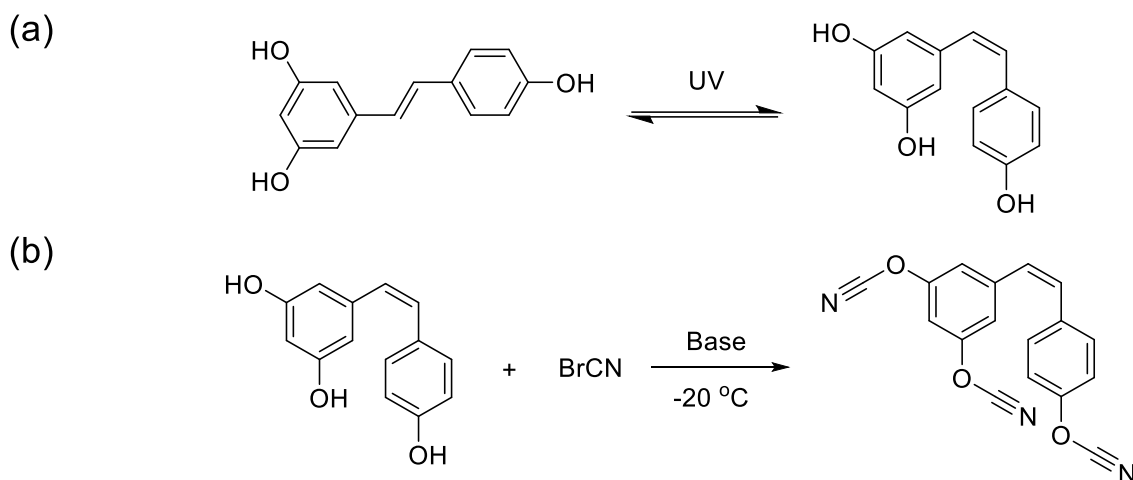


Figure 4.1 (a) Isomerization of *trans*-resveratrol to *cis*-resveratrol and (b) cyanation of *cis*-resveratrol to *cisResCy*.

The isomerization of *trans*-resveratrol to *cis*-resveratrol proceeded via irradiation on the PRSC roof using the sun as a light source. A conversion of 70 % was verified by taking an aliquot of the solution in  $\text{CdCl}_3\text{-d}_6$  for  $^1\text{H}$  NMR spectroscopy, by comparing the areas of the resonant shifts of the respective isomers. The *cis*-resveratrol isomer with a ~12 Hz coupling shifted upfield, compared to the *trans* isomer with a ~16 Hz coupling (Figure 4.2).

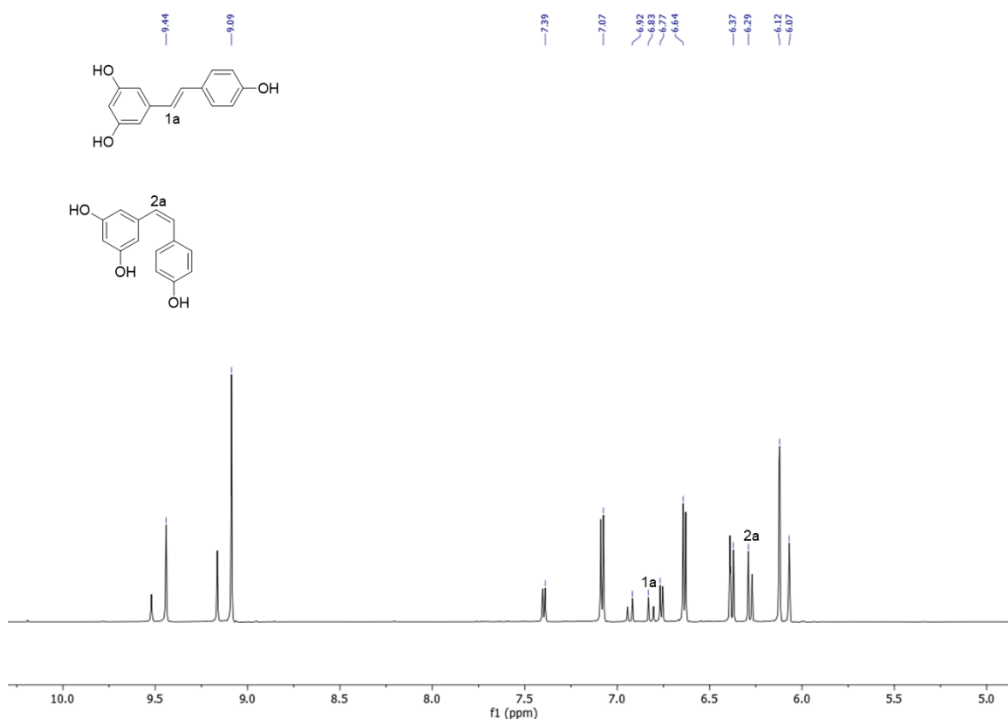


Figure 4.2  $^1\text{H}$  NMR of crude product from isomerization of trans-resveratrol to cis-resveratrol.

The characteristic alkene hydrogen atoms with of the cis isomer with a distinct 12 Hz coupling was moved upfield, compared to the trans with a representative coupling of 16 Hz. The cis-resveratrol was separated from the trans isomer using a filtration, due to the superior solubility of the *cis* isomer in diethyl ether. The pure *cis*-resveratrol product was characterized by  $^1\text{H}$  NMR, which agreed with previously reported literature values (Figure 4.3).<sup>14</sup>

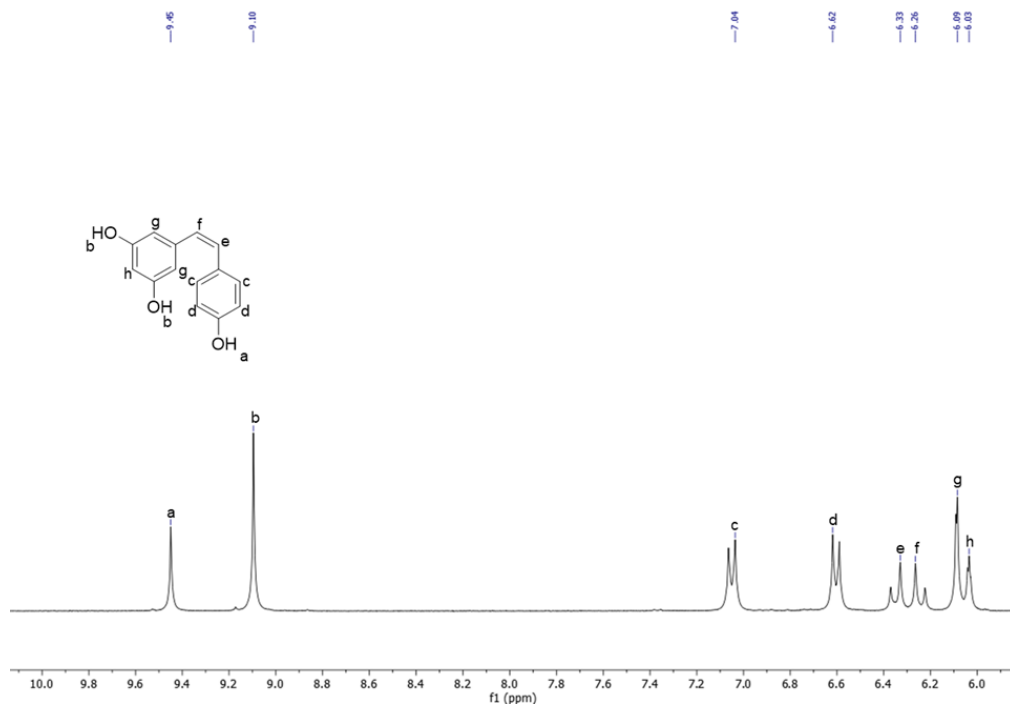


Figure 4.3  $^1\text{H}$  NMR of *cis-resveratrol*.

Despite the reversible nature of the isomerization reaction of *trans-resveratrol* to the *cis-resveratrol* isomer, it was determined that brief exposure of the *cis* isomer to fluorescent lighting did not result in a measurable backwards reaction. In addition, *cis-resveratrol* was observed to be stable when stored in ambient conditions in a dark cabinet.

In order to further investigate the reversible nature of the resveratrol isomerization, and the effect of heat on *cis-resveratrol*, DSC experiments were performed (Figure 4.4). It can be seen that the compound was stable before the melting temperature (170 °C). At temperatures above this melting transition, there is an exothermic event spanning from approximately 175 to 230 °C. Considering that *trans-resveratrol* has a reported melting temperature of approximately 260 °C, the thermogram provides evidence of thermal isomerization of *cis-resveratrol* to the *trans* diastereomer.<sup>14</sup> It is

proposed that when *cis*-resveratrol melts, it undergoes thermal isomerization to the more thermodynamically stable isomer.

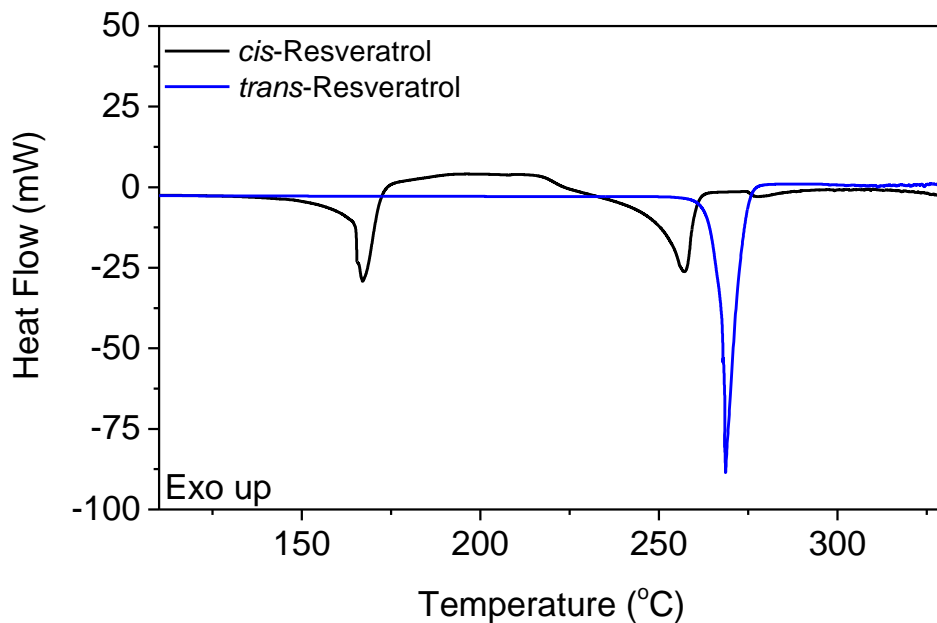


Figure 4.4 *Heat flow vs. temperature for cis-resveratrol and trans-resveratrol.*

Cyanation of *cis*-resveratrol was undertaken using the quintessential reaction with triethylamine and cyanogen bromide first published by Grigat and Putter.<sup>14</sup> After the reaction *cis*ResCy was gathered as a crystalline solid (Figure 4.5).



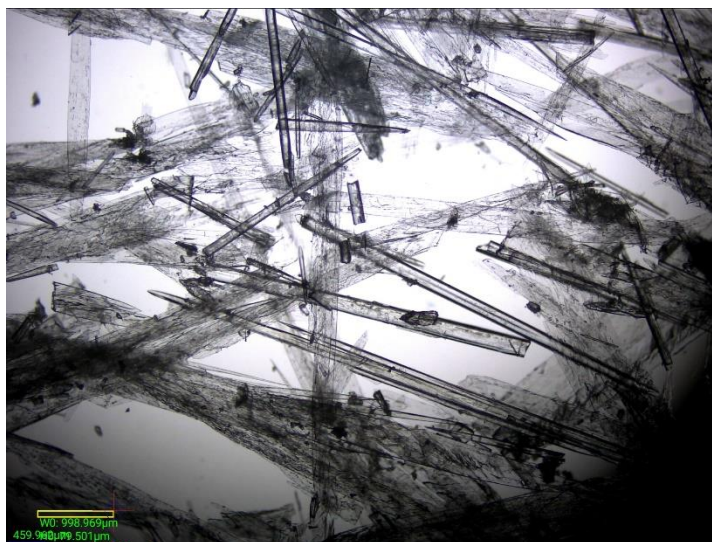


Figure 4.5 *Crystals of cisResCy.*

The CE monomer was also characterized by  $^1\text{H-NMR}$  (Figure 4.6) and FTIR (Figure 4.7). In the  $^1\text{H-NMR}$  spectrum of cisResCy in diemethyl sulfoxide- $d_6$  (Fig. 2) the signals at 6.82 ppm (d, H) and 6.94 ppm (d, H) are characteristic of the protons on the ethylene bridge connecting the atomatic rings. The signal at 7.27 ppm (s, 2H), 7.51 ppm (s, H), and 7.51 ppm (s, H) are assigned to aromatic protons on the disubstituted cyanate ester group, and the resonance at 7.41 ppm (s, 4H) is assigned to the aromatic hydrogens on the monosubstituted functional group. The chemical shifts for water and diemethyl sulfoxide- $d_6$  can also be observed at 3.31 ppm and 2.52 ppm respectively.

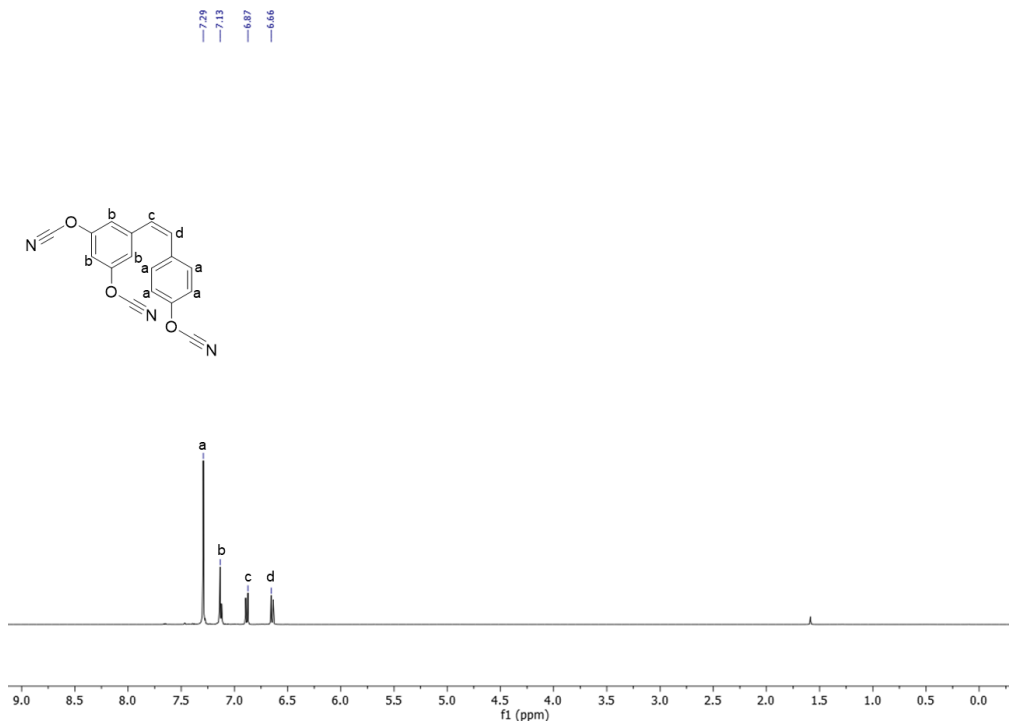


Figure 4.6  $^1\text{H}$  NMR of *cisResCy*.

FTIR analysis confirmed the product by the disappearance of the characteristic phenol of the starting material, and the appearance of a  $\text{C}\equiv\text{N}$  absorbance at  $2250\text{ cm}^{-1}$  (Figure 4.7).

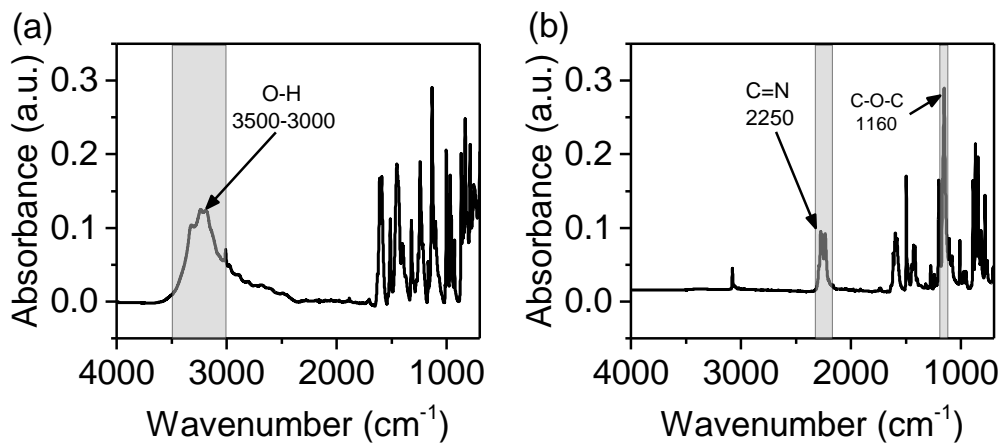


Figure 4.7 IR spectra of: (a) *cis-resveratrol* and (b) *cisResCy*.

Figure 4.8 and Figure 4.9 show the  $^1\text{H}$  NMR of two commercially available cyanate ester monomers, 2'-(4-cyanatophenyl)propane (BPACy) and 4,4'-(ethane-1,1-diyl)bis(cyanatobenzene) (LECy), respectively. Both monomers are dicyanates derived from bisphenols, but differ in the nature of the bridging group. For example, BPACy features a rigid dimethyl segment, whereas LECy has a more flexible methyl linking group.

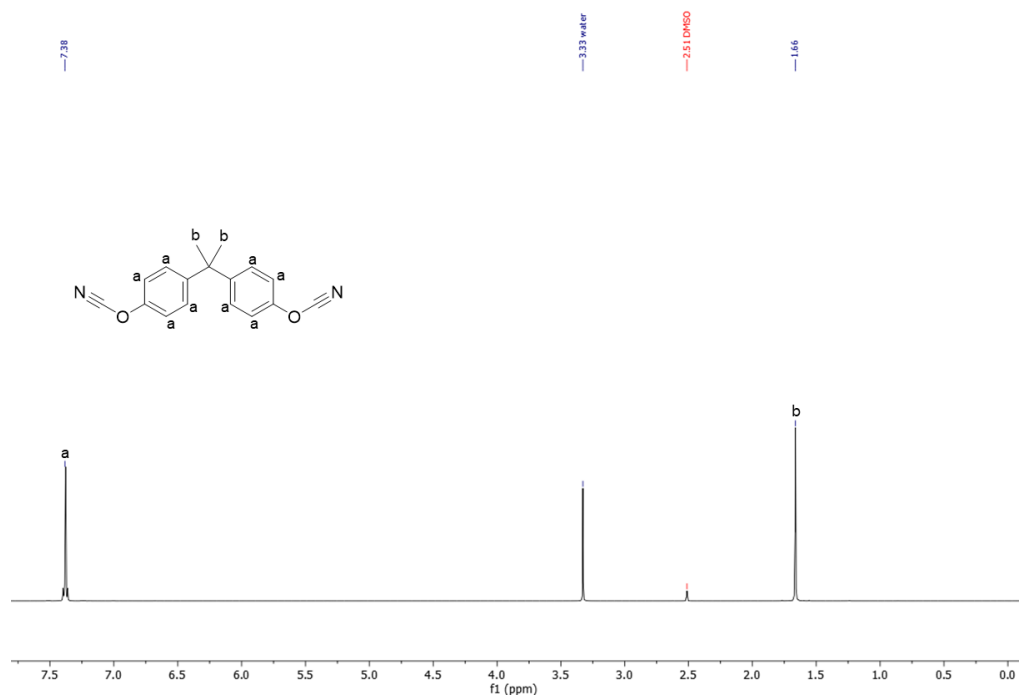


Figure 4.8  $^1\text{H}$  NMR of BPACy.

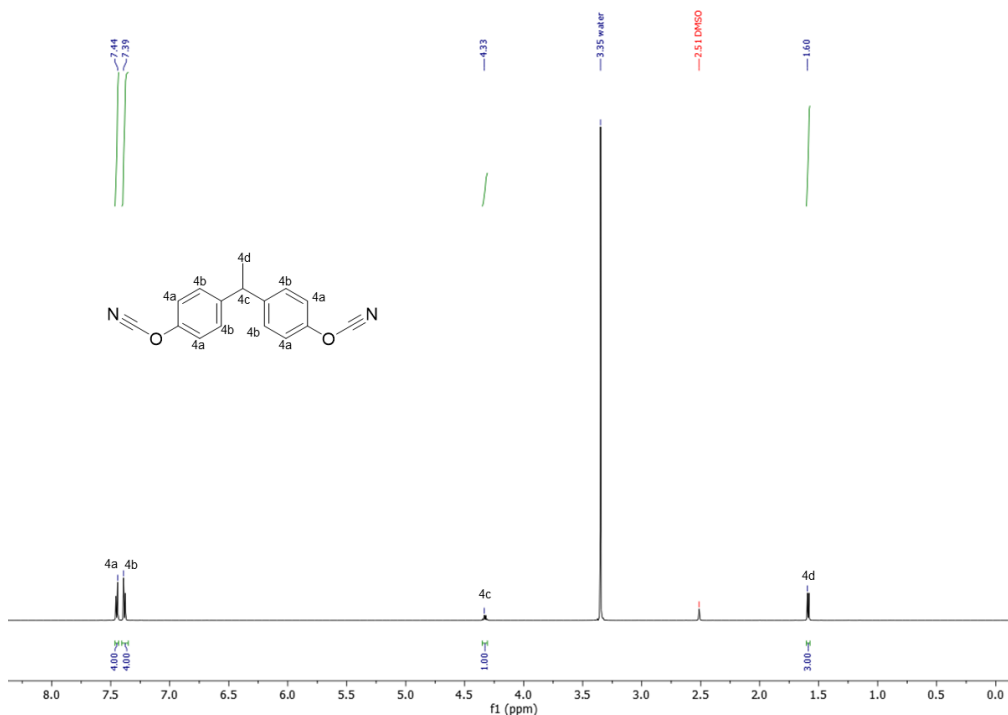


Figure 4.9  $^1\text{H}$  NMR of LECy.

#### 4.2.2 DSC

The pure monomers were analyzed by DSC to study processability and cure chemistry. The DSC thermograms for cisResCy, BPACy, and LECy are shown in Figure 4.10. All of the monomers had melting temperatures below 100 °C. More specifically, the DSC thermogram shows endothermic transitions associated with  $T_m$  at 82 °C and 81 °C for cisResCy and BPACy, respectively. The sharp melting endotherm for both compounds had a narrow range which demonstrated the high purity of the monomer. At room temperature the BPACy and cisResCy monomers were crystalline solids, whereas LECy was as a supercooled liquid, and therefore the melting temperature was not observed in the temperature range of the DSC thermogram. It has been previously shown by Guenther et al.<sup>51</sup> that the low melting temperature of LECy is a function of the crystal structure of the monomer. For example, single X-ray Diffraction studies showed

crystal disorder on account of two co-crystallized arrangements, which was accredited to the bridge connecting the aryl cyanate ester groups. Specifically, this feature allowed the co-crystallized form to function as a eutectic, and stabilized the supercooled liquid. In general, the lower melting temperature of LECy is desirable and indicated good processability for composite applications.

Table 4.1 *DSC data for monomers*

<b>Monomer</b>	<b>T<sub>m</sub> (°C)</b>	<b>T<sub>o</sub> (°C)</b>	<b>T<sub>p</sub> (°C)</b>	<b>ΔH (J/g)</b>
cisResCy	82	207	287	518
BPACy	81	309	217	604
LECy	-	256	213	678

An important difference between the systems is the shape of the DSC curve, which showed a small exotherm that peaks at approximately 207 °C, followed by a larger exotherm that peaks at approximately 287 °C. This polymerization behavior had been reported for cisResCy in the literature by Garrison et al.<sup>14</sup>, and in a like manner observed two overlapping peaks, which were assigned to the isomerization of cisResCy to the *trans*-isomer, followed by the cyclotrimerization polymerization reaction.<sup>14,59</sup>

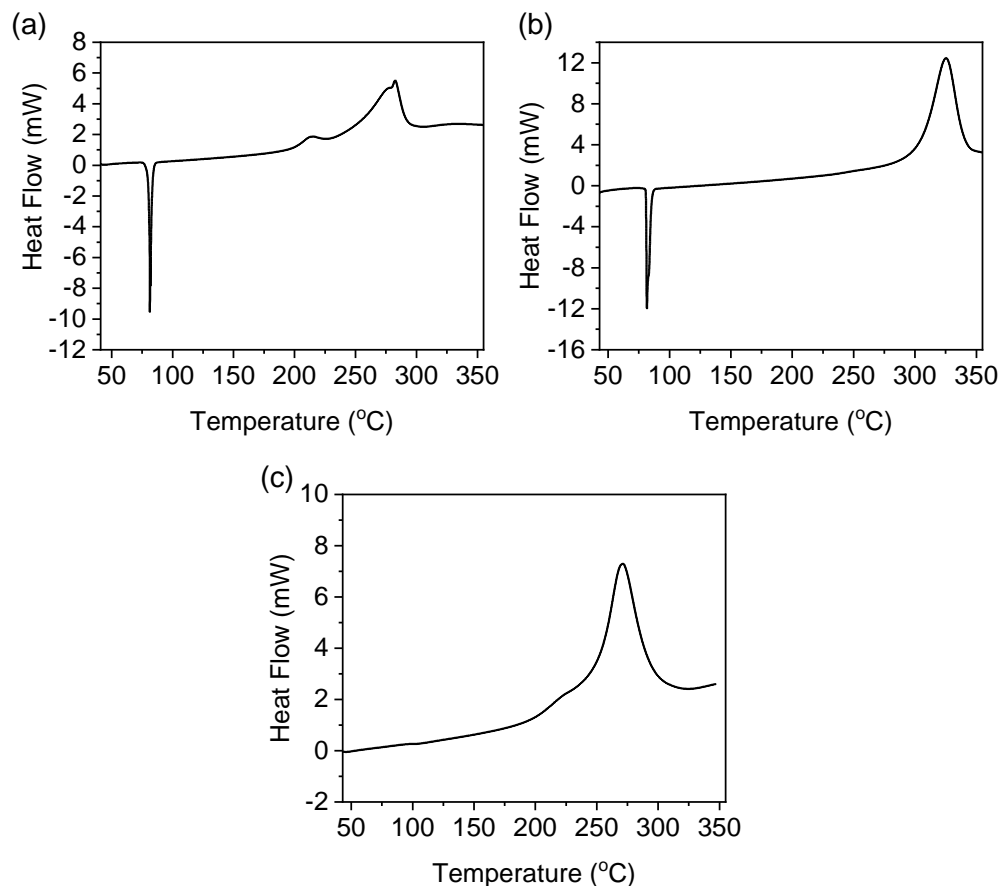


Figure 4.10 Heat flow vs. temperature for cyanate ester monomers: (a) *cisResCy*, (b) *BPACy*, and (c) *LECy*.

All monomers exhibited differences in polymerization behavior, with the onset of polymerizations ranked in the following order: *cisResCy* < *LECy* < *BPACy*. With regard to the peak exotherm temperature, the systems were ranked in the following order *LECy* < *BPACy* < *cisResCy*. The enthalpy of polymerization also varied for the examined monomers, and were ranked as follows: *LECy* > *BPACy* > *cisResCy*. The lower value for *cisResCy* implies that the resin does not completely cure under scanning conditions.

With regard to the differences in polymerization behavior between the three cyanate esters, a multitude of variables must be considered such as monomer chemical structure and flexibility. Thereafter gelation, upon which the molecular weight of the

growing network is infinite, and vitrification, where the  $T_g$  of the network is greater than the cure temperature, polymer chain motions are impeded. While unreacted functional groups remain in the network, they may be unable to collide and react. With this in mind, the low enthalpy of polymerization for cisResCy is presumptively on account of topological constraints of the rigid network produced from monomers with three cyantophenyl groups attached with an ethylene linking group.

The rigid stilbene backbone makes it difficult to achieve full conversion, in particular upon vitrification, where the network architecture is conclusively “frozen” in the configuration it possessed at the onset of vitrification. Considering the comparably lower enthalpy of polymerization of cisResCy compared to BPACy and LECy, it may be sensibly concluded that the combination of a reactive modifier, such as the aforementioned difunctional monomers (or some other molecule) may be advantageous to reach higher degrees of polymerization. For example, a more flexible co-monomer is likely to adopt a larger variety of orientations that may assist the formation of cyanurate ring systems, compared to a neat cisResCy network.

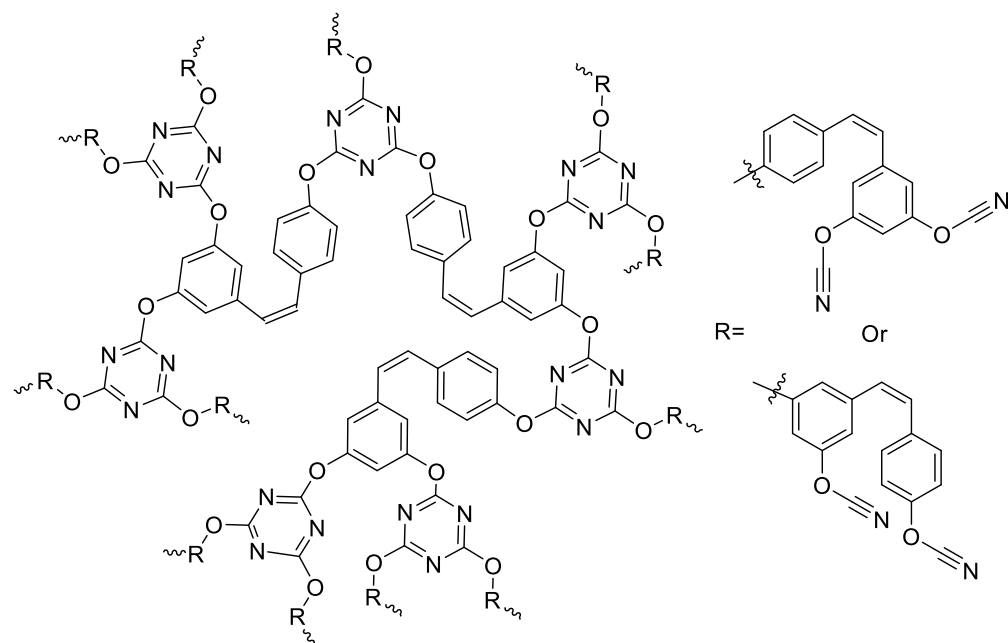


Figure 4.11 *Chemical structure of polymer network architecture from cisResCy monomer.*

It should be mentioned that impurities are known to catalyze the cyclotrimerization polymerization reaction, and we considered that slight differences in the impurity set present in the various monomer types may have had an effect on the onset of polymerization and peak polymerization temperatures. Considering the  $^1\text{H}$  NMR data for the monomers shown above, and particularly the absence of triethylammonium hydrobromide salt and amine, it was assumed the main the main impurity is the partially cyanated phenol analogue of the CE, which has been previously (and unambiguously) identified as the main impurity in other studies.<sup>76</sup> All things considered, entirely pure monomers are of limited practical significance, since they may not even polymerize.<sup>76</sup> Even so, we emphasize that the monomers in the current study involve not only differences in chemical structure, and without a doubt a humble difference in the



impurities present. As such, we have intentionally remarked on the role (if any) the difference in impurities have on the results.

Another observation to note for all of the cyanate esters, but particularly for BPACy, is the relatively higher complex viscosity from 100 to 125 °C (Table 4.2). As has been mentioned already, all monomers exhibited differences in polymerization behavior, with the onset of polymerizations ranked in the following order: cisResCy < LECy < BPACy. The viscosity of cisResCy and LECy were markedly lower than BPACy. The complex viscosity is likely to be important during the onset of polymerization, possibly explaining the higher onset of polymerization temperature of BPACy. It is proposed the more crystalline BPACy monomers are more hindered due to diffusion limitations by the relatively high viscosity. This may lower reactivity in the chemically controlled regime.

Table 4.2 Average complex viscosity of resins from 100 to 125 °C.

System	cisResCy	BPACy	LECy
<b>Complex viscosity (Pa.s)</b>	0.03 (±0.02)	10.75 (±4.30)	0.03 (±0.03)

The decrease in the complex viscosity and molecular mobility of the LECy and cisResCy monomers may enhance reactivity of monomers in the liquid state, prior to gelation. We sought to conduct a more details kinetic analysis to further support our findings. Therefore we utilized Kissinger's<sup>63</sup> and Ozawa's<sup>64</sup> methods to determine activation energy for polymerization. From the DSC curves, it can be seen as the heating rate increases, there is a shift in the reaction rates and an increase in the peak exotherm

temperature (Figure 4.12). It was also observed that the total heat of reaction increases with heating rate, due to the increase in molecular mobility and diffusion.

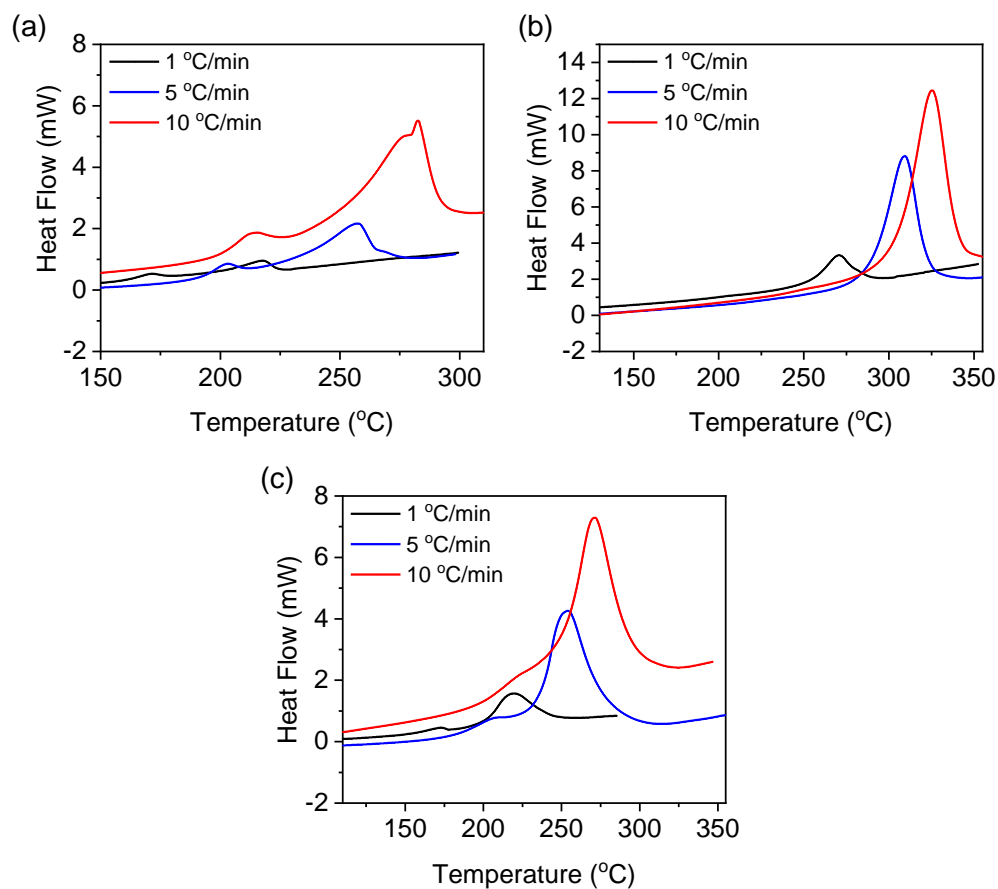


Figure 4.12 *Heat flow vs. temperature for cyanate ester monomers with heating rates of 1, 5, and 10 °C.*

Table 4.3 DSC data for monomers

Monomer	Heating Rate (°C/min)	Exotherm Max (°C)	Ea Kissinger (kJ/mol)	Ea Ozawa (kJ/mol)
cisResCy	1	217.8	69.5	74.3
	5	257.6		
	10	285.8		
BPACy	1	270.3	102.7	106.6
	5	309.3		
	10	325.2		
LECy	1	219.0	84.8	88.8
	5	254.1		
	10	274.7		

Kissinger and Ozawa plots are shown in Figure 4.13. From the straight lines in the plots, the activation energy values were calculated for cisResCy, BPACy, and LECy as follows: 69.5 kJ/mol, 84.8 kJ/mol, and 102.7 kJ/mol respectively. The lower activation energy of cisResCy suggests lower required polymerization temperatures which is desirable for composite applications due to cheaper molding materials and lower residual stress in parts.<sup>59</sup>

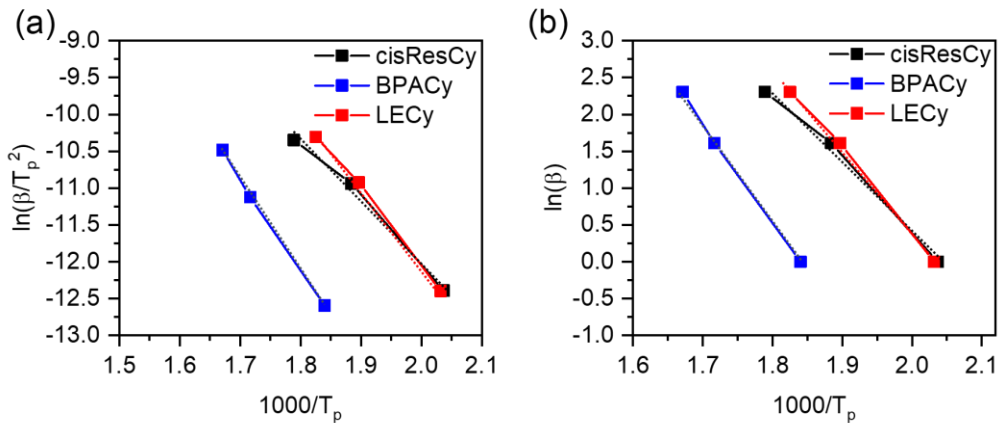


Figure 4.13 (a) Kissinger plot of  $\ln(\beta/T_p^2)$  vs.  $T$  and (b) Ozawa plot of  $\ln(\beta)$  vs.  $1/T$  for cyanate esters.

The activation energy of polymerization was ranked as followed BPCy > LECy > cisResCy. The relative increase in activation energy for the two industrial standards it hypothesized to be due to the steric hinderance of the reactive chain end groups while increasing molecular weight until gel. When comparing the industrial standards, it is hypothesized that the extra quaternary carbon of the BPACy polymer backbone contributes to higher steric hinderance than the quaternary hydrogen present in the LECy polymer backbone.

Since polymerization is accompanied by the release of heat, it is possible to evaluate the extent of conversion by relating a fraction of the total heat released in a process.<sup>100</sup> Therefore DSC was used to measure polymer conversion as a function of cure temperature, following the stepwise protocol described in the experimental section, are shown in Figure 4.14, Figure 4.15 and summarized in Table 4.4.

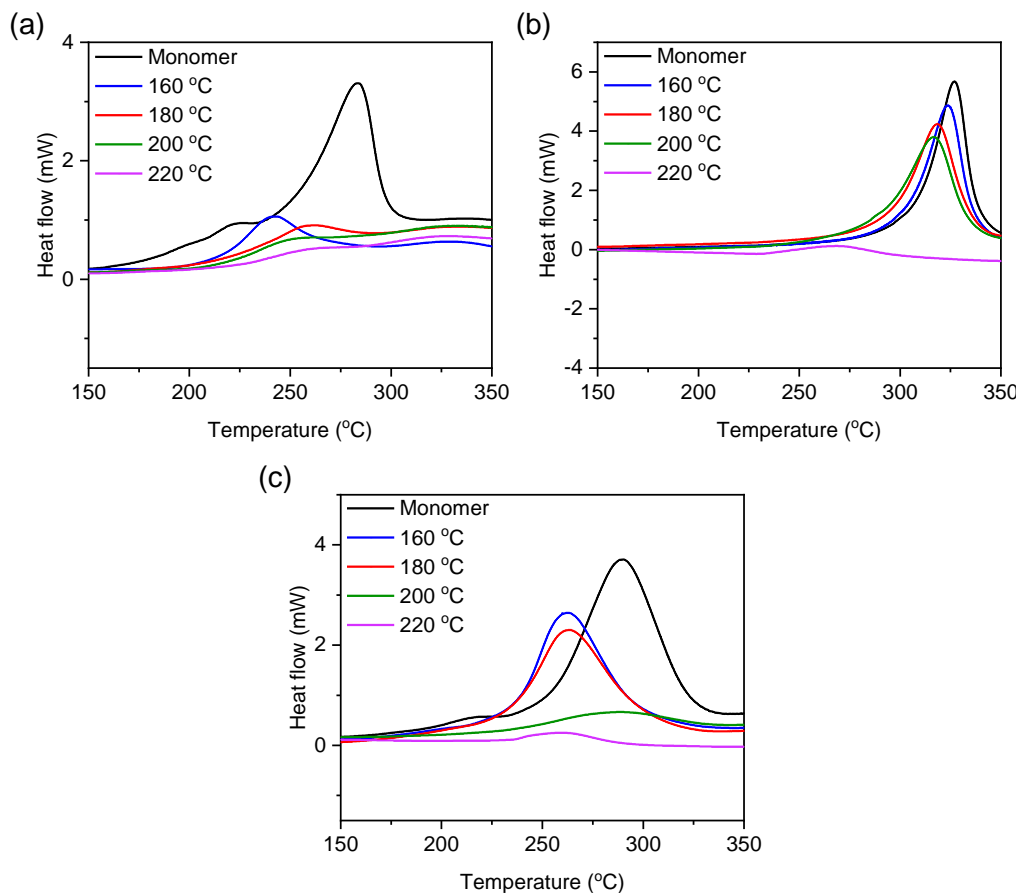


Figure 4.14 DSC plots of the residual enthalpy of polymerization for (a) *cisResCy*, (b) *BPACy*, and (c) *LECy* at each stage of the stepwise polymerization protocol.

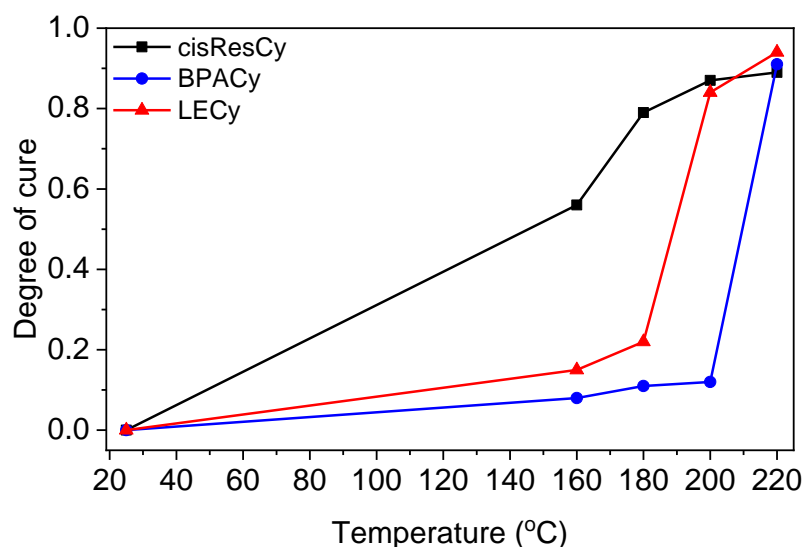


Figure 4.15 Cyanate ester conversion based on DSC measurements.

Table 4.4 The extent of cure of cisResCy, BPACy, and LECy at each stage of the stepwise polymerization protocol

Temperature (°C)	cisResCy	BPACy	LECy
160	0.56	0.08	0.15
180	0.79	0.11	0.22
200	0.87	0.12	0.84
220	0.89	0.91	0.94

It was observed that the temperature necessary to reach specific degrees of polymerization differed for each polymer. For example, to reach approximately 80 percent conversion (as measured via DSC), BPACy required a cure temperature up to 220 °C, whereas cisResCy and LECy reached a similar degree of cure at 180 °C and 200 °C, respectively. The temperatures necessary to attain a targeted degree of polymerization indicate the topological constraints for the different systems and follow the trend BPACy > LECy > cisResCy, complementing the activation energy calculations in the previous

section. Despite the resemblance of the monomer chemical structure between LECy and BPACy, the difference in the temperatures required to reach a specific degree of conversion may be rationalized when considering molecular bond flexibility. Considering the aryl cyanate ester “arms” are attached to a “core” with varying molecular bond flexibility, the LECy monomer would be anticipated to have the highest core flexibility due to the low steric hinderance around the core bonds, compared to BPACy.<sup>101</sup>

The extents of cure measured by the residual enthalpy of cure for the examined systems were ranked in the following order: LECy > BPACy > cisResCy. The lower degree of cure for cisResCy reflects the topological constraints of cisResCy, particularly given the highly crosslinked network formed from monomers with three cyantophenyl groups connected by an ethylene group. The rigidity of the stilbene backbone makes it challenging to achieve full conversion, in particular as the concentration of reactive groups are depleted.

#### **4.2.3 DMA**

The thermomechanical properties of the glassy amorphous networks were examined via DMA. The  $\tan \delta$  for the glassy amorphous networks are presented in Figure 4.16 and summarized in Table 4.5.

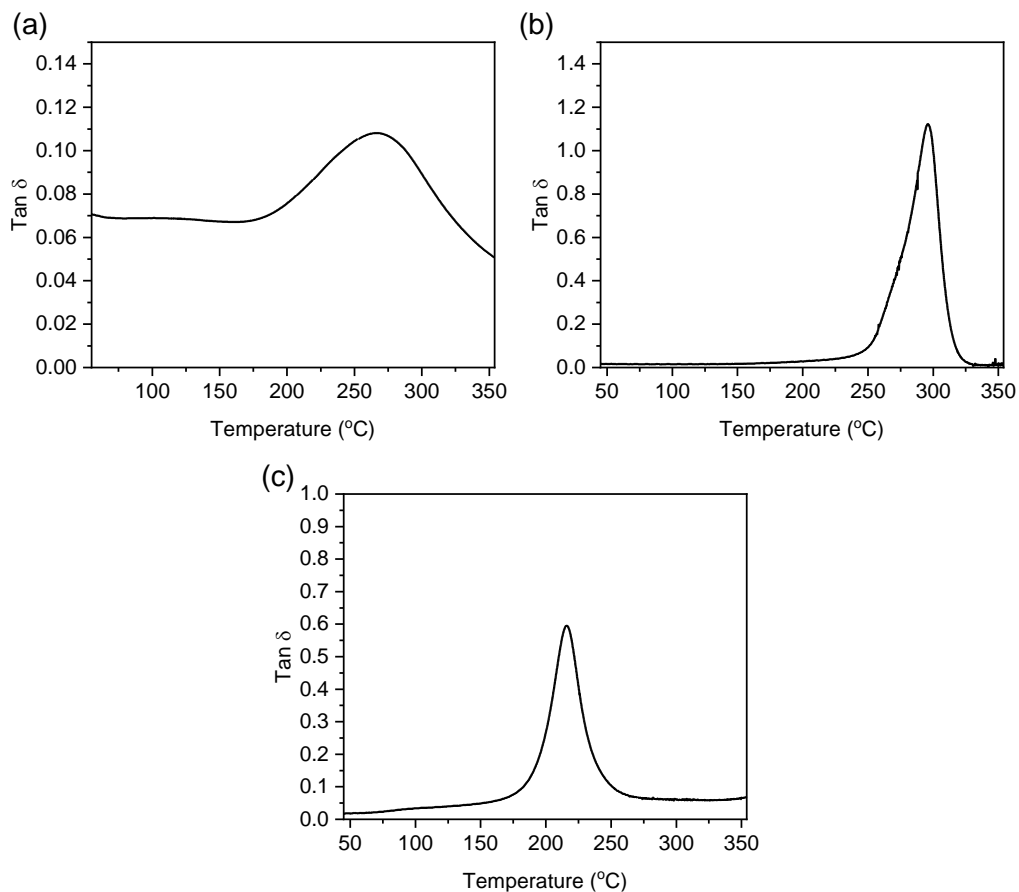


Figure 4.16  $\text{Tan } \delta$  vs. temperature for polymers of (a) *cisResCy*, (b) *BPACy*, and (c) *LECy*.

Table 4.5 *Dynamic mechanical properties for polymers with an industrial cure*

Sample	Modulus at 50 $^{\circ}\text{C}$ (MPa)	Modulus 350 $^{\circ}\text{C}$ (MPa)	$T_g$ ( $^{\circ}\text{C}$ )
<i>cisResCy</i>	4596	2756	282
<i>BPACy</i>	5756	41	296
<i>LECy</i>	5645	58	216

The dampening peak corresponding to the  $T_g$  of networks were observed at varying temperatures in the order of: *BPACy* < *cisResCy* < *LECy*. Analysis of the shape of the alpha transition can provide additional information about the structure of the



crosslinked network. For example, the height of the alpha transition ( $h_\alpha$ ) for a thermoset mixture provides information on the network, with a lower  $h_\alpha$  as the distance between crosslinks becomes smaller.<sup>102</sup> It was observed that BPACy and LECy had the highest  $h_\alpha$ , signifying the difunctional networks had longer average distances between crosslinks. In addition, the width at half height ( $\sigma_\alpha$ ) can be related to the network homogeneity, since the alpha transition is broader as network loosening increases. As can be seen in Figure 4.16 the  $\sigma_\alpha$  for the LECy and BPACy are similar. The similar  $\sigma_\alpha$  and  $h_\alpha$  values indicate a similar network compaction for the difunctional networks.

The broad  $\tan \delta$  curve ranging from  $\sim 200$  to  $325$  °C for the cisResCy network suggests the polymer network is heterogeneous as the glass transition takes place over a wide temperature range. This increase in the heterogeneity of the cisResCy glassy network results from the multifunctional chemical structure of the cisResCy monomer, which when polymerized, produces regions ranging from limited crosslinking to highly crosslinked areas. The heterogeneity of the network architecture ultimately leads to a wide range of relaxation times or mobilities.<sup>103</sup> More specifically, the cisResCy molecular architecture may have broadened this transition through suppression of some backbone segmental motions (shift to high temperature) along with promoting others (shift to low temperature).

The moduli of the networks were also examined, shown in Figure 4.17 and summarized in Table 4.5.

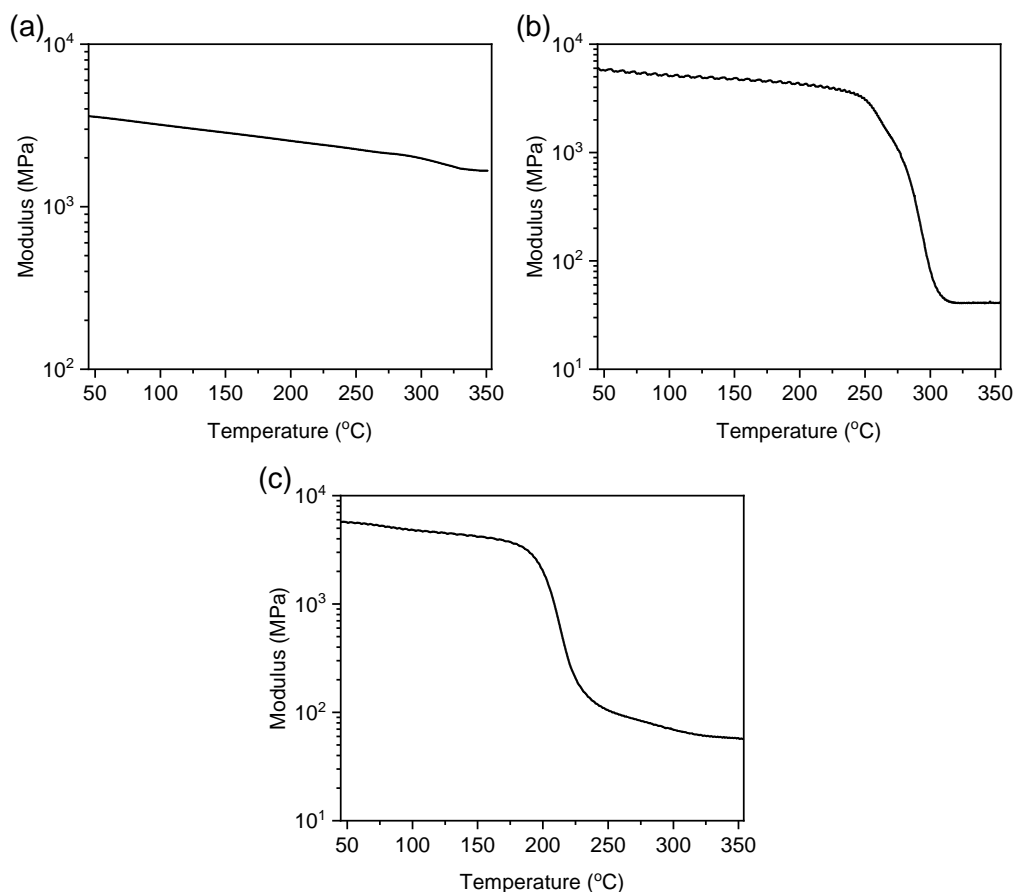


Figure 4.17  $E'$  vs. temperature for polymers of (a) *cisResCy*, (b) *BPACy*, and (c) *LECy*.

The storage modulus for the polymers at 50 °C were ranked in the following order: *BPACy* > *LECy* > *cisResCy*. The difference between the systems is on account of subtle variations in network architecture including crosslink density, entirely supporting the DSC results. Compared to the *cisResCy* polymer, the approximately ~1000 MPa increase in modulus of *BPACy* and *LECy* was attributed to the higher degree of cure for the difunctional networks. As mentioned in the previous section, the stilbene backbone rigidity of the *cisResCy* network prevents full conversion. The implication here is that there is a high free volume akin to chain ends from the *cisResCy* network, compared to

the difunctional BPACy and LECy networks, results in the higher modulus values for the latter networks.

Effects other than crosslink density should also be considered when examining the measured modulus values at 50 °C.<sup>102</sup> For example, it might be assumed that the exclusive consideration of the network stiffness would be that crosslinked networks formed from cisResCy (three cyanophenyl moieties connected by a rigid stilbene linking group) would be higher than those containing aliphatic backbones (BPACy and LECy). While this is not the case for cisResCy (for reasons stated above), this rationale may be used to explain differences in modulus between BPACy and LECy. More specifically, BPACy has a sterically hindered dimethyl substitution in between crosslinks, resulting in a stiffer polymer backbone and therefore, a higher modulus compared to LECy.

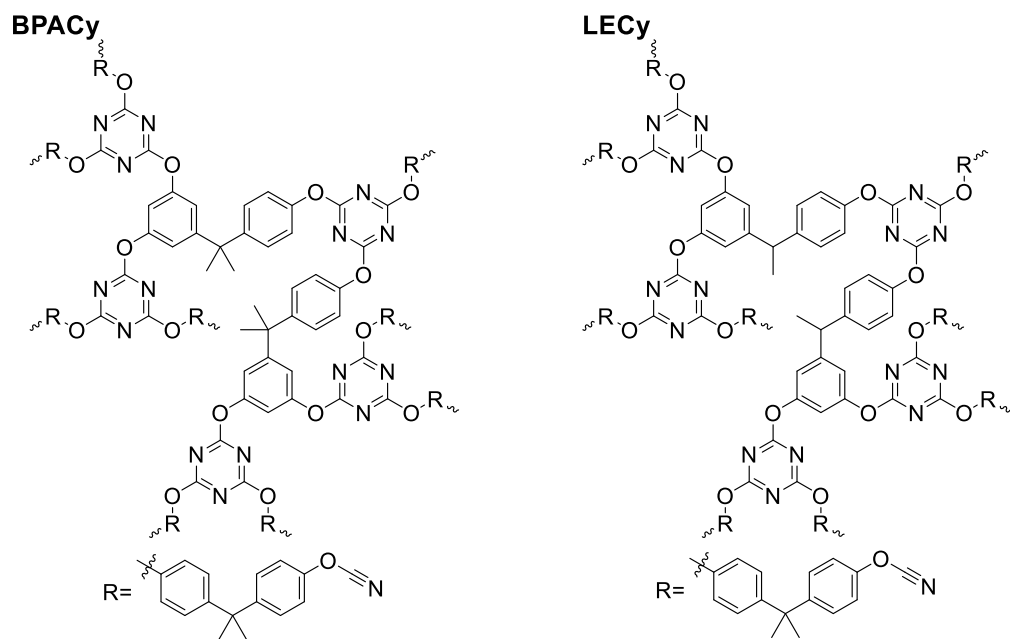


Figure 4.18 *Difunctional polymer networks.*

As polymers are continually heated, the networks reach the rubbery plateau, in which the molecular chains are highly mobile. Examination of the samples' moduli in this rubbery region provided relevant information regarding differences in the glassy polymer network architectures. The storage modulus at 350 °C for networks are ranked in the following order:  $\text{cisResCy} > \text{LECy} > \text{BPACy}$ . It is immediately obvious that there is a significant knockdown in the rubbery moduli for the two difunctional networks. It was, however, surprising that the modulus for  $\text{cisResCy}$  did not exhibit a characteristic drop in the storage modulus, commonly observed above the  $T_g$ . For example, the moduli for BPACy and LECy decreased by 99% and 92%, respectively, from 50 to 350 °C. On the other hand, the modulus for  $\text{cisResCy}$  decreased by 40%. This finding may be rationalized by considering the theory of rubbery elasticity, where the rubbery modulus value in the rubbery state is related to crosslink density. Based on this finding, it appears

that the cisResCy monomer chemical structure based on the double meta substitution and one para substitution promotes the formation of the densest network.

The crosslink density was calculated from the previous DMA measurements, according to the theory of rubber elasticity, and summarized in Table 4.5. The crosslink density was highest for networks of trifunctional cisResCy, and were lowest for the difunctional networks. The variations in T<sub>g</sub> and crosslink density between the three crosslinked networks were observed, which is evidence of variations in network architecture. It was observed that as the average functionality increased, so did the crosslink density.

#### 4.2.4 TGA

The glassy amorphous polymers were investigated with TGA, as shown in Figure 4.19 and summarized in Table 4.6.

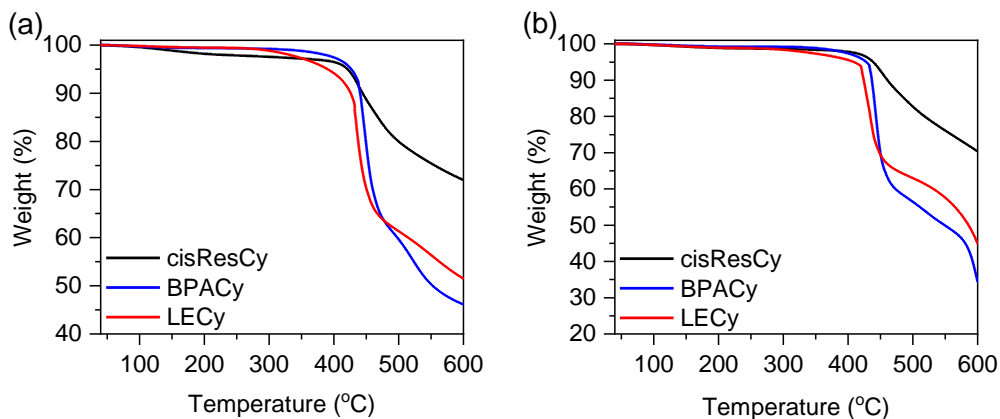


Figure 4.19 *Mass loss vs. temperature for polycyanurates.*

Table 4.6 *Thermal degradation of industrial polycyanurates in Nitrogen and Air*

System	T <sub>5%</sub> (°C)		T <sub>10%</sub> (°C)		Char Yield 600 °C (%)	
	N <sub>2</sub>	Air	N <sub>2</sub>	Air	N <sub>2</sub>	Air
<b>cisResCy</b>	421	439	444	461	71	71
<b>BPACy</b>	427	428	440	437	46	34
<b>LECy</b>	390	409	426	424	52	45

All networks exhibited excellent thermal stability with onsets of degradation (T<sub>5%</sub>) greater than 380 °C. The decomposition temperatures increased somewhat for polymers of cisResCy, which was expected due to the high degree of unsaturation. This decreased stability of BPACy is likely due to a higher concentration of chain ends.

### 4.3 Conclusions

The synthesis, purification, and network development of a *cis*-resveratrol cyanate ester (cisResCy) was investigated and compared with cyanate esters based on bisphenol A (BPACy) and bisphenol E (LECy). DSC analysis of thermal polymerization demonstrated the development of network architecture varied widely for the three polymer types, and the enthalpy of polymerization was highest for LECy and lowest for cisResCy. The relatively higher value for LECy was attributed to the monomer flexibility and low steric hinderance of the growing polymer backbone. The degree of polymerization decreased with an increase in monomer functionality and backbone steric hinderance in the order of: LECy > BPACy > cisResCy. For cisResCy, this result reflects the topological constraints of the highly crosslinked network formed from monomers containing three cyantophenyl groups, connected by an ethylene group. For BPACy reached a lower degree of cure than LECy because the BPACy backbone segments were sterically hindered from the double methyl substitution. The variations in network

architecture also had intriguing consequences for thermomechanical properties. While the moduli of the networks were arguably comparable at 50 °C, the knockdown of the rubbery moduli at 350 °C was substantial for the difunctional networks (BPACy and LECy). For cisResCy, however, the high temperature modulus for cisResCy was largely maintained, with a 40% decrease in the moduli from the glassy (50 °C) to rubbery (350 °C) states. A larger decrease in moduli was observed for BPACy (99%) and LECy (92%). Crosslink density calculations supported the results, where cisResCy had the highest crosslink density.

These polycyanurates provided unique opportunity to investigate the effect of monomer chemical structure on network growth and architecture. By understanding the fundamental relationships between molecular flexibility, functionality, and crosslink density, we can intelligently design novel cyanate esters from sustainable sources with targeted high temperature properties and glassy polymer network architecture.

## CHAPTER V – THERMAL DEGRADATION OF POLYCYANURATES

### 5.1 Abstract

Substantial changes in network thermal and thermo-oxidative stability behavior between petroleum-based difunctional cyanate esters (BPACy and LECy) and bio-based cyanate ester (cisResCy) were apparent from thermogravimetric analysis and ablation behavior. These polymers were characterized via TGA, TGA-MS, cone calorimetry, SEM, and EDX. The TGA and TGA-MS results revealed excellent thermal stability for the networks with onset of degradation  $> 400$  °C and char yields above 40 % at 900 °C. Examination of dTGA and decomposition gasses revealed the release of CO<sub>2</sub> in the first degradation step, followed by the release of CH<sub>4</sub> and NH<sub>3</sub>. Cone calorimetry data revealed the network from cisResCy produced a decrease in Total Heat Release (THR). This finding was attributed to the high char yield and thermal stability of the cisResCy polymer network due to the high crosslink density and degree of unsaturation.

### 5.2 Results and Discussion

For polymeric materials, including polycyanurates, the nature of monomer chemical structure and network architecture govern material properties including decomposition temperature, char yield, and flammability. The thermal and thermo-oxidative stability are themselves functions of aromaticity, crosslink density, degree of unsaturation, functionality and chain ends. The thermal/thermo-oxidative stability, decomposition gasses, and combustion behavior of three polycyanurates were studied by TGA, TGA-MS, cone calorimetry, SEM and EDX to develop a deeper understanding of the impacts of chemical structure on polycyanurate degradation.



Polymer networks were polymerized according to the following cure protocol: 160 °C (2h), 180 °C (2h), 200 °C (2h), 220 °C (2h). It was hypothesized that networks with high degrees of unsaturation (cisResCy) would exhibit the best thermal stability and compact carbonaceous char layer, whereas networks from saturated monomers (BPACy and LECy) would have the lowest thermal stability.

### **5.2.1 TGA**

Thermally polymerized polycyanurates prepared from cisResCy, BPACy, and LECy were analyzed via TGA in both an inert nitrogen and oxidizing air environment, to determine the Decomposition Temperature ( $T_{5\%}$ ), Maximum Degradation Temperature ( $T_{\max}$ ), and char yield at 900 °C. These results are shown in Figure 5.1 and summarized in Table 5.1.

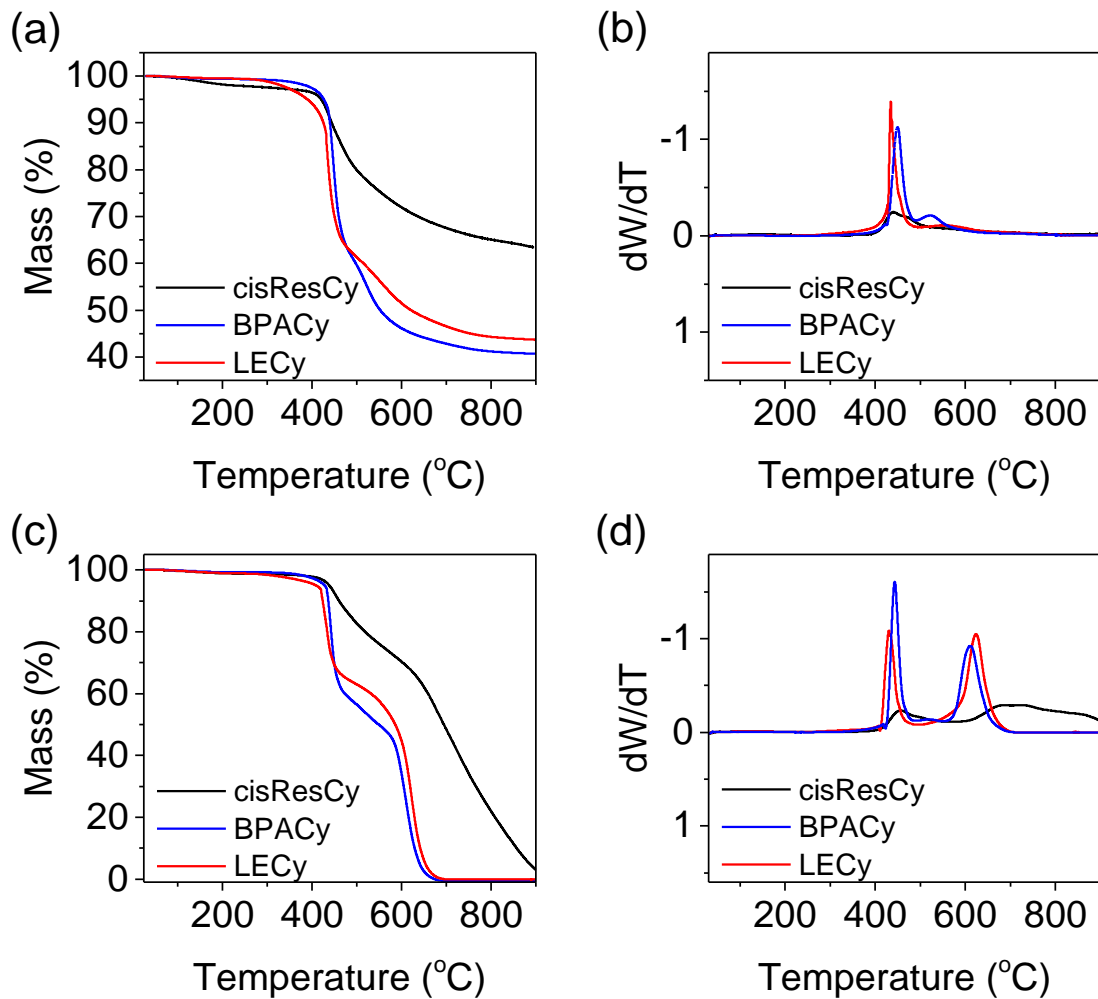


Figure 5.1 TGA plots of: (a) mass loss vs. temperature in nitrogen, (b) derivative of the mass loss vs. temperature in nitrogen, and (c) mass loss vs. temperature in air, and (d) derivative of the mass loss vs. temperature in air.

Table 5.1 *Thermal degradation temperatures for polycyanurates*

System	T <sub>5%</sub> (°C)		T <sub>max</sub> (°C)		Char 900 °C (%)	
	N <sub>2</sub>	Air	N <sub>2</sub>	Air	N <sub>2</sub>	Air
<b>cisResCy</b>	421	439	439	455	63	3
<b>BPACy</b>	427	428	444	445	41	0
<b>LECy</b>	390	409	434	427	49	0

All of the glassy amorphous polymers displayed excellent thermal stability with T<sub>5%</sub>'s approximately equal to or greater than 400 °C. The T<sub>5%</sub>'s of cisResCy and BPACy were greater than LECy on account of the greater thermal stability. This result was expected, as it was hypothesized that thermal stability would increase in rough proportion to the mole fraction of unsaturated bonds in the polymer backbone.

The T<sub>max</sub>'s for the polymers are shown in Table 5.1. In nitrogen, the values are similar for all of the polymers. This finding suggests that the T<sub>max</sub>'s are relatively insensitive to the monomer chemical structure in the event of purely thermal degradation. In an air environment, the T<sub>max</sub> for is highest for cisResCy (455 °C) and lowest for BPACy (445 °C) and LECy (427 °C). The similar T<sub>max</sub>'s suggest that in the event of purely thermal degradation, the peak degradation temperature is relatively insensitive to the monomer chemical structure.

From the dTGA in Figure 5.1, it can be seen that all of the polycyanurates exhibit a two-step weight loss. In nitrogen, the first degradation step peaked at approximately 435 °C and the second degradation peaked at approximately 560 °C. Similar results exhibiting a two-step degradation process has been previously published by Ramirez et al.<sup>49</sup> The first major mass loss was accredited to chain scission and crosslinking of the

polymer backbone without substantial loss of mass, and the second decomposition step was attributed to decyclization of the cyanurate ring ( $> 450\text{ }^{\circ}\text{C}$ ).

For all polymers in air, the first degradation step occurred at nearly identical values to those measured in  $\text{N}_2$ , which revealed that thermo-oxidative degradation is not significantly accelerated below  $400\text{ }^{\circ}\text{C}$  compared to purely thermal degradation. However, this degradation is accelerated above  $400\text{ }^{\circ}\text{C}$  in air. These results are likely due to reactions between oxygen and polymer alkyl radicals.<sup>104</sup> More specifically, the decrease in thermal stability at high temperatures in an oxidizing environment has been attributed to the hydrolysis of the oxygen bond attached to the triazine ring, followed by decyclization of the cyanurate ring and the release of small organic molecules.<sup>48</sup>

The char yields of the thermally cured polymers in nitrogen and air were ranked in the following order:  $\text{cisResCy} > \text{LECy} > \text{BPACy}$ . It is noteworthy that in nitrogen the polymer from  $\text{cisResCy}$  has a char yield  $\sim 20\%$  higher than the networks from  $\text{BPACy}$  and  $\text{LECy}$ , which is likely on account of the high degree of unsaturation of the  $\text{cisResCy}$  polymer backbone that is mainly constructed of repeating units linked together via triply substituted cyanurate rings.<sup>22</sup>

### **5.2.2 TGA-MS**

To further examine the differences in network degradation between the three crosslinked networks and characterize the volatile decomposition products, TGA-MS was used (Figure 5.2 and Figure 5.3). It should be mentioned analysis of the thermal degradation molecules does not show evidence of high molecular weight molecules. It is possible that the gas transport temperatures were unable to maintain the volatility of the higher molecular weight species.

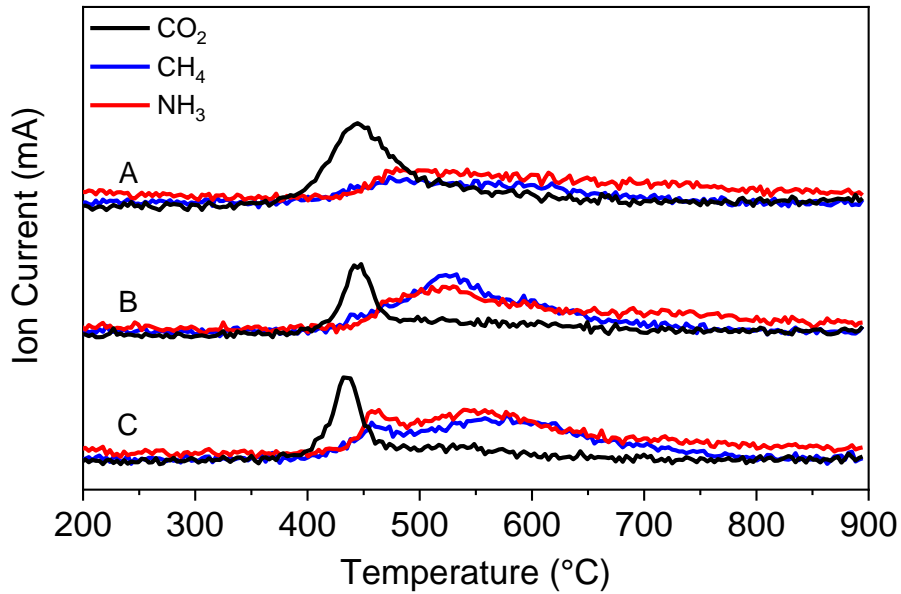


Figure 5.2 Ion current vs. temperature for (A) *cisResCy*, (B) *BPACy*, and (C) *LECy* in nitrogen.

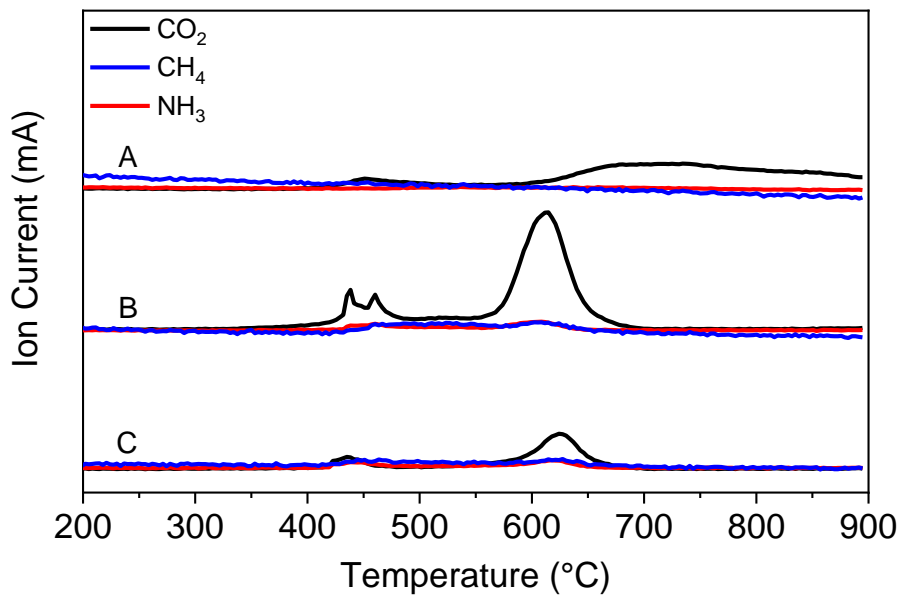


Figure 5.3 Ion current vs. temperature for (A) *cisResCy*, (B) *BPACy*, and (C) *LECy* in air.

It can be seen that there were no major changes in the concentration of small volatile species before 400 °C, which suggests little thermal degradation has occurred. At temperatures greater than 400 °C, the concentration of CO<sub>2</sub> increases rapidly. The appearance of CO<sub>2</sub> above 400 °C indicated backbone breaking reactions via chain scission of ether bonds adjacent to cyanurate rings. The subsequent appearance of NH<sub>3</sub> is due to a multistep process which begins with the decyclization of the cyanurate rings to form carbamates that degrade to carbamic acid. This acid is an unstable intermediate, which degrades to CO<sub>2</sub> and ammonia. The appearance of CH<sub>4</sub>, NH<sub>3</sub>, and CO<sub>2</sub> for all of the spectra suggests there is no change in the degradation mechanism between the three different crosslinked networks.

In air the thermo-oxidative degradation commences with the rapid appearance of CO<sub>2</sub> at temperatures greater than 400 °C (Figure 5.3). A noteworthy observation is the large magnitude of the second degradation step at approximately 550 °C. From approximately 550 to 650 °C there is a sharp increase in CO<sub>2</sub>, CH<sub>4</sub>, and NH<sub>3</sub>. This second event is in excellent agreement with the dTGA results and suggests major degradation of the primary residue resulting in full consumption of the crosslinked samples. The difference in the magnitude of the second degradation step in air, compared to that in nitrogen, during dynamic TGA-MS experiments reflects the acceleration of degradation in air due to the thermo-oxidative degradation of the primary residue. In air, the crosslinking reactions are unable to contest the breakdown of the polymer backbone.

### 5.2.3 Cone Calorimetry

Cone calorimetry experiments were performed on crosslinked polymers to measure fire behavior. Measured parameters include Time to Ignition (TTI), Total Heat Released (THR), Heat Release Rate (HRR), Peak Heat Release Rate (PHRR), and smoke generation, which are shown in Figure 5.4 and summarized in Table 5.2.

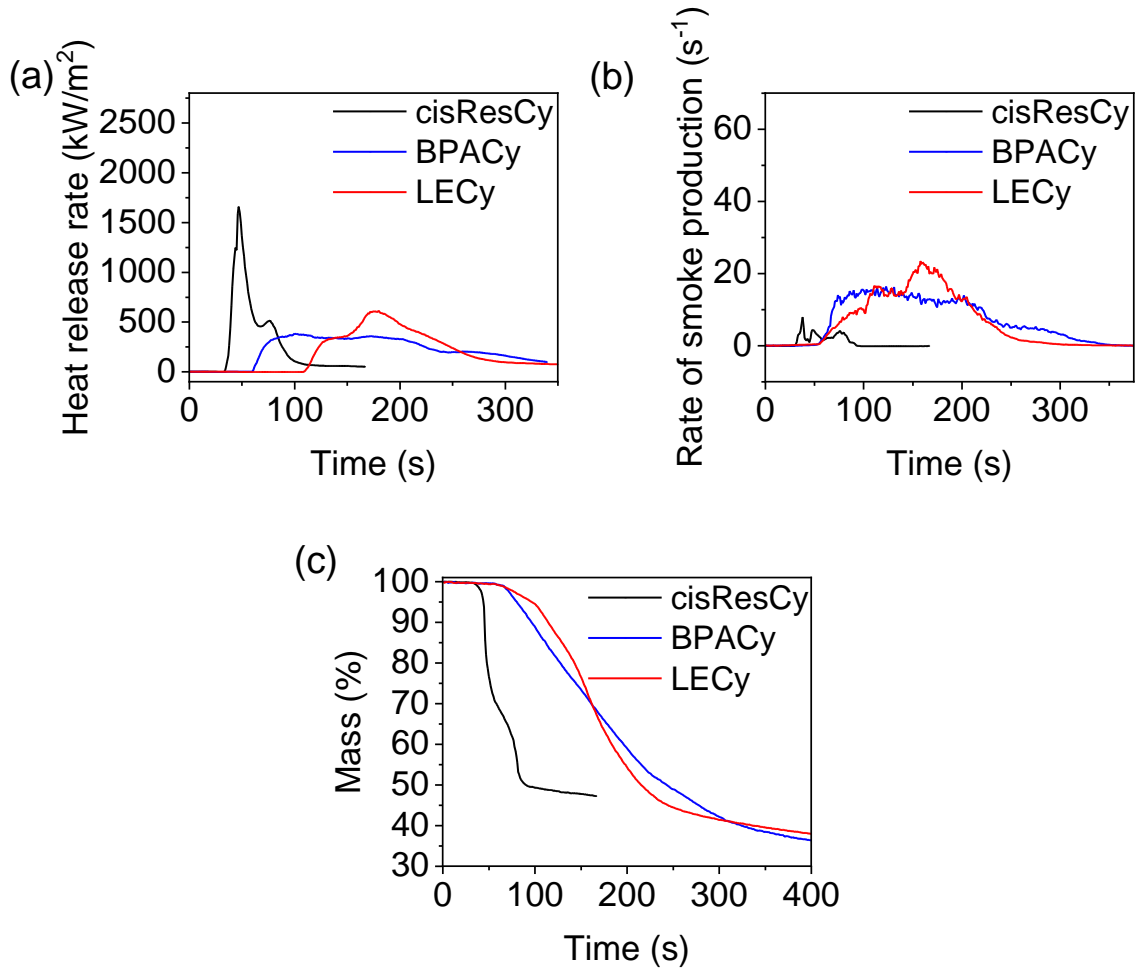


Figure 5.4 (a) Heat release rate vs. temperature, (b) rate of smoke production vs. temperature, and (c) mass loss vs. temperature.

Table 5.2 *Combustion behavior of polycyanurates using from calorimetry experiments*

<b>Sample</b>	<b>TTI (s)</b>	<b>pHRR (kW/m<sup>2</sup>)</b>	<b>THR (MJ/m<sup>2</sup>)</b>	<b>CO yield</b>	<b>CO<sub>2</sub> Yield</b>
cisResCy	39	1659	42	0.03	1.8
BPACy	66	383	85	0.07	2.5
LECy	101	612	72	0.09	2.8

The networks had TTI values in the following order: cisResCy < BPACy < LECy. These results indicate variations in the polymer network architectures, and reflect differences in degree of polymerization between the samples. For instance, cisResCy had the lowest TTI, presumably because of the greater propensity of the dangling unreacted chain ends to combust. In addition, LECy has the highest TTI, and lowest concentration of unreacted groups (highest degree of polymerization) as shown in the previous chapter.

It can be seen in Figure 5. 4 that the HRR versus time curve for the networks vary for each of the studied polymer networks. For BPACy there is an increase in the HRR upon ignition at 66 s. By approximately 100 s the HRR curve reaches the PHRR value of 383 kW/m<sup>2</sup>. Interestingly, after the PHRR is reached the HRR forms a “platform” area, evidence of the formation of a protective char layer.<sup>105</sup> For LECy, upon ignition (101 s) the HRR jumped to approximately 340 kW/m<sup>2</sup> forming a shoulder (130 to 150 s), which indicated the start of char formation. However, the HRR jumped to 612 kW/m<sup>2</sup> (180 s), indicating cracking that exposed a high concentration of volatiles at once. For cisResCy, the PHRR was reached at 47 s (1658 kW/m<sup>2</sup>), approximately 8 s after ignition. The intensity of the first peak clearly implies an increase in the oxygen combustion rate, compared to the other polymer networks. It should be mentioned PHRR for cisResCy



was an order of magnitude larger than the other samples. This result is once again related to the degree of polymerization. The high structural rigidity of the cisResCy monomer likely did not allow the polymer to fully cure, and when combined with the increased concentration of chain ends and low molecular weight oligomers, contribute significantly to the observed higher pHRR. Interestingly, these results agree with previous findings by Garrison et al.<sup>59</sup> who studied the cure chemistry and thermomechanical properties of cisResCy blends with commercially available cyanate ester monomers. DSC studies showed that the structural rigidity of the monomer and 1.5 –OCN groups per aromatic ring do not allow cisResCy to fully cure, even with a high-temperature post-cure.

The cisResCy networks had the lowest THR, followed by LECy and BPACy. The low THR of the cisResCy network is likely an artifact of the polymer char yield (Figure 51c), which supported the TGA results presented in the previous section. The total mass retained for the cisResCy network (as measured by cone calorimetry) is greater than the other two networks. The high mass retention was likely on account of the high degree of unsaturation of the cisResCy polymer backbone.

The primary cause of death by fire is on account of toxic gasses, therefore, smoke suppression is a critical property for high temperature polymer materials. The smoke data from the cone calorimetry experiments are shown in Figure 5.5 and summarized in Table 5.2.

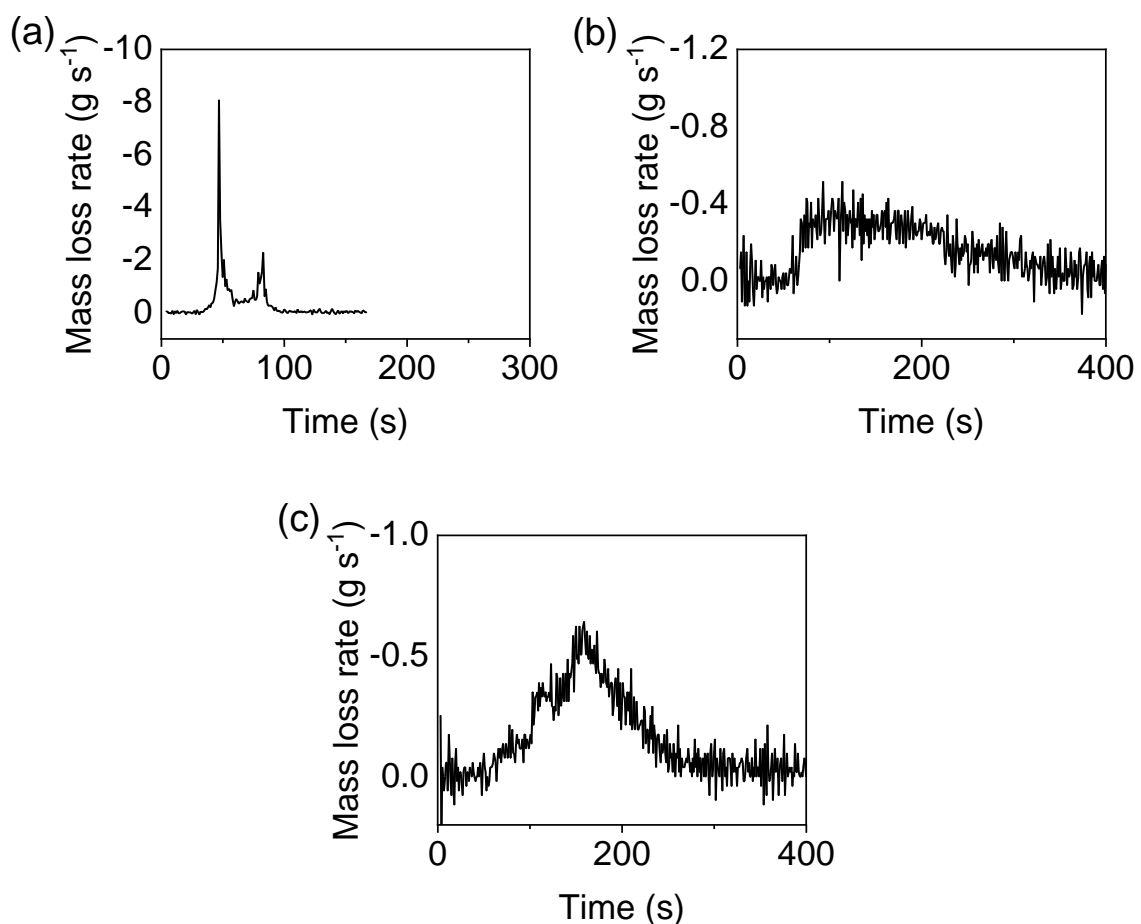


Figure 5.5 The rate of mass loss vs. temperature for (a) *cisResCy*, (b) *BPACy*, and (c) *LECy*.

It can be seen in Table 5.2 that *cisResCy* exhibits the lowest CO and CO<sub>2</sub> yield compared to the other networks. This is advantageous, due to the high flammability and toxicity of CO, and the environmental problems commonly associated with CO<sub>2</sub>. For *BPACy* and *LECy*, there are large peaks in the rate of smoke production – time curve, signifying that the difunctional polycyanurate networks produce a higher concentration of smoke upon ignition (compared to *cisResCy*). The rate of smoke production versus time

graph corresponds well with the mass loss rate, meaning that smoke production is a factor in mass loss.

#### 5.2.4 Visual Inspection of Charred Specimens

Figure 5.6 shows digital photographs of the carbonaceous chars of the three polymer networks after the cone calorimetry experiments.

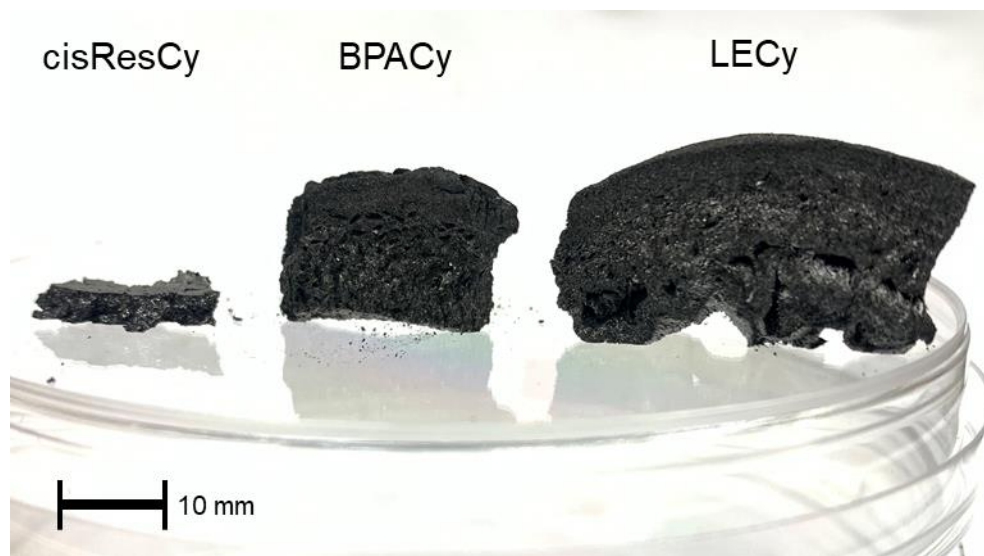


Figure 5.6 *Carbonaceous char residues of polycyanurates.*

The image demonstrates the difference in the thickness of the char residues, which are ranked in the following order:  $\text{cisResCy} < \text{BPACy} < \text{LECy}$ . LECy showed the highest char swelling of all of the samples and it can be seen that the LECy char had very large and irregular pores. On the other hand, the cisResCy char is denser and more compact, and it is difficult to see pores and voids. It should also be mentioned that the cisResCy sample was the most severely damaged, compared to BPACy and LECy. More specifically, while the difunctional charred networks (BPACy and LECy) fractured into several pieces, the cisResCy char residue completely collapsed into small chips. This

thermal shrinkage and resultant mechanical breakdown were likely caused from the substantial heat generation of cisResCy during the cone calorimetry experiment. On the other hand, the low molecular weight between crosslinks for the cisResCy network, and rigid backbone, may also rationalize the observed brittle fracture.<sup>106</sup>

### **5.2.5 SEM**

The SEM images of the residual chars from the cone calorimeter experiments are shown in Figure 5.7. It was found that the CE network architecture has a great effect on the porous nature of the resulting structures. The average pore size of the carbonaceous structure decreased in the order of LECy > BPACy > cisResCy. For cisResCy the resulting carbonaceous structure exhibited a plate-like morphology and small pores approximately 5 to 10  $\mu\text{m}$  in diameter. Both BPACy and LECy exhibit large pores with uneven sizes in the range of 50-200  $\mu\text{m}$ .

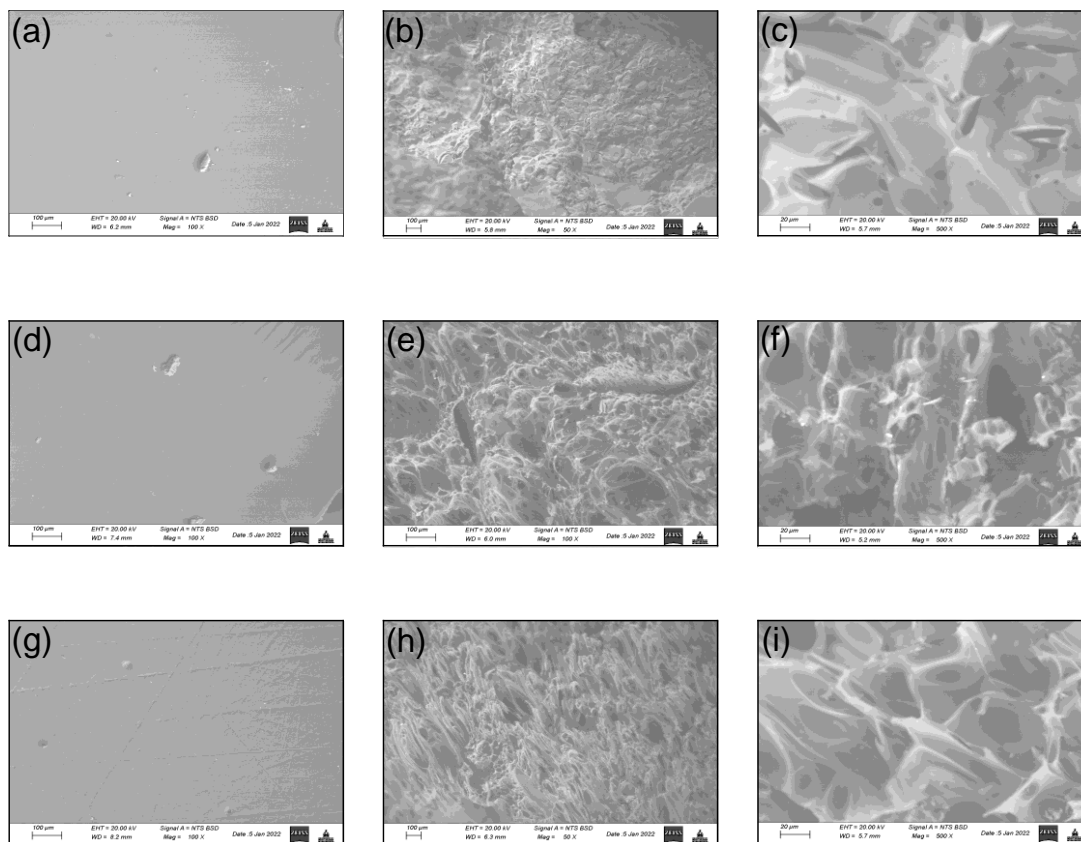


Figure 5.7 SEM micrographs of (a) *cisResCy*, (b) *cisResCy* char low magnification, (c) *cisResCy* char high magnification, (d) *BPACy*, (e) *BPACy* char low magnification, (f) *BPACy* char high magnification, (g) *LECy*, (h) *LECy* char low magnification, and (i) *LECy* char high magnification.

The variation in the size of the pores and thickness of the pyrolyzed specimens demonstrate that the monomer chemical structure and network architecture influences the formation of these morphological features. For example, the trifunctional *cisResCy* network has the highest crosslink density which may have impeded void and bubble formation during pyrolysis, and resulted in the small pore size of the carbonaceous residue.<sup>107</sup> Alternatively, the brittle fracture (discussed in the previous section) may have

served to provide heat transfer and gas diffusion, precluding the network from forming large pores.

### 5.2.6 EDX

Elemental analysis via EDX was used to investigate the virgin polymers, char surface, and char cross-section (Table 5.3).

Table 5.3 *EDX data*

<b>Sample</b>	<b>C</b>	<b>% error (+/-)</b>	<b>N</b>	<b>% error (+/-)</b>	<b>O</b>	<b>% error (+/-)</b>
cisResCy	54.32	0.28	15.03	2.08	30.66	0.58
cisResCy char surface	61.52	0.37	17.03	2.29	21.45	0.72
cisResCy char cross-section	61.70	0.42	17.09	2.91	21.21	0.91
BPACy	63.62	0.31	14.76	2.22	21.62	0.57
BPACy char surface	70.29	0.38	16.91	2.34	12.80	0.70
BPACy char cross-section	73.70	0.40	17.86	2.46	8.44	0.74
LECy	59.57	0.30	12.83	2.43	27.59	0.62
LECy char surface	74.32	0.36	25.68	1.11	0.00	0.00
LECy char cross-section	73.77	0.36	26.23	1.15	0.00	0.00

The elemental analysis for the surface and cross-section of the pyrolyzed specimens illustrate the representative compositional changes for the polymer networks.

For all of the pyrolyzed samples there was a decrease in the surface oxygen concentration compared to the virgin polymers, illustrating the preferential decomposition of ether bonds adjacent to cyanurate rings via chain scission. It is worth noting that LECy and BPACy exhibit a more dramatic decrease in oxygen concentration, compared to cisResCy. This suggests that the LECy, and to a lesser degree BPACy, have difficulty in contesting the breakdown of the polymer backbone upon pyrolysis. The cisResCy network exhibits less oxygen consumption presumably because of its higher thermal stability on account of the high aromatic content and close packing of the cyanurate rings.

### **5.3 Conclusions**

Progress towards a molecular-level understanding of CE monomer chemical structure on polymer degradation and flammability was advanced. Through the use of CEs with varying order of functionality and variety of bridging groups we characterize fundamental structure-property relationships of polymer networks. Cone calorimetry results reflected changes in materials properties that could be correlated to changes in degree of polymerization. The HRR peak upon ignition increased for the cisResCy polymerized sample, indicating a change in molecular architecture. For this network, the HRR peak upon ignition was attributed to the increase in monomer functionality and rigid stilbene structure, followed by the polymer unable to fully cure (likely to have low MW oligomers present). For the networks from difunctional CE's with flexible  $sp^3$  bridging groups, the HRR peaks upon ignition did not jump to high values because the high crosslink density. While the HRR changes were driven by degree of polymerization, the char yield values likely contributed to the changes in THR.

## CHAPTER VI – STRUCTURE-PROPERTY RELATIONSHIPS OF BIOBASED CYANATE ESTER BLENDS

### 6.1 Abstract

Monofunctional and trifunctional cyanate ester monomers, cardanol-cyanate ester (1-cyanato-3-pentadecylbenzene, CardCy) and cis-resveratrol-cyanate ester (cis-3,4',5-tricyanatostilbene, cisResCy), respectively, were synthesized from biobased cardanol and resveratrol. The cisResCy monomer was blended with varying weights of CardCy and co-cured to produce five polycyanurate networks (a – e). The cyanate ester monomers were low melting solids ( $T_m < 83$  °C). The polymerization exotherms measured with Differential Scanning Calorimetry (DSC) exhibited “tunable” exotherm maxima, relating to cyanate ester cyclotrimerization. The activation energies for cyanate ester polymerization were calculated by Kissinger’s and Ozawa’s methods. Thermal and thermomechanical properties including char yield and modulus were evaluated with Thermogravimetric Analysis (TGA) and Dynamic Mechanical Analysis (DMA). The organic polymers displayed outstanding thermal stability and enhanced mechanical dampening, establishing the utility of plant-derived cyanate ester formulations to design sustainable thermosets for high performance applications.



## 6.2 Results and Discussion

### 6.2.1 Monomer Synthesis

The cisResCy and CardCy monomers were synthesized from *cis*-resveratrol and cardanol, respectively, through reaction with cyanogen bromide in the presence of triethylamine, following synthetic procedures reported by Grigat and Putter.<sup>108</sup> Purified cisResCy appeared as colorless needle-like crystals, and CardCy was an oily amber liquid at room temperature, and when stored in a freezer (~3 to 5 °C). The structure and purity of the monomers were confirmed for purity and structure by <sup>1</sup>H NMR and FTIR. The <sup>1</sup>H NMR spectra for purified cisResCy, cardanol and CardCy are shown in Figure 6.1, Figure 6.2, and Figure 6.3 respectively.

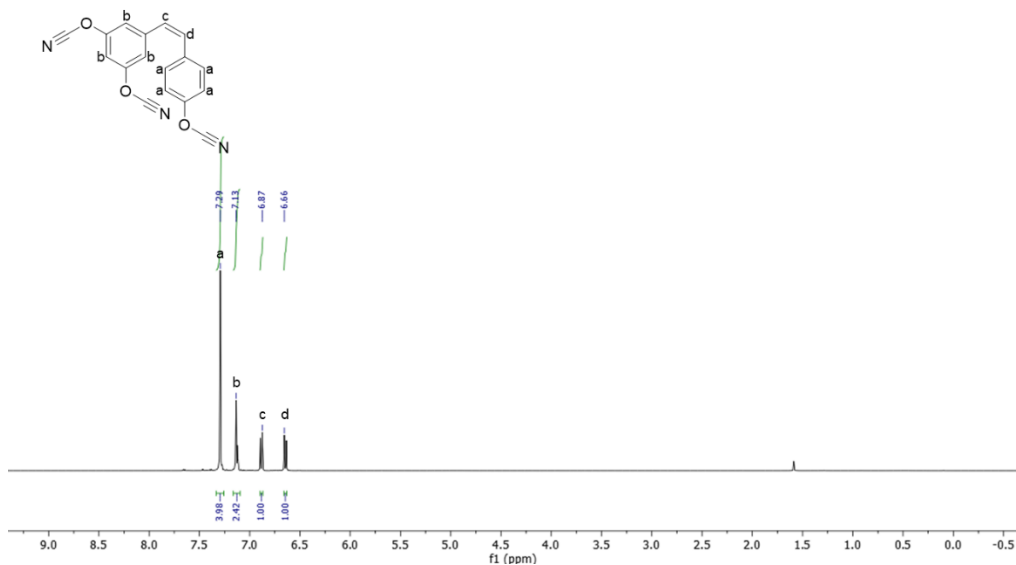


Figure 6.1 <sup>1</sup>H NMR of cisResCy.

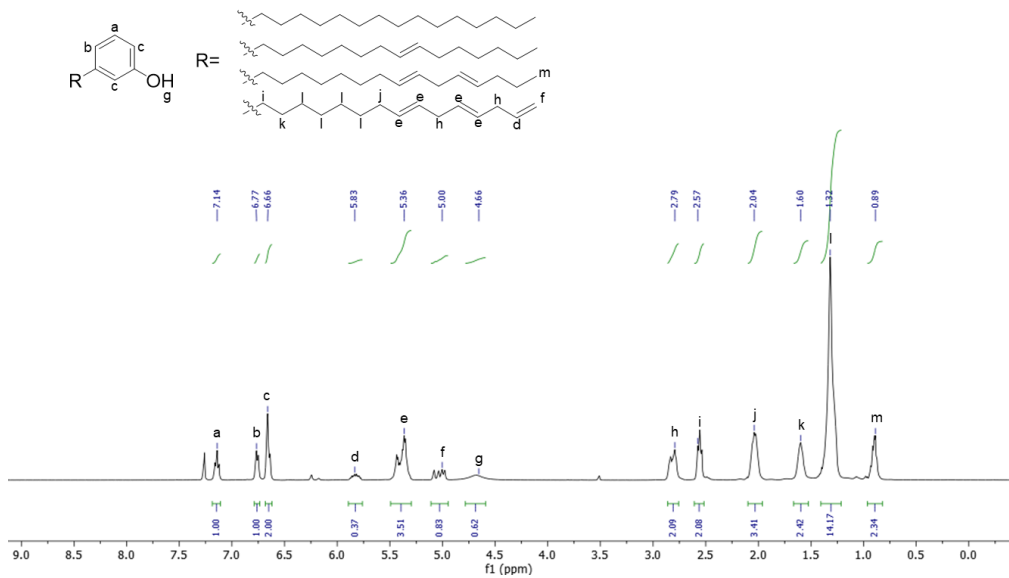


Figure 6.2  $^1\text{H}$  NMR of Cardanol.

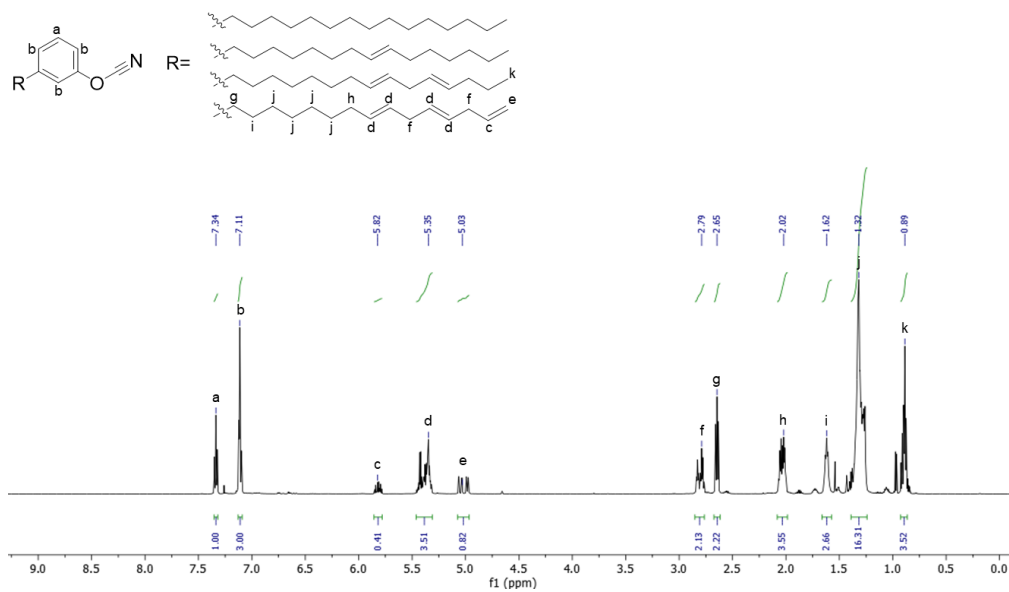


Figure 6.3  $^1\text{H}$  NMR of CardCy.

The CardCy monomer exhibited the characteristic protons of the benzene ring from 7.14-7.37 ppm. The protons of the unsaturated double bonds in the alkyl side chain corresponded to the signals from 5.06 to 5.85 ppm, and the protons adjacent to C=C corresponded to signals at 2.07 and 2.82 ppm.<sup>109</sup> The breadth in the resonance shift of the cardanol and CardCy was on account of the varying saturation of the alkyl tails. More specifically, previous structural analyses of cardanol performed by gas chromatography/mass spectrometry (GC/MS) has shown the composition of cardanol was 2.7% saturate, 39.2% monoene, 23.0% diene, and 35.1% triene (Figure 6.4).<sup>110</sup>

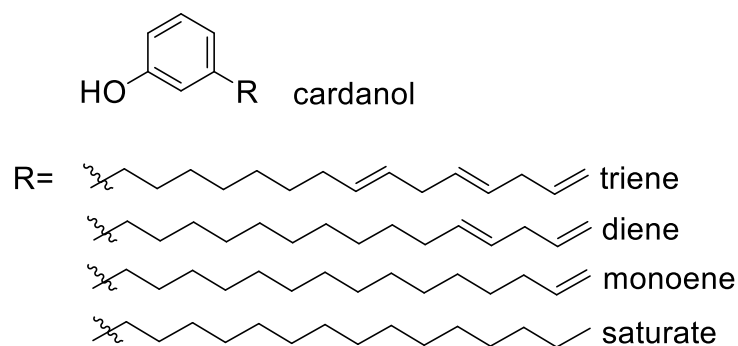


Figure 6.4 *The chemical structure of cardanol*

### 6.2.2 FTIR

The FTIR spectra of the monomers are shown in Figure 6.5. For both cyanate ester monomers, full conversion to cyanate functionality was indicated by the absence of an O-H stretch ( $3400\text{-}3600\text{ cm}^{-1}$ ) and the presence of strong  $\text{C}\equiv\text{N}$  and C-O-C stretches at  $2250\text{ cm}^{-1}$  and  $1160\text{ cm}^{-1}$ , respectively. The spectrum of CardCy indicated several typical peaks of the 15-carbon long side alkyl side chain including C-H stretch from the inner unsaturated moiety ( $3008\text{ cm}^{-1}$ ); methine, methylene, and methyl groups ( $1453$ ,  $2851$ ,  $2925\text{ cm}^{-1}$ ); C=C stretching of the aromatic ring ( $1149$  and  $1261\text{ cm}^{-1}$ ).<sup>111</sup>

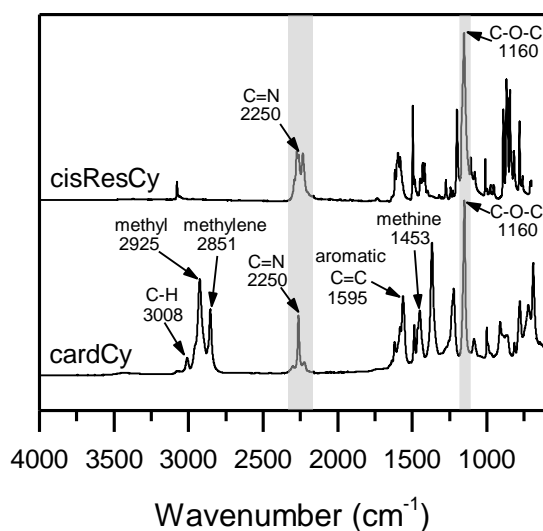


Figure 6.5 FTIR data for the cyanated monomers.

### 6.2.3 DSC

All CardCy/ cisResCy blends formed homogenous waxy solids that were analyzed using Differential Scanning Calorimetry (DSC). The dynamic thermograms of monomer samples shown in Figure 6.6 illustrate the melting temperatures, evidenced by the sharp endothermic transitions between 69 and 83 °C. Generally, the melting temperatures decreased with an increase in the weight percentage of CardCy (Table 6.1). This facilitates good monomer processability at reasonable temperatures, which is attractive for the fabrication of composites. The decrease in the melting temperatures can be attributed to an increase in molecular mobility upon the addition of the liquid monofunctional CE.

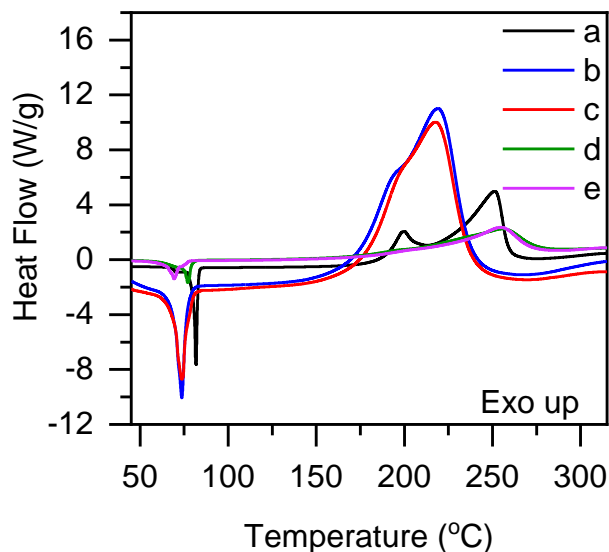


Figure 6.6 DSC thermograms of thermally polymerized cyanate ester monomers mixtures: (a) neat cisResCy, (b) 5 wt% CardCy/ cisResCy, (c) 10 wt% CardCy/ cisResCy, (d) 20 wt% CardCy/ cisResCy, and (e) 30 wt% CardCy/ cisResCy.

Table 6.1 DSC Values for the Following Monomer Blends: (a) neat cisResCy, (b) 5 wt% CardCy/ cisResCy, (c) 10 wt% CardCy/ cisResCy, (d) 20 wt% CardCy/ cisResCy, and (e) 30 wt% CardCy/ cisResCy

Network	T <sub>m</sub> (°C)	T <sub>o</sub> (°C)	T <sub>p</sub> (°C)	ΔH <sub>tot</sub> (J/g)	ΔH <sub>tot</sub> (kJ/-OCN)	Kissinger (kJ/mol)	Ozawa (kJ/mol)
<b>a</b>	83	245	264	585	66	76.8	81.6
<b>b</b>	81	239	260	545	56	52.5	58.3
<b>c</b>	74	217	255	490	53	59.7	65.5
<b>d</b>	77	215	247	417	49	58.9	64.2
<b>e</b>	69	183	236	400	51	53.9	59.2

Impurity levels as low as 2% may lead to considerable changes in melting endotherm shape, with increased levels of impurities leading to a broadening and a shift to lower temperatures. The difference in melting temperatures of the blends is most probably not a consequence of impurities, as it has been shown in the literature that for

BADCy a 7.2 mol% level of impurity will decrease the peak melting temperature by 6.6 °C.<sup>4</sup> While it is well known that impurities may catalyze the cyclotrimerization reaction, the absence of amine and triethylammonium hydrobromide salt in the <sup>1</sup>H NMR suggests the main impurity is the partially cyanated phenol analogue of the CE, phenolic starting materials have been previously (and unambiguously) identified as the main impurity in other studies.<sup>76</sup> It should also be mentioned that completely pure monomers may not even cure, therefore are of limited practical significance.<sup>76</sup> Nevertheless, it should be noted that the blends in the current study involve a difference in chemical structure (and wt %'s) of the constituents, along with a modest difference in the impurity set. With this in mind, we have deliberately examined and remarked on what role (if any) the impurity set differences may affect the results.

It can be seen in Figure 6.6 that all systems exhibited an exotherm with two overlapping peaks. This observation aligned with that of Garrison et al.<sup>14</sup> who used DSC to study the cyanate ester cure reactions for cisResCy /LECy, a bisphenol cyanate ester, and similarly observed overlapping peaks. This first peak was attributed to the isomerization of cisResCy to the more thermodynamically stable *trans*-isomer, and the second to the polymerization of cyanate ester groups.<sup>59,14</sup>

The onset of polymerization temperature ( $T_o$ ) and peak exotherm temperature ( $T_p$ ) for polycyanurate networks **a** – **e** are listed in Table 6.1. The  $T_o$ 's and  $T_p$ 's decreased with increased weight percentages of CardCy. All of the blends exhibited  $T_o$ 's below 245 °C and  $T_p$ 's lower than 264 °C, which was the  $T_p$  for cisResCy. The lower  $T_o$ 's and  $T_p$ 's for the blends may be rationalized on account of the presence of phenolic starting material, which is well understood to decrease the polymerization temperature for CE systems. On

the other hand, the monomer with a 15-carbon long alkyl chain meta to the cyanate reactive site may have increased the molecular mobility and reactivity toward cyclotrimerization mechanism of component mixtures.<sup>112-114</sup> As curing reactions proceed, the physical state of the system progresses from a liquid to a gel to a glassy solid. The increased flexibility and molecular mobility of the liquid CardCy monomers may enhance reactivity of monomers in the liquid state. A modest increase in reactivity of the CE blends owing to synergistic (non-linear) interactions requires a more detailed kinetic analysis to demonstrate the effect with certainty. To further support our findings, dynamic scanning experiments using both Kissinger<sup>63</sup> and Ozawa<sup>64</sup> approaches were utilized to determine kinetic parameters, which are shown in Figure 6.7, Figure 6.8, and tabulated in Table 6.2. Overall, the results illustrated the higher reactivity of CardCy blends compared to the cisResCy, due to the decrease in activation energy for polymerization.

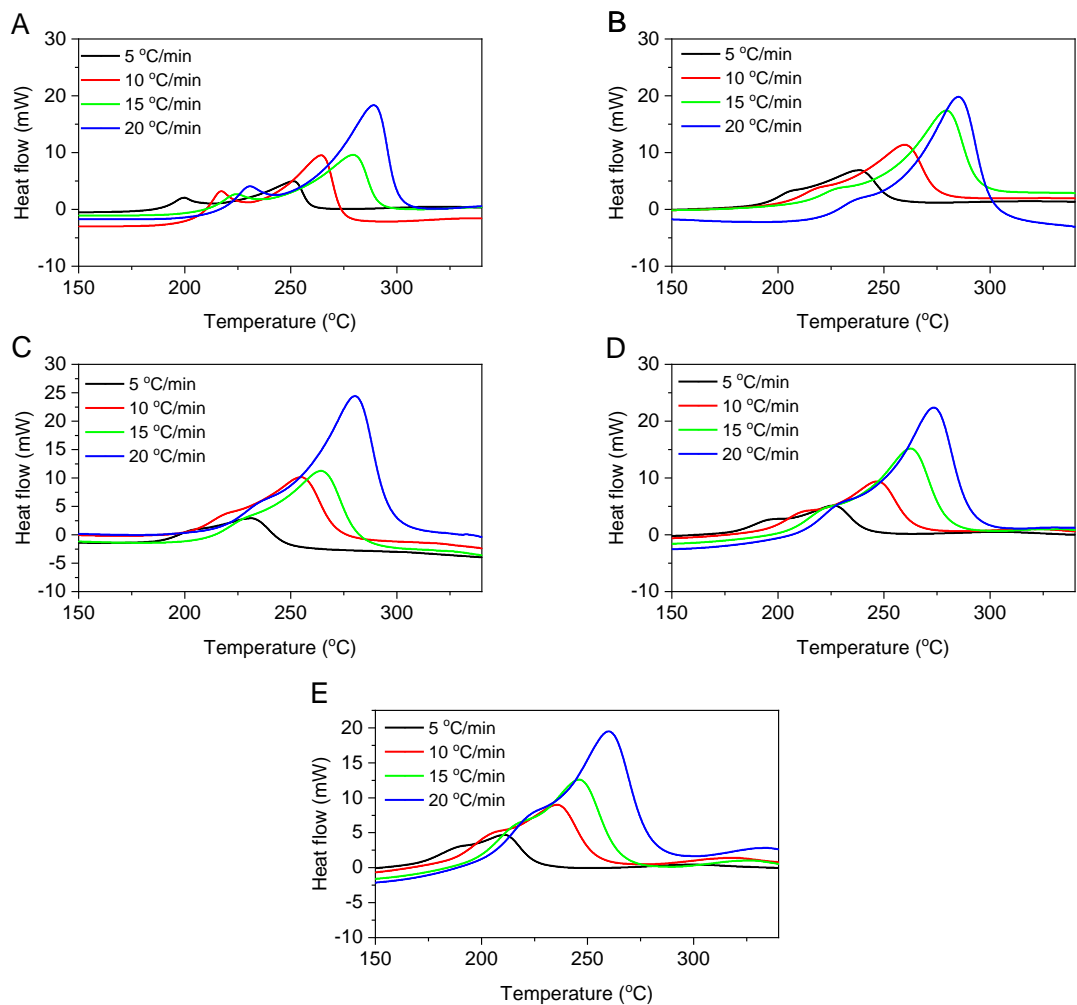


Figure 6.7 DSC thermograms at different heating rates for: (A) neat cisResCy, (B) 5 wt% cardCy/cisResCy, (C) 10 wt% cardCy/cisResCy, (D) 20 wt% cardCy/cisResCy, and (E) 30 wt% cardCy/cisResCy.



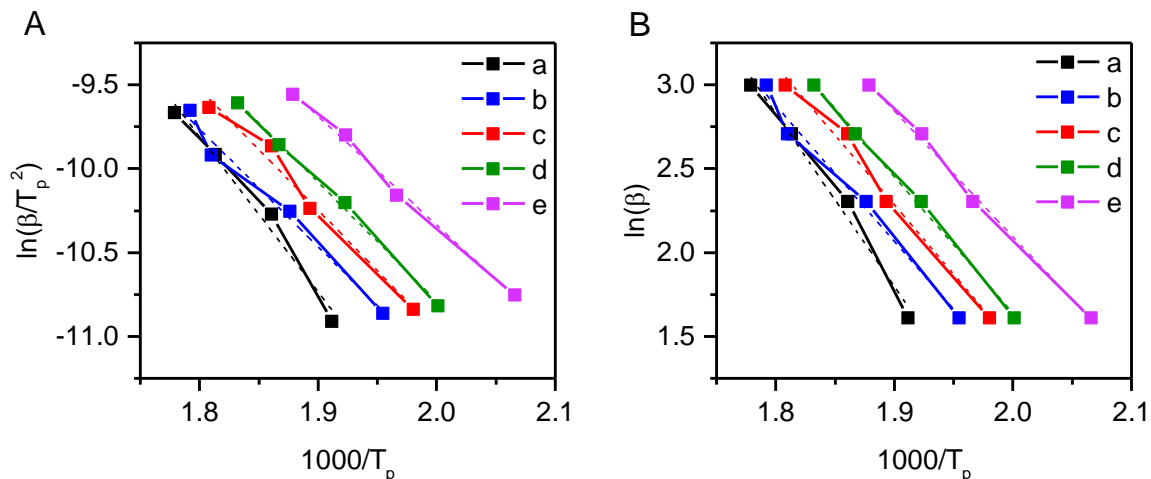


Figure 6.8 (A) Kissinger and (B) Ozawa plots for the calculation of activation energy for: (a) neat cisResCy, (b) 5 wt% cardCy/cisResCy, (c) 10 wt% cardCy/cisResCy, (d) 20 wt% cardCy/cisResCy, and (e) 30 wt% cardCy/cisResCy.

Table 6.2 Average activation energy of cisResCy/cardCy blends obtained by the Kissinger and Ozawa methods utilizing the peak exotherm temperatures, ranked on kJ/mol.

Network	a	b	c	d	e
Kissinger	76.8	52.5	59.7	58.9	53.9
Ozawa	81.6	58.3	65.5	64.2	59.2

Further differences in polymerization behavior were established in the polymerization enthalpy per mole of -OCN values, which are summarized in Table 6.3. Samples **a** and **b** had cure enthalpies of 66 kJ/(mol -OCN) and 60 kJ/(mol -OCN), respectively. Compared to the polymerization enthalpy of a commercial bisphenol A-based cyanate ester (108 kJ/cyanate)<sup>4</sup>, the value for cisResCy / CardCy blends are approximately halved. The lower cure enthalpies imply topological constraints of the highly crosslinked network prevent full conversion. After gelation (molecular weight of growing network is infinite) and vitrification (the  $T_g$  of the network exceeds the

temperature of the environment), chain motions are severely hindered. Upon vitrification the architecture is effectively “frozen” in the prevailing configuration. Unreacted groups may remain in the system but they are too constrained to collide and continue reacting. Understandably, full conversion was challenging to achieve due to the topological constraints of the network formed from monomers with three cyanophenyls connected by an ethylene linking group, in conjunction with endcapping from the monofunctional CardCy monomer. The enthalpies of polymerization for the blends were generally similar to the values expected from the linear rule of mixtures, especially for the blends with  $\leq$  10 wt% CardCy (Table 6.3). The blend with 5 wt% CardCy (**b**) had a polymerization enthalpy of 545 J/g, only 4% lower than expected (564 J/g) based on the linear rule of mixtures. In summary therefore, the DSC studies show that by increasing the weight percentage of CardCy there was a decrease in monomer melting temperature with an increase due to an increase molecular mobility. During thermal polymerization, the blends react faster without the use of metal catalysts. All of the cure enthalpies were somewhat lower than what was expected from the linear rule of mixtures and the highly crosslinked network architecture prevented full conversion of cyanate ester groups.

Table 6.3 DSC data for cyanate ester blends with calculated enthalpy of polymerization based on the linear rule of mixtures

Network	$\Delta H_{tot}$ (J/g)	Calculated $\Delta H_{tot}^*$ (J/g)	Difference (%)
<b>a</b>	585	N/A	N/A
<b>b</b>	545	564	4
<b>c</b>	490	544	11
<b>d</b>	417	502	21
<b>e</b>	400	461	15

## 6.2.4 TGA

The homopolymer and blended networks were analyzed by TGA, as shown in

Figure 6.9 and summarized in Table 6.4.

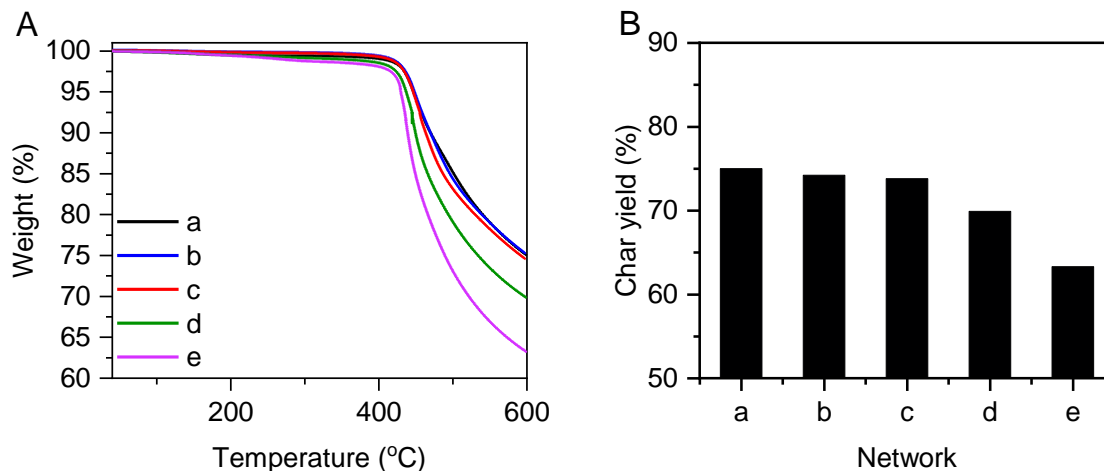


Figure 6.9 (A) TGA thermogram and (B) char yield bar graph for: (a) neat *cisResCy*, (b) 5 wt% *CardCy/cisResCy*, (c) 10 wt% *CardCy/cisResCy*, (d) 20 wt% *CardCy/cisResCy*, and (e) 30 wt% *CardCy/ResCy*.

Table 6.4 *Summary of TGA experiments*

<b>Network</b>	<b>a</b>	<b>b</b>	<b>c</b>	<b>d</b>	<b>e</b>
<b>T<sub>5%</sub> (°C)</b>	447	442	445	437	429
<b>T<sub>10%</sub> (°C)</b>	469	459	464	449	438
<b>Char Yield (%)</b>	75	74	73	69	63

The onset of decomposition temperature (5% mass loss, T<sub>5%</sub>), 10% mass loss temperature (T<sub>10%</sub>), and char yield at 600 °C were determined from the representative thermograms. The TGA scans of polymerized networks prepared from neat monomers and mixtures exhibited excellent thermal stability with T<sub>5%</sub>'s greater than 400 °C in nitrogen. Up to 400 °C the impact of cocuring CardCy and cisResCy monomers does not exhibit strongly systematic changes. It is notable that the T<sub>5%</sub> for **b** and **c** are virtually the same as cisResCy. With regard to T<sub>10%</sub>, compared with the cisResCy homopolymer, networks with ≤ 10% CardCy (**b** and **c**) have marginally lower values by 10 and 5 °C, respectively, reflecting the excellent thermal stability of the co-cured glassy networks. These findings suggest the onset of thermal decomposition temperature is influenced by the network architecture. For example, for blended networks the high concentrations of 15 carbon-long alkyl groups were not confined to the polymer backbone and were instead present as pendant moieties. The pendant chain ends occupied more free volume and prevented close packing of polymer chains, which lowered thermal stability.

Interestingly, networks **b** and **c** both demonstrated char yields nearly identical to the cisResCy homopolymer, with less than 2% difference. The similar char yields of networks **b** and **c** to the cisResCy homopolymer exhibits the retention of considerable thermal stability. Ultimately, blends with ≥ 20% CardCy had the lowest char yield

(Figure 6.9). Previously, increases in thermal stability of glassy polymer networks have been discussed in terms of aromatic content (monomer chemical structure) while decreases have been attributed to an increase in aliphatic character. Gouthaman et al.<sup>115</sup> studied several polycyanurate homopolymers (with similar degrees of crosslink density) and reported a higher char yield for a 4,4'-dicyanto naphthalene polymer when compared with other polycyanurates due to the fused naphthalene core leading to a highly aromatic network. These competing trends were evident in the thermal degradation measurements obtained here, considering the increased char yield for networks with the highest weight percentages of cisResCy.

### **6.2.5 DMA**

The neat and blended polymer networks were investigated by DMA to determine  $T_g$ 's and moduli values. The results are shown in Figure 6.10 and summarized in Table 6.5.

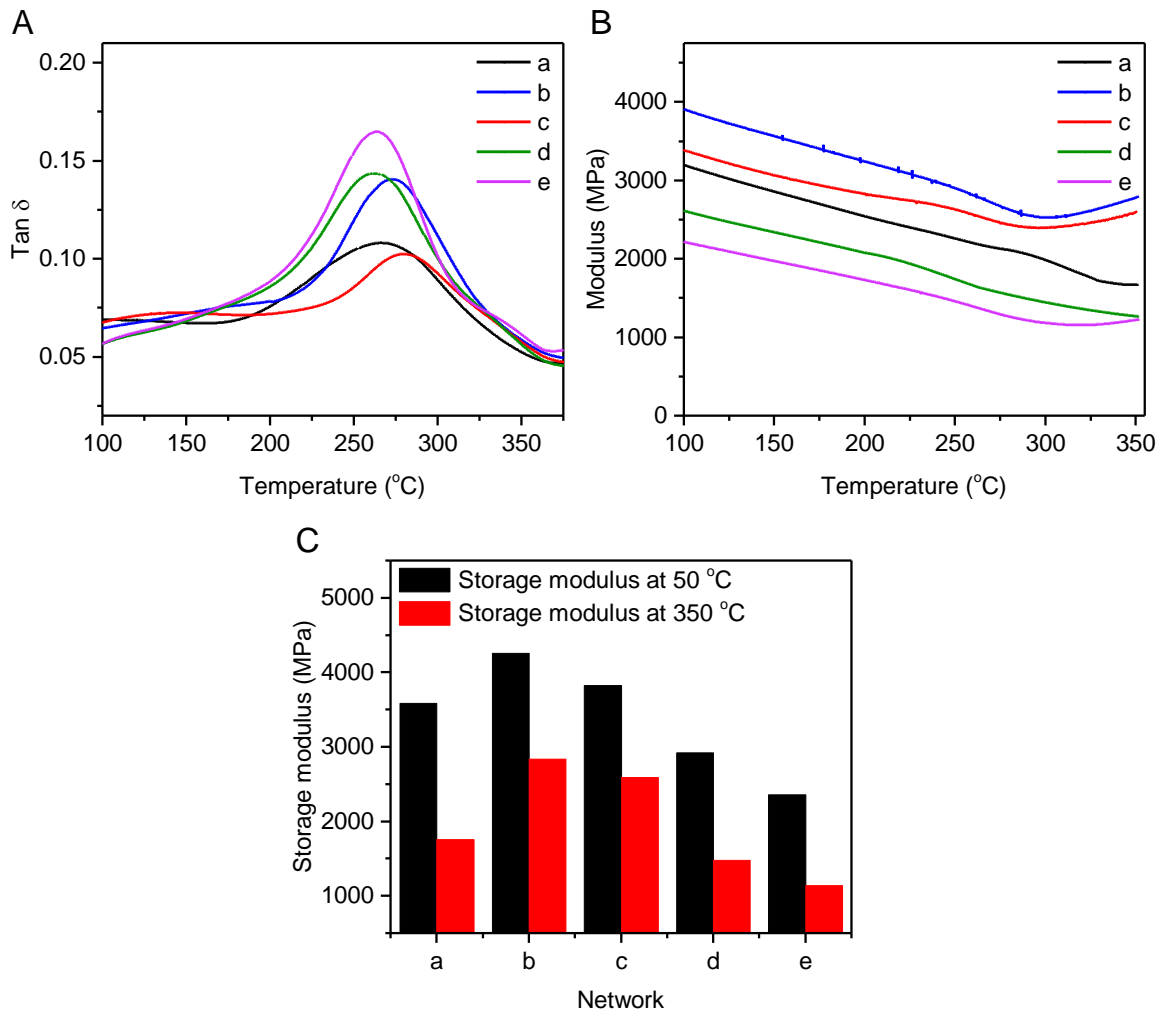


Figure 6.10 DMA thermogram of (A)  $\text{Tan } \delta$  and (B) Storage modulus, and (C) bar graph of glassy and rubbery moduli for: (a) neat ResCy, (b) 5 wt% CardCy/ cisResCy cisResCy cisResCy, (c) 10 wt% CardCy/ cisResCy, (d) 20 wt% CardCy/ cisResCy, and (e) 30 wt% CardCy/ cisResCy.

Table 6.5 Dynamic mechanical analysis of polymers.

Network	a	b	c	d	e
$T_g$ ( $^{\circ}\text{C}$ )	280	272	276	259	260
Modulus at 50 $^{\circ}\text{C}$ (MPa)	3588	4260	3824	2969	2356
Crosslink density ( $\text{mol cm}^{-3}$ )	12.3	18.3	17.2	10.1	7.3

The cisResCy homopolymer ensued the network with the highest  $T_g$  of 280 °C. Previous studies have shown that temperatures  $> 300$  °C are necessary to fully cure cisResCy, to reach a  $T_g > 350$  °C (as measured by TMA).<sup>14</sup> The difference in the  $T_g$  measured in this study, compared to the former, is likely due to the different cure protocol in the present study, as well as the difference in measurement (TMA vs. DMA). The blended networks had  $T_g$ 's ranging from  $\sim 259$  to 276 °C. The high  $T_g$ 's ( $> 250$  °C) are due to the high concentration of aromatic rings in the polymer backbone. It was interesting to note that networks **a**, **b**, and **c** have similar  $T_g$  values, despite the chemical differences, which may be rationalized on account of the high crosslink density averaging out these chemical differences. Compared to the ResCy homopolymer, the  $\sim 20$  °C depression in  $T_g$  for networks with  $\geq 20$  wt% CardCy was attributed to the 15-carbon long alkyl chain. The implication here is that the size and bulkiness of the pendant groups increased the free volume in between polymer chains, which lowered the  $T_g$ .<sup>116</sup>

The  $\tan \delta$  is a measure of the energy loss with regard to the recoverable energy.<sup>117</sup> The height is related to the internal friction of the system and is associated with the mechanical damping.<sup>117</sup> It can be seen in Figure 6.10 that there was an appreciable variation in peak height for the glassy networks. Blends with CardCy overwhelmingly have an increase in peak height compared to the cisResCy control. The increase in the  $\tan \delta$  for the polycyanurates with monofunctional CardCy reflect an increase in the number of mobile chain segments during the glass transition due to the presence of 15 carbon-long alkyl pendant groups. It should also be mentioned that the increase in the  $\tan \delta$  peak height implicated the CardCy blended networks were less brittle, which is advantageous

since high brittleness has historically been a key disadvantage for polycyanurate networks.

The variation of the crosslinked networks' storage moduli as a function of temperature is shown in Figure 6.10 and summarized in Table 6.5. At 50 °C the glassy moduli values were ranked in the following order: **b** > **c** > **a** > **d** > **e**. The rubbery moduli values at 350 °C followed the same trend such that the moduli values were highest for blended networks with  $\leq 10$  wt% CardCy and lowest for networks with  $\geq 20$  wt% CardCy. This suggests that the blended networks **b**, and to a lesser degree **c**, have highest crosslink densities. Networks **d** and **e** likely exhibit lower moduli by reason of the high monofunctional monomer and low trifunctional monomer content.

Interestingly, compared to homopolymer **a**, blends **b** and **c** had higher moduli, yet the blends had slightly lower  $T_g$  values. While the high rubbery moduli of the two blends suggested a more "closed" network, the decrease in  $T_g$  (compared to **a**) suggested the reverse. To investigate this, the crosslink density ( $\nu_e$ ) was calculated from the rubbery plateau, as described in the experimental section. The values are summarized in Table 6.5. It can be seen that networks **a**, **b**, and **c** have the highest  $\nu_e$ 's (12.3 to 18.3 mol cm<sup>-3</sup>) and networks **d** and **e** have the lowest  $\nu_e$ 's (7.3 to 10.1 mol cm<sup>-3</sup>). For mixtures with  $\leq 10$  wt% of CardCy, the increase in moduli was attributed to a reinforcing effect from the high concentration of physical crosslinks in the networks. On the other hand, glassy networks with  $\geq 20$  wt% of CardCy exhibit lower moduli and crosslink density because the monofunctional component cardCy, particularly given 15 carbon-long alkyl groups are not confined to the polymer backbone and are instead present as pendant moieties. On



the other hand, it should be mentioned that these pendant moieties of cardanol contain a 1,4-diene type structure that is amenable to polymerization (Figure 6.11).<sup>110</sup>

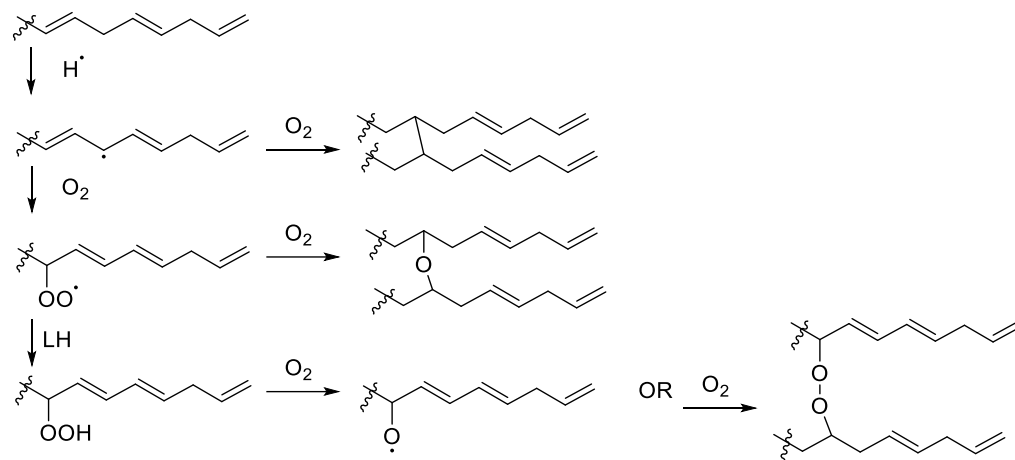


Figure 6.11 *Mechanism of thermal polymerization of 1,4-diene groups that may occur during thermal polymerization of in the presence of small amounts of oxygen.*<sup>110</sup>

Specifically, upon the loss of hydrogen in the active methylene group, the formed radical may produce carbonyl or hydroxyl groups in the presence of oxygen and hydroxyl radical during the polymerization. Although the polymerization was performed under nitrogen, minute amounts of oxygen may have resulted in the autooxidation of the CardCy side chain, resulting in a free-radical polymerization that yielded networks with favorable thermomechanical properties. While this is beyond the scope of the present study (and currently under investigation within our research group), it is worth mentioning that if CE's are to find increasing industrial relevance, then challenges related to improving impact resistance and toughness of the glassy networks must be addressed.

### 6.2.6 Rheology

To investigate the polymerization behavior of the bio-based monomers, The complex viscosity of the samples were obtained from rheology experiments and are reported in Figure 6.12. The ultra-low viscosity was one of the foremost alluring features of the monomer melt blends. All systems maintained a complex viscosity of  $\sim 0.05$  Pa.s up to 150 °C.

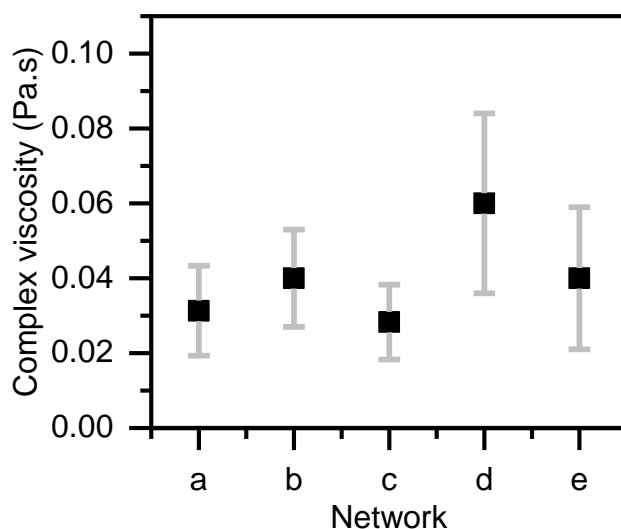


Figure 6.12 *Dynamic viscosity at of the cisResCy/CardCy mixtures at 100 °C: (a) neat cisResCy, (b) 5 wt% CardCy/ cisResCy, (c) 10 wt% CardCy/ cisResCy, (d) 20 wt% CardCy/ cisResCy, and (e) 30 wt% CardCy/ cisResCy.*

### 6.3 Conclusions

In this work we studied a series of plant-derived polycyanurate networks based on trifunctional (resveratrol) and monofunctional (cardanol) cyanate ester monomers, cisResCy and CardCy, respectively. The melting temperature of cisResCy was readily depressed once blended with CardCy, to obtain waxy solids that can be readily used for applications including filament winding and resin transfer molding. The addition of CardCy to cisResCy had a catalytic effect on thermal polymerization, which can be advantageous for reducing energy consumption to cure composite parts or B-staging carbon fiber pre-preg. Despite the decrease in polymerization temperatures, the glassy amorphous polymers had char yields and glass transition temperatures greater than 63% and 259 °C, respectively. This work demonstrates the utility in bio-based cyanate ester blends to develop high performance polycyanurates with unique custom properties for targeted applications.

## REFERENCES

- (1) Olalekan Odeyemi, S.; Adelodun Akinpelu, M.; Dotun Atoyebi, O.; Rukayah Titilope Yahaya. Determination of Load Carrying Capacity of Clay Bricks Reinforced With Straw. *Int. J. Sustain. Constr. Eng. Technol.* **2017**, 8 (2).
- (2) Strong, A. B. *Fundamentals of Composites Manufacturing: Materials, Methods, and Applications*, 2nd ed.; Society of Manufacturing Engineers: Dearborn, 2008.
- (3) Landman, D. *Developments in Reinforced Plastics*; London, 1986.
- (4) Hamerton, I. *Chemistry and Technology of Cyanate Ester Resins*; Chapman & Hall, 1994.
- (5) Ramdani, N.; Zaimche, H.; Derradji, M. Biobased Thermally-Stable Aromatic Cyanate Ester Thermosets: A Review. *React. Funct. Polym.* **2021**, 168, 105037.
- (6) Hamerton, I.; Hay, J. N. Recent Developments in the Chemistry of Cyanate Esters. *Polym. Int.* **1998**.
- (7) Guenther, A. J.; Wright, M. E.; Chafin, A. P.; Reams, J. T.; Lamison, K. R.; Ford, M. D.; Kirby, S. P. J.; Zavala, J. J.; Mabry, J. M. Mechanisms of Decreased Moisture Uptake in Ortho -Methylated Di(Cyanate Ester) Networks. *Macromolecules* **2014**, 47 (22), 7691–7700.
- (8) Fang, T.; Shimp, D. Polycyanate Esters: Science and Applications. *Prog. Polym. Sci.* **1995**, 20 (1), 61–118.
- (9) Wang, G.; Fu, G.; Gao, T.; Kuang, H.; Wang, R.; Yang, F.; Jiao, W.; Hao, L.; Liu, W. Preparation and Characterization of Novel Film Adhesives Based on Cyanate Ester Resin for Bonding Advanced Radome. *Int. J. Adhes. Adhes.* **2016**, 68, 80–86.
- (10) Laskoski, M.; Dominguez, D. D.; Keller, T. M. Oligomeric Cyanate Ester Resins:

- Application of a Modified Ullmann Synthesis in the Preparation of Thermosetting Polymers. *J. Polym. Sci. Part A Polym. Chem.* **2006**, *44* (15), 4559–4565.
- (11) Mileva, G.; Baker, S.; Konkle, A.; Bielajew, C. Bisphenol-A: Epigenetic Reprogramming and Effects on Reproduction and Behavior. *Int. J. Environ. Res. Public Health* **2014**, *11* (7), 7537–7561.
- (12) Ike, M.; Chen, M.-Y.; Jin, C.-S.; Fujita, M. Acute Toxicity, Mutagenicity, and Estrogenicity of Biodegradation Products of Bisphenol-A. *Environ. Toxicol.* **2002**, *17* (5), 457–461.
- (13) Harvey, B. G.; Sahagun, C. M.; Guenther, A. J.; Groshens, T. J.; Cambrea, L. R.; Reams, J. T.; Mabry, J. M. A High-Performance Renewable Thermosetting Resin Derived from Eugenol. *ChemSusChem* **2014**, *7* (7), 1964–1969.
- (14) Cambrea, L. R.; Davis, M. C.; Garrison, M. D.; Groshens, T. J.; Lyon, R. E.; Safronava, N. Processable Cyanate Ester Resin from Cis Resveratrol. *J. Polym. Sci. Part A Polym. Chem.* **2017**, *55* (6), 971–980.
- (15) Grigat, E.; Pütter, R. Synthesis and Reactions of Cyanic Esters. *Angew. Chemie Int. Ed. English* **1967**, *6* (3), 206–218.
- (16) Grigat, E.; Puetter, R. A Process for the Preparation of Aromatic Cyanate Esters. 1195764, 1963.
- (17) Grigat, E.; Puetter, R. A Process for Preparing Aliphatic Cyanate Esters Which Are Substituted by Electron-Attracting Atoms or Groups. 1201839, 1963.
- (18) Meylemans, H. A.; Harvey, B. G.; Reams, J. T.; Guenther, A. J.; Cambrea, L. R.; Groshens, T. J.; Baldwin, L. C. Synthesis, Characterization, and Cure Chemistry of Renewable Bis(Cyanate) Esters Derived from 2-Methoxy-4-Methylphenol.

- (19) Kessler, M. R. *Wiley Encyclopedia of Composites*; John Wiley & Sons, Inc.: Hoboken, NJ, USA, 2011.
- (20) Pankratov, V. A.; Frenkel, T. M.; Vinogradova, S. V.; Komarova, L. I.; Bondarev, V. B.; Korshak, V. V. Side Reactions in Synthesis of Phenyl Cyanate by Acylation of Phenol with Cyanogen Halides. *Bull. Acad. Sci. USSR Div. Chem. Sci.* **1974**, *23* (6), 1336–1337.
- (21) Cahn, R. W. Materials Science: Melting and the Surface. *Nature* **1986**, *323* (6090), 668–669.
- (22) Guenther, A. J.; Ramirez, S. M.; Ford, M. D.; Soto, D.; Boatz, J. A.; Ghiassi, K. B.; Mabry, J. M. Organic Crystal Engineering of Thermosetting Cyanate Ester Monomers: Influence of Structure on Melting Point. *Cryst. Growth Des.* **2016**, *16* (7), 4082–4093.
- (23) Bamane, S. S.; Gaikwad, P. S.; Radue, M. S.; Gowtham, S.; Odegard, G. M. Wetting Simulations of High-Performance Polymer Resins on Carbon Surfaces as a Function of Temperature Using Molecular Dynamics. *Polymers (Basel)*. **2021**, *13* (13), 2162.
- (24) Ghiassi, K. B.; Guenther, A. J.; Redeker, N. D.; Boatz, J. A.; Harvey, B. G.; Davis, M. C.; Chafin, A. P.; Groshens, T. J. Insights into Melting Behavior of Propyl-Bridged Di(Cyanate Ester) Monomers through Crystal Packing, Thermal Characterization, and Computational Analysis. *Cryst. Growth Des.* **2018**, *18* (2), 1030–1040.
- (25) Zheng, L.; Rice, B. M.; Thompson, D. L. Molecular Dynamics Simulations of the Melting Mechanisms of Perfect and Imperfect Crystals of Dimethylnitramine. *J.*

- Phys. Chem. B* **2007**, *111* (11), 2891–2895.
- (26) Luo, S.-N.; Strachan, A.; Swift, D. C. Nonequilibrium Melting and Crystallization of a Model Lennard-Jones System. *J. Chem. Phys.* **2004**, *120* (24), 11640–11649.
- (27) Wang, J.; Yoo, S.; Bai, J.; Morris, J. R.; Zeng, X. C. Melting Temperature of Ice Ih Calculated from Coexisting Solid-Liquid Phases. *J. Chem. Phys.* **2005**, *123* (3), 036101.
- (28) Agrawal, P. M.; Rice, B. M.; Thompson, D. L. Molecular Dynamics Study of the Effects of Voids and Pressure in Defect-Nucleated Melting Simulations. *J. Chem. Phys.* **2003**, *118* (21), 9680–9688.
- (29) Zhang, Y.; Maginn, E. J. A Comparison of Methods for Melting Point Calculation Using Molecular Dynamics Simulations. *J. Chem. Phys.* **2012**, *136* (14), 144116.
- (30) Alavi, S.; Thompson, D. L. Molecular Dynamics Studies of Melting and Some Liquid-State Properties of 1-Ethyl-3-Methylimidazolium Hexafluorophosphate [Emim][PF<sub>6</sub>]. *J. Chem. Phys.* **2005**, *122* (15), 154704.
- (31) Frenkel, D.; Ladd, A. J. C. New Monte Carlo Method to Compute the Free Energy of Arbitrary Solids. Application to the Fcc and Hcp Phases of Hard Spheres. *J. Chem. Phys.* **1984**, *81* (7), 3188–3193.
- (32) Alfè, D.; Price, G. D.; Gillan, M. J. Iron under Earth's Core Conditions: Liquid-State Thermodynamics and High-Pressure Melting Curve from Ab Initio Calculations. *Phys. Rev. B* **2002**, *65* (16), 165118.
- (33) Eike, D. M.; Maginn, E. J. Atomistic Simulation of Solid-Liquid Coexistence for Molecular Systems: Application to Triazole and Benzene. *J. Chem. Phys.* **2006**, *124* (16), 164503.

- (34) Pedersen, U. R. Direct Calculation of the Solid-Liquid Gibbs Free Energy Difference in a Single Equilibrium Simulation. *J. Chem. Phys.* **2013**, *139* (10), 104102.
- (35) Zou, Y.; Xiang, S.; Dai, C. Investigation on the Efficiency and Accuracy of Methods for Calculating Melting Temperature by Molecular Dynamics Simulation. *Comput. Mater. Sci.* **2020**, *171*, 109156.
- (36) Alavi, S.; Thompson, D. L. Simulations of Melting of Polyatomic Solids and Nanoparticles. *Mol. Simul.* **2006**, *32* (12–13), 999–1015.
- (37) Solca, J.; Dyson, A. J.; Steinebrunner, G.; Kirchner, B.; Huber, H. Melting Curve for Argon Calculated from Pure Theory. *Chem. Phys.* **1997**, *224* (2–3), 253–261.
- (38) Hay, J. N. *Chemistry and Technology of Cyanate Ester Resins: Processing and Cure Schedules for Cyanate Ester Resins*; Hamerton, I., Ed.; Chapman & Hall, 1994.
- (39) Pankratov, V.; S.V.Vinogradova; Korshak, V. V. The Synthesis of Polycyanates by the Polycyclotrimerisation of Aromatic and Organoelement Cyanate Esters. *Russ. Chem. Rev.* **1977**.
- (40) Campbell, F. C. Thermoset Resins: The Glue That Holds the Strings Together. In *Manufacturing Processes for Advanced Composites*; Elsevier, 2004; pp 63–101.
- (41) Guenther, A. J.; Harvey, B. G.; Chafin, A. P.; Davis, M. C.; Zavala, J. J.; Lamison, K. R.; Reams, J. T.; Ghiassi, K. B.; Mabry, J. M. Effect of Segmental Configuration on Properties of n -Propyl-Bridged Polycyanurate Networks. *Macromolecules* **2017**, *50* (13), 4887–4896.
- (42) Bauer, M.; Bauer, J.; Kühn, G. Kinetics and Modelling of Thermal



- Polycyclotrimerization of Aromatic Dicyanates. *Acta Polym.* **1986**, *37* (11–12), 715–719. <https://doi.org/10.1002/actp.1986.010371112>.
- (43) Ryu, B.-Y.; Emrick, T. Thermally Induced Structural Transformation of Bisphenol-1,2,3-Triazole Polymers: Smart, Self-Extinguishing Materials. *Angew. Chemie* **2010**, *122* (50), 9838–9841.
- (44) Luo, R.; Zhang, J.; Li, J.; Zhang, Y.; Zhang, J.; Su, C. Carbon/Carbon Composites. In *Wiley Encyclopedia of Composites*; John Wiley & Sons, Inc.: Hoboken, NJ, USA, 2011.
- (45) Lahaye, J.; Louys, F.; Ehrburger, P. The Reactivity of Carbon-Carbon Composites. *Carbon N. Y.* **1990**, *28* (1), 137–141.
- (46) Wang, W.; Wen, P.; Zhan, J.; Hong, N.; Cai, W.; Gui, Z.; Hu, Y. Synthesis of a Novel Charring Agent Containing Pentaerythritol and Triazine Structure and Its Intumescent Flame Retardant Performance for Polypropylene. *Polym. Degrad. Stab.* **2017**, *144*, 454–463.
- (47) Anslyn, E. V.; Dougherty, D. A. *Modern Physical Organic Chemistry*; University Science Books, 2006.
- (48) Lyon, R. E.; Walters, R. N.; Gandhi, S. Combustibility of Cyanate Ester Resins. *Fire Mater.* **2006**, *30* (2), 89–106.
- (49) Ramirez, M. L.; Walters, R.; Lyon, R. E.; Savitski, E. P. Thermal Decomposition of Cyanate Ester Resins. *Polym. Degrad. Stab.* **2002**, *78* (1), 73–82.
- (50) Harvey, B. G.; Guenther, A. J.; Lai, W. W.; Meylemans, H. A.; Davis, M. C.; Cambrea, L. R.; Reams, J. T.; Lamison, K. R. Effects of *o*-Methoxy Groups on the Properties and Thermal Stability of Renewable High-Temperature Cyanate Ester

Resins. *Macromolecules* **2015**, *48* (10), 3173–3179.

- (51) Guenthner, A. J.; Reams, J. T.; Lamison, K. R.; Ramirez, S. M.; Swanson, D. D.; Yandek, G. R.; Sahagun, C. M.; Davis, M. C.; Mabry, J. M. Synergistic Physical Properties of Cured Networks Formed from Di- and Tricyanate Esters. *ACS Appl. Mater. Interfaces* **2013**, *5* (17), 8772–8783.
- (52) Crawford, A. O.; Howlin, B. J.; Cavalli, G.; Hamerton, I. Examining the Thermo-Mechanical Properties of Novel Cyanate Ester Blends through Empirical Measurement and Simulation. *React. Funct. Polym.* **2012**, *72* (9), 596–605.
- (53) Koh, H. C. Y.; Dai, J.; Tan, E. Curing Behavior and Thermal Mechanical Properties of Cyanate Ester Blends. *J. Appl. Polym. Sci.* **2006**, *102* (5), 4284–4290.
- (54) Mattivi, F.; Reniero, F.; Korhammer, S. Isolation, Characterization, and Evolution in Red Wine Vinification of Resveratrol Monomers. *J. Agric. Food Chem.* **1995**, *43* (7), 1820–1823.
- (55) Bhullar, K. S.; Hubbard, B. P. Lifespan and Healthspan Extension by Resveratrol. *Biochim. Biophys. Acta - Mol. Basis Dis.* **2015**, *1852* (6), 1209–1218.
- (56) Tomé-Carneiro, J.; Larrosa, M.; Yáñez-Gascón, M. J.; Dávalos, A.; Gil-Zamorano, J.; González, M.; García-Almagro, F. J.; Ruiz Ros, J. A.; Tomás-Barberán, F. A.; Espín, J. C.; et al. One-Year Supplementation with a Grape Extract Containing Resveratrol Modulates Inflammatory-Related MicroRNAs and Cytokines Expression in Peripheral Blood Mononuclear Cells of Type 2 Diabetes and Hypertensive Patients with Coronary Artery Disease. *Pharmacol. Res.* **2013**, *72*, 69–82.
- (57) Jang, M.; Cai, L.; Udeani, G. O.; Slowing, K. V.; Thomas, C. F.; Beecher, C. W.

- W.; Fong, H. H. S.; Farnsworth, N. R.; Kinghorn, A. D.; Mehta, R. G.; et al. Cancer Chemopreventive Activity of Resveratrol, a Natural Product Derived from Grapes. *Science* (80-. ). **1997**, 275 (5297), 218–220.
- (58) Cash, J. J.; Davis, M. C.; Ford, M. D.; Groshens, T. J.; Guenther, A. J.; Harvey, B. G.; Lamison, K. R.; Mabry, J. M.; Meylemans, H. A.; Reams, J. T.; et al. High Tg Thermosetting Resins from Resveratrol. *Polym. Chem.* **2013**, 4 (13), 3859.
- (59) Garrison, M. D.; Harvey, B. G. Structure-Property Relationships of Cis-Resveratrol Cyanate Ester Blends. *Polymer (Guildf)*. **2021**, 213, 123194.
- (60) Garrison, M. D.; Savolainen, M. A.; Chafin, A. P.; Baca, J. E.; Bons, A. M.; Harvey, B. G. Synthesis and Characterization of High-Performance, Bio-Based Epoxy–Amine Networks Derived from Resveratrol. *ACS Sustain. Chem. Eng.* **2020**, 8 (37), 14137–14149.
- (61) Attanasi, O. A.; Del Sole, R.; Filippona, P.; Mazzetto, S. E.; Mele, G.; Vasapollo, G. Synthesis of Novel Lipophilic Porphyrin-Cardanol Derivatives. *J. Porphyr. Phthalocyanines* **2004**, 08 (11), 1276–1284.
- (62) Patnaik, P. *A Comprehensive Guide to the Hazardous Properties of Chemical Substances*, Third Edit.; New Jersey, 2007.
- (63) Kissinger, H. E. Variation of Peak Temperature with Heating Rate in Differential Thermal Analysis. *J. Res. Natl. Bur. Stand. (1934)*. **1956**, 57 (4), 217.
- (64) Ozawa, T. A New Method of Analyzing Thermogravimetric Data. *Bull. Chem. Soc. Jpn.* **1965**, 38 (11), 1881–1886.
- (65) Reams, J. T.; Guenther, A. J.; Lamison, K. R.; Vij, V.; Lubin, L. M.; Mabry, J. M. Effect of Chemical Structure and Network Formation on Physical Properties of

- Di(Cyanate Ester) Thermosets. *ACS Appl. Mater. Interfaces* **2012**, *4* (2), 527–535.
- (66) Hill, L. W. Calculation of Crosslink Density in Short Chain Networks. *Prog. Org. Coatings* **1997**, *31* (3), 235–243.
- (67) Materials Science Suite, Schrödinger, LLC Schrödinger Release 2021-1: Desmond Molecular Dynamics System, D. E. Shaw Research. Maestro-Desmond Interoperability Tools, Schrödinger. New York, NY 2021.
- (68) Desmond Molecular Dynamics System, D. E. Shaw Research, New York, NY, 2021. Maestro-Desmond Interoperability Tools, Schrödinger, New York, NY, 2021.
- (69) Nosé, S. A Unified Formulation of the Constant Temperature Molecular Dynamics Methods. *J. Chem. Phys.* **1984**, *81* (1), 511–519.
- (70) Hoover, W. G. Canonical Dynamics: Equilibrium Phase-Space Distributions. *Phys. Rev. A* **1985**, *31* (3), 1695–1697.
- (71) Martyna, G. J.; Tobias, D. J.; Klein, M. L. Constant Pressure Molecular Dynamics Algorithms. *J. Chem. Phys.* **1994**, *101* (5), 4177–4189.
- (72) DuBay, K. H.; Hall, M. L.; Hughes, T. F.; Wu, C.; Reichman, D. R.; Friesner, R. A. Accurate Force Field Development for Modeling Conjugated Polymers. *J. Chem. Theory Comput.* **2012**, *8* (11), 4556–4569.
- (73) Harder, E.; Damm, W.; Maple, J.; Wu, C.; Reboul, M.; Xiang, J. Y.; Wang, L.; Lupyán, D.; Dahlgren, M. K.; Knight, J. L.; et al. OPLS3: A Force Field Providing Broad Coverage of Drug-like Small Molecules and Proteins. *J. Chem. Theory Comput.* **2016**, *12* (1), 281–296.
- (74) Shivakumar, D.; Williams, J.; Wu, Y.; Damm, W.; Shelley, J.; Sherman, W.

- Prediction of Absolute Solvation Free Energies Using Molecular Dynamics Free Energy Perturbation and the OPLS Force Field. *J. Chem. Theory Comput.* **2010**, *6* (5), 1509–1519.
- (75) Sheng, X.; Akinc, M.; Kessler, M. R. Cure Kinetics of Thermosetting Bisphenol E Cyanate Ester. *J. Therm. Anal. Calorim.* **2008**, *93* (1), 77–85.
- (76) Guenther, A. J.; Yandek, G. R.; Wright, M. E.; Petteys, B. J.; Quintana, R.; Connor, D.; Gilardi, R. D.; Marchant, D. A New Silicon-Containing Bis(Cyanate) Ester Resin with Improved Thermal Oxidation and Moisture Resistance. *Macromolecules* **2006**, *39* (18), 6046–6053.
- (77) Fyfe, C. A.; Niu, J.; Rettig, S. J.; Burlinson, N. E. High-Resolution Carbon-13 and Nitrogen-15 NMR Investigations of the Mechanism of the Curing Reactions of Cyanate-Based Polymer Resins in Solution and the Solid State. *Macromolecules* **1992**, *25* (23), 6289–6301. <https://doi.org/10.1021/ma00049a028>.
- (78) Cambridge Structural Database <https://www.ccdc.cam.ac.uk/structures/>? (accessed Nov 2, 2021).
- (79) Agrawal, P. M.; Rice, B. M.; Zheng, L.; Velardez, G. F.; Thompson, D. L. Molecular Dynamics Simulations of the Melting of 1,3,3-Trinitroazetidine. *J. Phys. Chem. B* **2006**, *110* (11), 5721–5726.
- (80) Choudhary, N.; Chakrabarty, S.; Roy, S.; Kumar, R. A Comparison of Different Water Models for Melting Point Calculation of Methane Hydrate Using Molecular Dynamics Simulations. *Chem. Phys.* **2019**, *516*, 6–14.
- (81) Ma, S.; Li, S.; Gao, T.; Shen, Y.; Chen, X.; Xiao, C.; Lu, T. Molecular Dynamics Simulations of Structural and Melting Properties of Li<sub>2</sub>SiO<sub>3</sub>. *Ceram. Int.* **2018**, *44*

- (3), 3381–3387.
- (82) Liu, Y.; Lai, W.; Yu, T.; Ma, Y.; Guo, W.; Ge, Z. Melting Point Prediction of Energetic Materials via Continuous Heating Simulation on Solid-to-Liquid Phase Transition. *ACS Omega* **2019**, *4* (2), 4320–4324.
- (83) Liu, N.; Zeman, S.; Shu, Y.; Wu, Z.; Wang, B.; Yin, S. Comparative Study of Melting Points of 3,4-Bis(3-Nitrofurazan-4-Yl)Furoxan (DNFTF)/1,3,3-Trinitroazetidine (TNAZ) Eutectic Compositions Using Molecular Dynamic Simulations. *RSC Adv.* **2016**, *6* (64), 59141–59149.
- (84) Solca, J.; Dyson, A. J.; Steinebrunner, G.; Kirchner, B.; Huber, H. Melting Curves for Neon Calculated from Pure Theory. *J. Chem. Phys.* **1998**, *108* (10), 4107–4111.
- (85) Alvares, C. M. S.; Deffrennes, G.; Pisch, A.; Jakse, N. Thermodynamics and Structural Properties of CaO: A Molecular Dynamics Simulation Study. *J. Chem. Phys.* **2020**, *152* (8), 084503.
- (86) Sun, J.; Liu, P.; Wang, M.; Liu, J. Molecular Dynamics Simulations of Melting Iron Nanoparticles with/without Defects Using a Reaxff Reactive Force Field. *Sci. Rep.* **2020**, *10* (1), 3408.
- (87) Zhao, Y.; Stratt, R. M. Measuring Order in Disordered Systems and Disorder in Ordered Systems: Random Matrix Theory for Isotropic and Nematic Liquid Crystals and Its Perspective on Pseudo-Nematic Domains. *J. Chem. Phys.* **2018**, *148* (20), 204501.
- (88) Steinhardt, P. J.; Nelson, D. R.; Ronchetti, M. Bond-Orientational Order in Liquids and Glasses. *Phys. Rev. B* **1983**, *28* (2), 784–805.

- (89) SMARTS - A Language for Describing Molecular Patterns  
<https://www.daylight.com/dayhtml/doc/theory/theory.smarts.html>.
- (90) Eike, D. M.; Brennecke, J. F.; Maginn, E. J. Toward a Robust and General Molecular Simulation Method for Computing Solid-Liquid Coexistence. *J. Chem. Phys.* **2005**, *122* (1), 014115.
- (91) Luo, S.-N.; Ahrens, T. J.; Çağın, T.; Strachan, A.; Goddard, W. A.; Swift, D. C. Maximum Superheating and Undercooling: Systematics, Molecular Dynamics Simulations, and Dynamic Experiments. *Phys. Rev. B* **2003**, *68* (13), 134206.
- (92) Li, C.; Strachan, A. Molecular Scale Simulations on Thermoset Polymers: A Review. *J. Polym. Sci. Part B Polym. Phys.* **2015**, *53* (2), 103–122.
- (93) Alvares, C. M. S.; Deffrennes, G.; Pisch, A.; Jakse, N. Thermodynamics and Structural Properties of CaO: A Molecular Dynamics Simulation Study. *J. Chem. Phys.* **2020**, *152* (8), 084503.
- (94) Ren, Y.; Zhang, Y.; Mao, Q.; Pitsch, H. Amorphous-to-Crystalline Transition during Sintering of Nascent TiO<sub>2</sub> Nanoparticles in Gas-Phase Synthesis: A Molecular Dynamics Study. *J. Phys. Chem. C* **2020**, *124* (50), 27763–27771.
- (95) Fan, X.; Pan, D.; Li, M. Rethinking Lindemann Criterion: A Molecular Dynamics Simulation of Surface Mediated Melting. *Acta Mater.* **2020**, *193*, 280–290.
- (96) Lavine, M. S.; Waheed, N.; Rutledge, G. C. Molecular Dynamics Simulation of Orientation and Crystallization of Polyethylene during Uniaxial Extension. *Polymer (Guildf)*. **2003**, *44* (5), 1771–1779.
- (97) Tong, X.; Yang, P.; Zeng, M.; Wang, Q. Confinement Effect of Graphene Interface on Phase Transition of n -Eicosane: Molecular Dynamics Simulations.

- Langmuir* **2020**, *36* (29), 8422–8434.
- (98) Zheng, L.; Thompson, D. L. Molecular Dynamics Simulations of Melting of Perfect Crystalline Hexahydro-1,3,5-Trinitro-1,3,5-s-Triazine. *J. Chem. Phys.* **2006**, *125* (8), 084505.
- (99) Pinal, R. Effect of Molecular Symmetry on Melting Temperature and Solubility. *Org. Biomol. Chem.* **2004**, *2* (18), 2692.
- (100) Vyazovkin, S.; Burnham, A. K.; Criado, J. M.; Pérez-Maqueda, L. A.; Popescu, C.; Sbirrazzuoli, N. ICTAC Kinetics Committee Recommendations for Performing Kinetic Computations on Thermal Analysis Data. *Thermochim. Acta* **2011**, *520* (1–2), 1–19.
- (101) Andrew J. Guenther, Josiah T. Reams, Kevin R. Lamison, Lee R. Cambrea, Vandana Vij, J. M. M. The Influence of Monomer Chemical Structure on Late-Stage Cure Kinetics of Dicyanate Ester Resins; SAMPE: Dallas, TX.
- (102) de Nograro, F. F.; Llano-Ponte, R.; Mondragon, I. Dynamic and Mechanical Properties of Epoxy Networks Obtained with PPO Based Amines/MPDA Mixed Curing Agents. *Polymer (Guildf)*. **1996**, *37* (9), 1589–1600.
- (103) Park, J.; Eslick, J.; Ye, Q.; Misra, A.; Spencer, P. The Influence of Chemical Structure on the Properties in Methacrylate-Based Dentin Adhesives. *Dent. Mater.* **2011**, *27* (11), 1086–1093.
- (104) Wilkie, C. A.; Morgan, A. B. *Fire Retardancy of Polymeric Materials*, 2nd ed.; Taylor & Francis Group: Boca Raton, 2009.
- (105) Zhang, Z.; Xu, W.; Yuan, L.; Guan, Q.; Liang, G.; Gu, A. Flame-Retardant Cyanate Ester Resin with Suppressed Toxic Volatiles Based on Environmentally



- Friendly Halloysite Nanotube/Graphene Oxide Hybrid. *J. Appl. Polym. Sci.* **2018**, *135* (31), 46587.
- (106) Lyon, R. E.; Walters, R.; Gandhi, S. *Combustibility of Cyanate Ester Resins*; 2002.
- (107) Chen, T.; Lin, Q.; Xiong, L.; Lü, Q.; Fang, C. Preparation and Characterization of Carbon Foams from Cyanate Ester Mixtures. *J. Anal. Appl. Pyrolysis* **2015**, *113*, 539–544.
- (108) Grigat, E.; Pütter, R. Synthesis and Reactions of Cyanic Esters. *Angew. Chemie Int. Ed. English* **1967**, *6* (3), 206–218. <https://doi.org/10.1002/anie.196702061>.
- (109) Su, Y.; Zhang, S.; Zhou, X.; Yang, Z.; Yuan, T. A Novel Multi-Functional Bio-Based Reactive Diluent Derived from Cardanol for High Bio-Content UV-Curable Coatings Application. *Prog. Org. Coatings* **2020**, *148*, 105880.
- (110) Kanehashi, S.; Yokoyama, K.; Masuda, R.; Kidesaki, T.; Nagai, K.; Miyakoshi, T. Preparation and Characterization of Cardanol-Based Epoxy Resin for Coating at Room Temperature Curing. *J. Appl. Polym. Sci.* **2013**, *130* (4), 2468–2478.
- (111) Liu, Z.; Chen, J.; Knothe, G.; Nie, X.; Jiang, J. Synthesis of Epoxidized Cardanol and Its Antioxidative Properties for Vegetable Oils and Biodiesel. *ACS Sustain. Chem. Eng.* **2016**, *4* (3), 901–906.
- (112) Lochab, B.; Varma, I. K.; Bijwe, J. Thermal Behaviour of Cardanol-Based Benzoxazines. *J. Therm. Anal. Calorim.* **2010**, *102* (2), 769–774.
- (113) Amarnath, N.; Appavoo, D.; Lochab, B. Eco-Friendly Halogen-Free Flame Retardant Cardanol Polyphosphazene Polybenzoxazine Networks. *ACS Sustain. Chem. Eng.* **2018**, *6* (1), 389–402.
- (114) Chaplin, A.; Hamerton, I.; Howlin, B. J.; Barton, J. M. Development of Novel

- Functionalized Aryl Cyanate Ester Oligomers. 1. Synthesis and Thermal Characterization of the Monomers. *Macromolecules* **1994**, 27 (18), 4927–4935.
- (115) Gouthaman, S.; Madhu, V.; Kanemoto, S. O.; Madurai, S. L.; Hamerton, I. Examining the Thermal Degradation Behaviour of a Series of Cyanate Ester Homopolymers. *Polym. Int.* **2019**, 68 (10), 1666–1672.
- (116) Hamerton, I.; Howlin, B. J.; Klewpatinond, P.; Takeda, S. Examination of the Thermal and Thermomechanical Behavior of Novel Cyanate Ester Homopolymers and Blends with Low Coefficients of Thermal Expansion. *Macromolecules* **2009**, 42 (20), 7718–7735. <https://doi.org/10.1021/ma901657n>.
- (117) M. G., A.; Chatterjee, T.; Naskar, K. Assessing Thermomechanical Properties of a Reactive Maleic Anhydride Grafted Styrene-ethylene-butylene-styrene/Thermoplastic Polyurethane Blend with Temperature Scanning Stress Relaxation Method. *J. Appl. Polym. Sci.* **2020**, 137 (48), 49598.